UNIVERSITY OF CALIFORNIA
SANTA CRUZ

SEARCHING FOR DUAL AGNS IN GALAXY MERGERS: UNDERSTANDING DOUBLE-PEAKED [O III] AS A SELECTION METHOD

A dissertation submitted in partial satisfaction of the
requirements for the degree of

Doctor of Philosophy

in

ASTRONOMY & ASTROPHYSICS

by

Rosalie C. McGurk

June 2015

The Dissertation of Rosalie C. McGurk
is approved:

Professor Claire E. Max, Chair

Professor Constance Rockosi

Professor J. Xavier Prochaska

Doctor Bradford Holden

Tyrus Miller
Vice Provost and Dean of Graduate Studies

Table of Contents

List of Figures

List of Tables

Abstract

Searching for Dual AGNs in Galaxy Mergers: Understanding Double-Peaked [O III]

as a Selection Method

by

Rosalie C. McGurk

When galaxies merge, gas may accrete onto both central supermassive black holes. Thus, one expects to see close pairs of active galactic nuclei (AGNs), or dual AGNs, in a fraction of galaxy mergers. The existence and statistics of dual AGNs provide an important probe into hierarchical galaxy formation models, accretion-triggering mechanisms, galaxy merger rates, and black hole growth. However, finding them remains a challenge. The presence of double-peaked [O III] has been proposed as a technique to select dual AGNs efficiently. We studied a sample of double-peaked narrow [O III] emitting AGNs from the Sloan Digital Sky Survey. By obtaining new and archival high spatial resolution images taken with the Keck II Laser Guide Star Adaptive Optics system and the near-infrared (IR) camera NIRC2, we showed that 31%±3% of double-peaked [O III] emission line SDSS AGNs have two spatial components within a $3''$ radius.

However, the imaging discussed above does not show whether or how the double emission line structure relates to the presence of a companion. Spatially resolved spectroscopy or X-ray observations can confirm these galaxy pairs as systems containing two

AGNs. We followed up these spatially-double candidate dual AGNs with integral field spectroscopy from Keck OSIRIS and Gemini GMOS and with long-slit spectroscopy from Keck NIRSPEC and Shane Kast Double Spectrograph. We find double-peaked lines are sometimes dual AGN and sometimes outflows or narrow line kinematics. We also performed Chandra X-ray ACIS-S observations on 12 double-peaked candidate dual AGNs. Using our observations and 8 archival observations, we compare the distribution of X-ray photons to our spatially double near-IR images, measure X-ray luminosities and hardness ratios, and estimate column densities. By assessing what fraction of double-peaked emission line SDSS AGNs are true dual AGNs, we can better determine whether double-peaked [O III] is an efficient dual AGN indicator and constrain the statistics of dual AGNs.

To my parents and brother,

who always believe in me.

Acknowledgments

I owe a great deal to many people who have supported me scientifically and in every other way possible. Thank you to my parents, who "forced" me to attend the astronomy summer camp at the Pisgah Astronomical Research Institute (PARI) and supported me when I came home astronomy-crazy. Thank you to Dr. Michael Castelaz and Dr. Mel Blake, for feeding my astronomy dreams! Thanks to the then-undergraduate and graduate students at the University of Washington Astronomy Department for creating a fantastic environment to learn and grow. Throughout my graduate studies, Jolene Glenn and Sophia Chang have been outstanding supporters and friends; thanks for reminding me about life outside my academic bubble.

My sincerest thanks to my thesis advisor, Claire Max, whose mixture of hands-on and hands-off advising taught me to be a skilled and independent scientist. This work would not have been possible without her support and feedback. Thank you to my instrumentation advisor, Connie Rockosi, for all the fantastic afternoons and evenings of detector and software testing in the lab; adding instrumentation to my thesis was the best choice I made in grad school. Thank you also to Brad Holden and J. Xavier Prochaska; your feedback was always productive and useful.

I owe many thanks to all the UC Santa Cruz graduate students who have helped me along the way in innumerable ways: to my project managers and officemates Anne Medling and Alex Rudy, who kept me on track and cheered me on when I needed cheering; to Angie Wolfgang, for sharing work/life balance and passion for science; to Jerome Fang, for reminding me to have patience with the world; to Claire Dorman, for

brightening my days with your cheer; to Nathan Goldbaum, for supporting me in all my crazy ideas; and to the collective grads for their support, and for eating all the baked goods I insisted on bringing for everyone's birthdays. I owe a special debt of thanks to those who visited me in my cave during the last few months of crunch time: Alex Rudy, Claire Dorman, Tiffany Hsyu, Kat Feng, Emily Cunningham, and Camille Leilber.

Thank you so much to the UCO laboratory, software, and engineering staff, from whom I learned so much. Thanks especially to Michael Peck for teaching me so much about detectors and cryogenics. Thanks also to the Keck Observatory and Lick Observatory staff and support astronomers, for helping me collect all my data from carefully tuned telescopes and instruments!

Paper Acknowledgments

The text of this dissertation includes reprints of the following published and in-preparation material by McGurk: McGurk et al. (2011), McGurk et al. (2014), and McGurk et al. (2015).

The contents of McGurk et al. (2011) and McGurk et al. (2015) make up Chapters 2–6. I was responsible for obtaining the imaging and spectroscopic data, reducing the data, and analyzing it using my emission line fitting programs to get our results. I wrote the text and created the figures of these papers. I would like to thank my coauthors Claire Max, Anne Medling, Greg Shields, Julie Comerford, David Rosario, Krista Smith, and Shelley Wright for their support and permission to include these works in this dissertation.

Chapter 8 contains McGurk et al. (2014) supplemented with exploratory spec-

troscopy. I characterized the near-infrared detector, wrote operations software for the instrument, and helped commission the instrument and adaptive optics system. I wrote the text and created the figures of this paper. I would like to thank my coauthors Constance Rockosi, Donald Gavel, Renate Kupke, Michael Peck, Terry Pfister, Jim Ward, William Deich, John Gates, Elinor Gates, Barry Alcott, David Cowley, Daren Dillon, Kyle Lanclos, Dale Sandford, Mike Saylor, Srikar Srinath, Jason Weiss, and Andrew Norton for their support and permission to include this work in my dissertation.

Science Acknowledgments

This material is based in part upon work supported by the National Science Foundation under award numbers AST-0908796 and AST-1412851. McGurk was supported by a Graduate Research Fellowship from the National Science Foundation.

Data presented herein were obtained at the W. M. Keck Observatory, which is operated as a scientific partnership among the California Institute of Technology, the University of California, and the National Aeronautics and Space Administration. The Observatory and the Keck II Laser Guide Star AO system were both made possible by the generous financial support of the W. M. Keck Foundation. This research has also made use of the Keck Observatory Archive (KOA), which is operated by the W. M. Keck Observatory and the NASA Exoplanet Science Institute (NExScI), under contract with the National Aeronautics and Space Administration.

I wish to extend special thanks to those of Hawaiian ancestry, on whose sacred mountain we are privileged to be guests. Without their generous hospitality, the observations would not have been possible. The observatories of Mauna Kea have contributed

significantly to our understanding and wonder of the universe.

Funding for the SDSS and SDSS-II has been provided by the Alfred P. Sloan Foundation, the Participating Institutions, the National Science Foundation, the United States Department of Energy, the National Aeronautics and Space Administration, the Japanese Monbukagakusho, the Max Planck Society, and the Higher Education Funding Council for England. The SDSS Web Site is http://www.sdss.org/.

This research has made use of the NASA/IPAC Extragalactic Database (NED), which is operated by the Jet Propulsion Laboratory, California Institute of Technology, under contract with the National Aeronautics and Space Administration.

Chapter 1

Introduction

1.1 Background: Active Black Holes in Merging Galaxies

In ΛCDM cosmology, galaxies regularly interact and merge; hierarchical galaxy formation and evolution dictates that galaxies undergo multiple mergers as they evolve (e.g., Blumenthal et al., 1984; Spergel et al., 2007). The gravitational perturbations in the merger process can disturb the gas, remove angular momentum, and funnel it into the centers of the merging galaxies. We know that most massive galaxies harbor supermassive black holes (SMBHs) in their centers (Richstone et al., 1998; Kormendy & Richstone, 1995). This gas flowing into the galaxy's center can both cause new bursts of star formation in the nuclear regions and increase the amount of gas available to accrete onto the central SMBH (Hernquist, 1989; Kauffmann & Haehnelt, 2000; Hopkins et al., 2008). Gas in the process of accreting onto the black hole forms a hot accretion disk, which radiates thermal X-rays as a blackbody and harder X-rays due to non-thermal processes. This radiation associated with an accreting black hole identifies it as an

Active Galactic Nucleus (AGN). If AGN activity is triggered by galaxy mergers, AGN pairs should be observable in the various stages of at least some galaxy mergers.

Although AGN pairs are a natural result of major galaxy mergers, evidence for their existence has been lacking until relatively recently. On large (20 kpc – 1 Mpc) scales, the embedded SMBHs simply follow the motions of their host galaxies, which interact via gravity only. Large scale quasar clustering surveys show that about 0.1% of quasars are known to be in pairs on scales less than <1 Mpc; additionally, evidence for excess clustering on smaller (10–100 kpc) scales suggests that some of these pairs are caused by galaxy interactions (Hennawi et al., 2006). More specifically, hundreds of AGN pairs are known at $>$ 10 kpc separations (e.g., Myers et al., 2007, 2008; Hennawi et al., 2010; Green et al., 2010; Piconcelli et al., 2010).

However, this situation changes as we examine the later stages of galaxy mergers, with the separations of the SMBHs being between 0.01 kpc to 10 kpc. Gravity and dynamical friction become the main drivers of the system's evolution at scales of around 1–10 kpc, as the pair of SMBHs sink towards the center of the merged galaxy. With this change of driving mechanisms, we might expect to see the rate of AGN pairs change from wider scales. This "kiloparsec-scale" phase has seen recent progress in the identification of candidate pairs of AGN (commonly known as "dual AGN"). Confirming that two AGNs are present in these small-separation systems is very difficult and often requires multiple confirmation techniques, as we will describe in Section 1.3. Briefly, to confirm a dual AGN, it is necessary to have high enough spatial resolution to observe the two cores and a method to prove that each core hosts a unique AGN. Whether

an object is a "confirmed" dual AGN or a "candidate" dual AGN is a very subjective classification. Regardless, we present in Table 1.1 a list of confirmed and candidate dual AGNs winnowed from the literature. We place 20 objects on the confirmed list; the most well-known dual AGNs include NGC 6240 (Komossa et al., 2003), Mrk 463 (Bianchi et al., 2008), and Mrk 739 (Koss et al., 2011b). Regardless of how "confirmed" is defined, it will be very difficult to draw lasting conclusions from this small number of heterogeneously-selected dual AGNs.

A few attempts have been made recently to push modern selection techniques (explained in more detail in Section 1.3) to systematically find samples of dual AGNs and to move beyond single object detections. Low-redshift ($z<0.05$) AGNs that are detected as sources of ultra hard X-rays (Koss et al., 2010, 2011a, 2012) have a higher chance of being a dual AGN than optically-selected AGNs; Koss et al. (2012) published four new dual AGNs using this selection technique. However, this technique is only sensitive to very local galaxies and the lack of resolution of current ultra hard X-ray telescopes (e.g. *Swift* Burst Alert Telescope, Nuclear Spectroscopic Telescope Array) necessitates multi-wavelength observational follow-up of all targets. Ellison et al. (2011) use optical imaging and emission line diagnostics of Sloan Digital Sky Survey (SDSS; Abazajian et al., 2009) galaxies with redshifts 0.01–0.20 to find galaxy pairs hosting one and two AGNs with separations < 80 kpc; they find some nearby dual AGNs with separations 5–10 kpc but the SDSS imaging lacks the resolution to resolve separations smaller than this for local and higher redshift AGNs. These searches are a step forward but are limited to low redshifts.

The possibility of a large homogeneously-selected sample of $0.1<z<0.7$ candidate dual AGNs with small separations (< 10 kpc) was raised when Wang et al. (2009), Smith et al. (2010), and Liu et al. (2010b) noticed that about 1% of all Sloan Digital Sky Survey (SDSS) AGNs have double-peaked narrow [O III] emission lines. As a single peaked narrow line, strong [O III] emission indicates that an AGN may be present. Double-peaked narrow lines, spectrally separated by several hundred km s^{-1}, are a possible signature of the orbital motion of two unresolved AGNs spatially separated on kpc scales. These double-peaked AGNs increased the number of candidate dual AGNs from tens to hundreds. Additionally, Ge et al. (2012) widened the search parameters of the three previous double-peaked [O III] searches to include AGN/star formation (SF) composite galaxies and to include asymmetric as well as double-peaked line profiles; they find that approximately 1% of all emission line galaxies are double-peaked, 40% (1318 objects) of which are AGN or composite galaxies. Ge et al.'s objects are considered less likely to be dual AGN since they lack the strong signature of at least one AGN present in the galaxy, which was guaranteed using the selection methods of Wang et al., Smith et al., and Liu et al. While only a fraction of these double-peaked [O III] AGNs are expected to actually be dual AGNs, this selection technique might greatly increase the number of known dual AGNs.

Table 1.1: List of Confirmed and Candidate Dual AGNs with Separations <15kpc

Reference	Name	Sep (kpc)	z	Detection / Confirmation Methods
Confirmed Dual AGNs				
Junkkarinen et al. (2001)	LBQS 0103−2753	2.3	0.848	HST imaged & LS unique spec
Gregg et al. (2002)	SDSS J233646.2−010732.6	14.2	1.285	near-IR imaging, unique spec
Komossa et al. (2003)	NGC 6240	0.75	0.02	HST imaging, X-ray imaging
Ballo et al. (2004); Zezas et al. (2003)	Arp 299	4.6	0.0105	HST imaging, Chandra & XMM imaging
Guainazzi et al. (2005)	ESO 509-IG066	10.5	0.04	HST imaging & XMM 2 nuclei
Rodriguez et al. (2006)	4C +37.11 (0402+379)	0.0073	0.06	VLBA imaging and SED
Owen et al. (1985); Hudson et al. (2006)	3C75 (NGC 1128, Abell 400)	7.2	0.023	2 compact radio nuclei each with double-lobed jet, Chandra 2 nuclei
Bianchi et al. (2008)	Mrk 463	3.8	0.0504	HST, XMM, Chandra imaging
Boroson & Lauer (2009)	SDSS J153636.22+044127.0	?0.0001	0.388	SDSS double broad lines
Decarli et al. (2009); Wrobel & Laor (2009); Bondi & Pérez-Torres (2010)	SDSS J153636.22+044127.0	5.1	0.388	2 AGN with HST, VLA, & VLBI
Comerford et al. (2009a)	COSMOS J100043.1+020637	1.75	0.36	HST imaging, Keck spec, VLA

Continued on next page

Table 1.1 – *Continued from previous page*

Reference	Name	Sep. (kpc)	z	Detection / Confirmation Methods
Civano et al. (2010)	CID-42 (J100043.1+020637)	2.46	0.359	HST image, VLT LS spec, Chandra image
Piconcelli et al. (2010)	IRAS 20210+1121	11	0.056	XMM hard x-rays have 2 nuclei
McGurk et al. (2011)	SDSS J095207.62+255257.2	4.8	0.34	double [O III], AO imaging & IFU spec
Fu et al. (2011b)	SDSS J150243.1+111557	7.4	0.39	double [O III], AO imaging, EVLA
Koss et al. (2011b)	Mrk 739	3.4	0.030	SDSS image, XMM, VLA, Chandra image
Peng et al. (2011); Frey et al. (2012)	SDSS J142507.32+323137.4	2.6	0.478	SDSS double [O III], VLBI 2 nuclei
Koss et al. (2012)	IRAS 05589+2828	8.0	0.03	BAT detected, Chandra image, SDSS spec
	IRAS 03219+4031	10.8	0.047	
	NGC 3227/3226	12.3	0.0038	
	NGC 835/833	14.8	0.013	
Mazzarella et al. (2012)	Mrk 266	5.9	0.028	VLA, Chandra, HST
Liu et al. (2013); Liu et al. (2010a); Shen et al. (2011)	SDSS J110851.04+065901.4	2.1	0.182	SDSS double [O III], HST & Keck 2 nuclei, *Chandra*, LS spec conf
Liu et al. (2013); McGurk et al. in press;	SDSS J114642.47+511029.6	6.3	0.130	SDSS double [O III], HST & Keck 2 nuclei, *Chandra*, LS spec conf

Continued on next page

Table 1.1 – *Continued from previous page*

Reference	Name	Sep. (kpc)	z	Detection / Confirmation Methods
Liu et al. (2010a); Shen et al. (2011)				
U et al. (2013)	Mrk 273	0.750	0.038	Keck AO imaging and IFU spec
Huang et al. (2014)	J0038+4128	4.7	0.0725	HST 2 nuclei, spat resolved spec T1+T2
McGurk et al. in prep	SDSS J130724.08+460400.9	11.6	0.353	double [O III], Keck & *Chandra* 2 nuclei
Candidate Dual AGNs				
Sillanpaa et al. (1988); Valtonen et al. (2008)	OJ287	?0.00001	0.306	12 year periodic pairs of flares
Zhou et al. (2004)	SDSS J104807.74+005543.5	0.020	0.64	double [O III], faint 2nd VLBA nucleus
Dasyra et al. (2006)	PG1426+015 (Mrk1383)	$\sim$4	0.087	near-IR 2 nuclei, unique spectra
Pindor et al. (2006)	SDSS J112012.12+671116.0	9.0	1.49	near-IR 2 nuclei, unique spectra
Gerke et al. (2007);	EGSD2 J142033.66+525917.5	1.2	0.705	HST imaging of 1 asymmetric elliptical, 2 emission lines distinct in LS spec
Comerford et al. (2009b)		0.84	0.71	Keck spec
Barth et al. (2008)	NGC 3341	5.1, 8.4	0.027	3 SDSS nuclei, Keck spec, central nucleus SF-dom, offset1 AGN, offset2 ?
Evans et al. (2008);	3C 321	6.4	0.096	HST imaging, Chandra, VLA

Continued on next page

Table 1.1 – *Continued from previous page*

Reference	Name	Sep. (kpc)	z	Detection / Confirmation Methods
Martel et al. (1999)				
Dotti et al. (2009) Komossa et al. (2008)	SDSS J092712.65+294344.0	0.0003	0.70	2600 km s^{-1} double peaked lines in SDSS
Comerford et al. (2009b)	EGSD2 J141550.8+520929	1.6	0.62	Keck spec, no imaging
Wang et al. (2009); Smith et al. (2010); Liu et al. (2010b)	340 objects			double-peaked narrow [O III] SDSS AGNs
Xu & Komossa (2009)	SDSS J131642.90+175332.5	?	0.150	double narrow lines, similar line ratios
Decarli et al. (2010)	4C 22.25	?	0.4183	SDSS broad lines offset by 8700 km s^{-1}
Schawinski et al. (2011)	CDFN J123652.77+621354.8	5	1.35	HST imaging & spec, Chandra unresolved
Liu et al. (2011)	SDSS J102700.4+174900.8	3.0, 2.4	0.066	SDSS 3 nuclei, LS spec 1 AGN, 2 LINER
Fabbiano et al. (2011)	NGC 3393	0.15	0.012	Chandra 2 unresolved nuclei, HST &VLA
Liu et al. (2010a); Shen et al. (2011)	SDSSJ113126.08+020459.2 SDSSJ133226.34+060627.4	1.5 5.1	0.146 0.207	NIR imaging, LS spec
Barrows et al. (2012)	CXOXBJ142607.6+353351	5.5	1.175	Chandra bright, Keck AO image 1 nucleus, spatially separated double emission lines
Ge et al. (2012)	1318 objects			double-peaked narrow and asymmetric

Continued on next page

Table 1.1 – *Continued from previous page*

Reference	Name	Sep. (kpc)	z	Detection / Confirmation Methods
				SDSS composite galaxies
Barrows et al. (2013)	131 objects		0.8-1.6	SDSS double [Ne V]λ3426 or [Ne III]λ3869
Benítez et al. (2013)	Mrk 1469 (J121607.08+504930.0)	?	0.031	double peaked emission lines
Imanishi & Saito (2014)	IRAS 16474+3430 (J1649+3425)	?	0.111	Subaru AO K & L imaging 2 nuclei
Gabányi et al. (2014); Benítez et al. (2013)	NGC 5515 (J141238.14+391836.5)	?	0.0257	double peaked emission lines, 1 VLA source
Ohyama et al. (2015)	NGC 3256	0.85	0.008	HST, mid-IR, Chandra
Comerford et al. (2015)	SDSS J112659.54+294442.8	1.76	0.102	double [O III], Chandra & HST

1.2 The Importance of Finding Close Pairs of AGNs in Merging Galaxies

Finding a way to uniformly select a statistically significant set of pairs of AGNs from some fraction of mergers would help us to answer numerous questions about the formation and evolution of AGNs and their host galaxies through mergers.

1.2.1 AGN Activity and Triggering

When are AGNs activated during the various stages of mergers? How much gas must reach the nuclear region before the AGN is activated? How long is the AGN duty cycle – the fraction of time the AGN is brightly accreting material instead of faintly quiescent? Do AGNs rapidly flicker between activity and quiescence, or do AGNs have a period of strong accretion followed by long periods of quiescence? Does the duty cycle change with merger stage, gas fraction, star formation rate, etc.? LaMassa et al. (2013) show how AGN activity is better linked to the central SF of the galaxy than to general SF levels. The duty cycle of radio AGN is well matched to the gas cooling rate, suggesting that fuel depletion has a strong influence on the duty cycle (Shabala et al., 2008). Hopkins et al. (2006) and Hopkins et al. (2015), to name a few, examine how the gas fraction changes the AGN activity in mergers. However, papers attempting to simulate AGNs and their effect on their host galaxies use sub-grid prescriptions of physics involved; these prescriptions need refinement and comparison with data to more accurately incorporate AGNs into these galaxy-scale models. Answering these questions requires a sample of dual AGNs to study.

1.2.2 Galaxy Evolution: Merger-Driven or Secular?

Are mergers the primary mechanism that feeds black holes and triggers AGN activity? What role does secular evolution play in growing the black holes? There are two primary methods to supply gas to galaxies. "Merger-driven evolution" is when a galaxy increases its own gas supply by colliding with a gas-rich galaxy. The gravitational perturbations due to the merger can allow the gas to flow into the galactic center and may trigger accretion onto the black hole (Hernquist, 1989; Kauffmann & Haehnelt, 2000; Hopkins et al., 2008). "Secular evolution" is the accretion of gas from the surrounding intergalactic medium, possibly flowing along filaments of dark matter in the cosmic web (Dekel & Birnboim, 2006; Dekel et al., 2009). This gas may be pristine and low-metallicity, or it may have been enriched in the galaxy and ejected at an earlier time. Both processes are important components of galaxy evolution, but do either dominate in certain conditions? Studies of AGNs selected by different techniques get opposing results: some show strong correlations of the AGNs with major galaxy mergers (Koss et al., 2010; Ellison et al., 2011), while other studies do not find a higher rate of AGNs undergoing mergers than field galaxies undergoing mergers (Cisternas et al., 2011; Kocevski et al., 2012). Treister et al. (2012) use multi-wavelength observations of AGNs and correlate them with nearby mergers; they find that only 10% of AGNs are likely triggered by a major galaxy merger. However, since this triggered 10% are the most luminous AGNs, Treister et al. also conclude that $\sim$50% of black hole growth over cosmic time is associated with major mergers. This result is still controversial, however, because of the selection effects that complicate the combining of various datasets. Dual

AGN provide a unique sample of galaxies where the AGN activity is triggered by mergers. This sample can be used to address the question of how important mergers are as compared to secular evolution in the growth of SMBH.

1.2.3 Binary Black Hole and Coalescence Rates

Regardless of whether both black holes activate as AGN, we expect all major galaxy mergers to result in a binary black hole, which may eventually merge into a single black hole. Pure N-body simulations of late merger stages predict that the black holes' inspiral may stall at separations of approximately one parsec, because the black holes will have ejected all of the stars in the loss cone and therefore lost their means to easily remove angular momentum from the system (Milosavljević & Merritt, 2003b). Multiple solutions to the final parsec problem suggest that it has been solved for many situations: interactions with surrounding gas and the accretion disk (Escala et al., 2004; Lodato et al., 2009), stellar loss cone refilling (Milosavljević & Merritt, 2003a), nonaxisymmetric galaxy potentials (Berczik et al., 2006; Preto et al., 2011), black hole wandering (Merritt, 2001), and/or the Kozai mechanism (Blaes et al., 2002). Understanding the rate of dual AGNs at successively smaller separations of the black holes can potentially aid in the prediction of the rate of binary black holes emitting gravitational waves and eventually of black hole coalescence events both with gravitational wave experiments similar to *LISA* (the *Laser Interferometer Space Antenna*; Thorne, 1995; Hughes, 2002; Vecchio & Wickham, 2004) and with pulsar timing arrays (Lee et al., 2011; Jenet et al., 2009; Ferdman et al., 2010; Hobbs et al., 2010; Manchester et al., 2013).

To answer the questions posed in the previous Subsections, one needs a substantial sample of mergers hosting zero, one and two AGNs; this thesis attempts to increase the number of close (<15 kpc) mergers hosting two AGNs using a new sample selection technique, double-peaked [O III] λ5008Å emission lines.

1.3 Current Methods of Confirming Pairs of AGNs in Merging Galaxies

To *confirm* a potential dual AGN, each spatially resolved source has to be proved to contain a unique AGN (pairs of AGNs will such small separations that they cannot be resolved will not be discussed). Multiple techniques are available to detect single AGN, but not all are suitable for the task of confirming close pairs of AGNs at a variety of redshifts. We discuss some of the techniques in the following paragraphs.

Radio interferometry is one of the unambiguous ways to confirm a nucleus or two nuclei as AGN(s). The nucleus of an AGN appears as a compact core in radio observations. The spectrum of such cores are well-fitted by power-laws; roughly flat spectra are observed in the dual AGNs confirmed with radio interferometry (Rodriguez et al., 2006; Fu et al., 2011b). Long baseline interferometry, such as performed by the VLBA, VLBI, and JVLA, enables high spatial resolutions, necessary for finding small-separation pairs. The classic 7.3 pc dual AGN in radio galaxy 0402+379 is show in Figure 1.1. However, only ∼10% of AGNs are radio-loud (Wilson & Colbert, 1995), limiting the sample that can be quickly confirmed with this method. Additionally, radio

loud cores are also often surrounded by diffuse or collimated radio emission from the jets of the AGN; these features increase the difficulty of determining the origin of the observed radio emission. While it is possible to observe radio-quiet AGNs (detected faintly in the radio) with little worry about jet or jet-related emission, the exposure times necessary for strong detections can become expensive in telescope time.

Mid-infrared (mid-IR) color diagnostics are another way of detecting AGNs. Regardless of obscuration, AGNs have a strong mid-IR (3–10μm) continuum from hot dust around the AGN that can be used to distinguish between AGNs and star forming galaxies. Mid-IR satellites such as the *Spitzer Space Telescope* and the *Wide-Field Infrared Survey Explorer* (*WISE*) have imaging capabilities in multiple bands; ratios of the flux in these various *Spitzer* and *WISE* photometric bands place AGNs on either the Spitzer-based Lacy et al. (2004) or Stern et al. (2005) wedges, the WISE-based Stern et al. (2012) W1-W2 cutoff, or the WISE-based Mateos et al. (2012) wedge, as shown in Figure 1.2. However, both telescopes lack the spatial resolution to confirm small separation pairs; *WISE*'s resolution ranges between $6\farcs1$ to $12\farcs0$ for its 3.4–22 μm bands, and *Spitzer*'s resolution varies widely from $2''$ at 3 μm wavelengths up to $40''$ at 180 μm wavelengths.

Optical imaging and emission line diagnostics are a third method of detecting AGNs. Baldwin et al. (1981) (hereafter BPT) demonstrated that it was possible to use the intensity ratios of two pairs of relatively strong emission lines (classically [O III] λ5008Å/Hβ and [N II] λ6584Å/Hα) to distinguish AGNs from normal or star-forming galaxies. These techniques have since been refined by many authors, including

Veilleux & Osterbrock (1987), Kewley et al. (2001), and Kauffmann et al. (2003) (to name only a few). Kauffmann et al. (2003)'s BPT diagram is shown in Figure 1.3. To unequivocally prove a nucleus as an AGN, and not a shock / star formation / AGN / low ionization emission region (LINER) composite object, both emission line ratios used must be high enough to place the object in the upper right quadrant of the BPT diagram; ratios of [O III]/Hβ> 3 and [N II]/Hα> 0.6 are often used as the definition of AGNs (Kauffmann et al., 2003). The abundance of optical spectroscopy available publicly through the Sloan Digital Sky Survey and other surveys has made this one of the most commonly-used and well-understood diagnostics. However, the spatial resolution of most publicly available data is not sufficient to find small pairs of objects; seeing limited imaging and 3″ diameter fiber spectroscopy prevents the easy detection of close pairs and blurs the origins of the observed emission lines. Additional high resolution imaging (often from *HST*) is necessary to determine if multiple spatial components are present, and spatially resolved spectroscopy, either from a long-slit or from an integral field unit, is necessary to determine if each spatial component is independently an AGN (e.g., Greene et al., 2011; Rosario et al., 2011; Shen et al., 2011; Comerford et al., 2012; Fu et al., 2012; McGurk et al., 2015). While this diagnostic is well accepted, skeptics point out that even cases where two optical AGN emission components are observed to be precisely coincident with two stellar bulges can be explained by a single AGN located between the two stellar bulges with extended emission covering or illuminating both bulges (Moran et al., 1992).

Near-IR imaging and emission line ratio diagnostics are a fourth way

to detect AGN. Near-IR imaging, especially when assisted with adaptive optics, can detect two stellar components down to small separations (generally $\geq 0\farcs2$ in our observations). Additionally, since the near-IR is less sensitive to obscuration by dust than the optical bands, often near-IR imaging can reveal more detail of the inner regions of the galaxies (Max et al., 2005; McGurk et al., 2011; Fu et al., 2011a; Rosario et al., 2011; Fu et al., 2012; McGurk et al., 2015). With adaptive optics systems becoming more common among moderate (2–5 m) and large (5 m and up) telescopes, this technique is becoming more available. Similar in concept to the optical BPT diagram, Larkin et al. (1998) and Rodríguez-Ardila et al. (2008) (shown in Figure 1.4) use the near-IR emission line flux ratios [Fe II] $\lambda 1.2570\mu$m/Paβ vs. H_2 $\lambda 2.121\mu$m/Brγ to distinguish between near-IR AGN activity and star-formation. However, near-IR emission line ratio diagnostics are less well understood and accepted than their optical counterparts. Since near-IR spectroscopy is not publicly available for most objects, independent observations are needed to use this technique. A benefit of these diagnostics are that they can be used in conjunction with the high spatial resolutions afforded by adaptive optics, making the confirmation of AGN pairs with small separations possible. Further testing of this diagnostic with known X-ray and optical AGNs and modeling of the line ratios used by this diagnostic are necessary for it to be more widely accepted.

High-energy X-ray observations are another unambiguous way to confirm a nucleus or two nuclei as AGN(s). X-ray observations are often considered the gold standard of AGN confirmation, since high X-ray luminosities ($>10^{42}$ ergs s^{-1}) must originate from an actively accreting supermassive black hole. Figure 1.5 from Szokoly

et al. (2004) illustrates this luminosity cutoff for AGNs. The *Chandra Space Telescope* has confirmed several pairs of AGN with wide ($>1''$) separations (Komossa et al., 2003; Comerford et al., 2011; Koss et al., 2011b), but *Chandra* lacks the spatial resolution to find dual AGNs at smaller separations.

Detecting **ultra hard x-rays** ($>$ 14 keV) from an AGN seems to improve the odds of the system containing a second AGN, but alone is not a confirmation technique. The *Swift* Burst Alert Telescope (BAT) all-sky 14–195 keV X-ray survey (Koss et al., 2010) is the most complete sample of AGNs in the local universe, since hard X-rays in this energy range are neither affected by galactic dust nor diluted by star formation. BAT-detected AGNs (Koss et al., 2010, 2012) are much more likely to be found in mergers than optically-selected SDSS AGNs (Rosario et al., 2011; Ellison et al., 2011), as shown in the left panel of Figure 1.6. Additionally, 10% of BAT-detected AGNs have an AGN in their companion galaxy, versus 0.5% of SDSS Seyfert AGNs having an AGN companion (Koss et al., 2012). The fraction of dual AGNs increases as the separations of the two AGNs get smaller, as shown in the right panel of Figure 1.6. Unfortunately, this technique is only sensitive to very local ($z<0.05$) galaxies. Since the resolution of BAT is $17'$, follow-up observations are necessary to localize the presence of one AGN to a single galaxy, let alone determine if there is a second AGN present in any companion galaxy.

It is generally necessary to use some assortment of the techniques described

above to prove that a candidate is a true dual AGN and not a multitude of other possible scenarios. Without spatially resolved spectroscopy to match the observed galaxies or their nuclei to their corresponding double-peaked emission lines, the double peaks of spectral lines such as [O III] may be due to:

- a recoiling supermassive black hole (SMBH) (Bonning et al., 2007; Comerford et al., 2009a; Civano et al., 2010; Guedes et al., 2011),
- jets interacting with the surrounding medium (Whittle & Wilson, 2004; Rosario et al., 2010; Rupke & Veilleux, 2013c),
- biconical or one-sided outflows from a single AGN (Fischer et al., 2011; Rupke & Veilleux, 2013c,a),
- rotating gaseous disks (Smith et al., 2012),
- rings of star formation, or
- complex narrow line region kinematics (Falcke et al., 1998; Xu & Komossa, 2009).

Similarly, without one of the spatially resolved techniques described above, the multiple bright cores imaged in or around one galaxy may be any of the previously listed scenarios, a chance superposition of two objects, gravitationally lensed sources (Hennawi et al., 2006), or a clump of intense star formation.

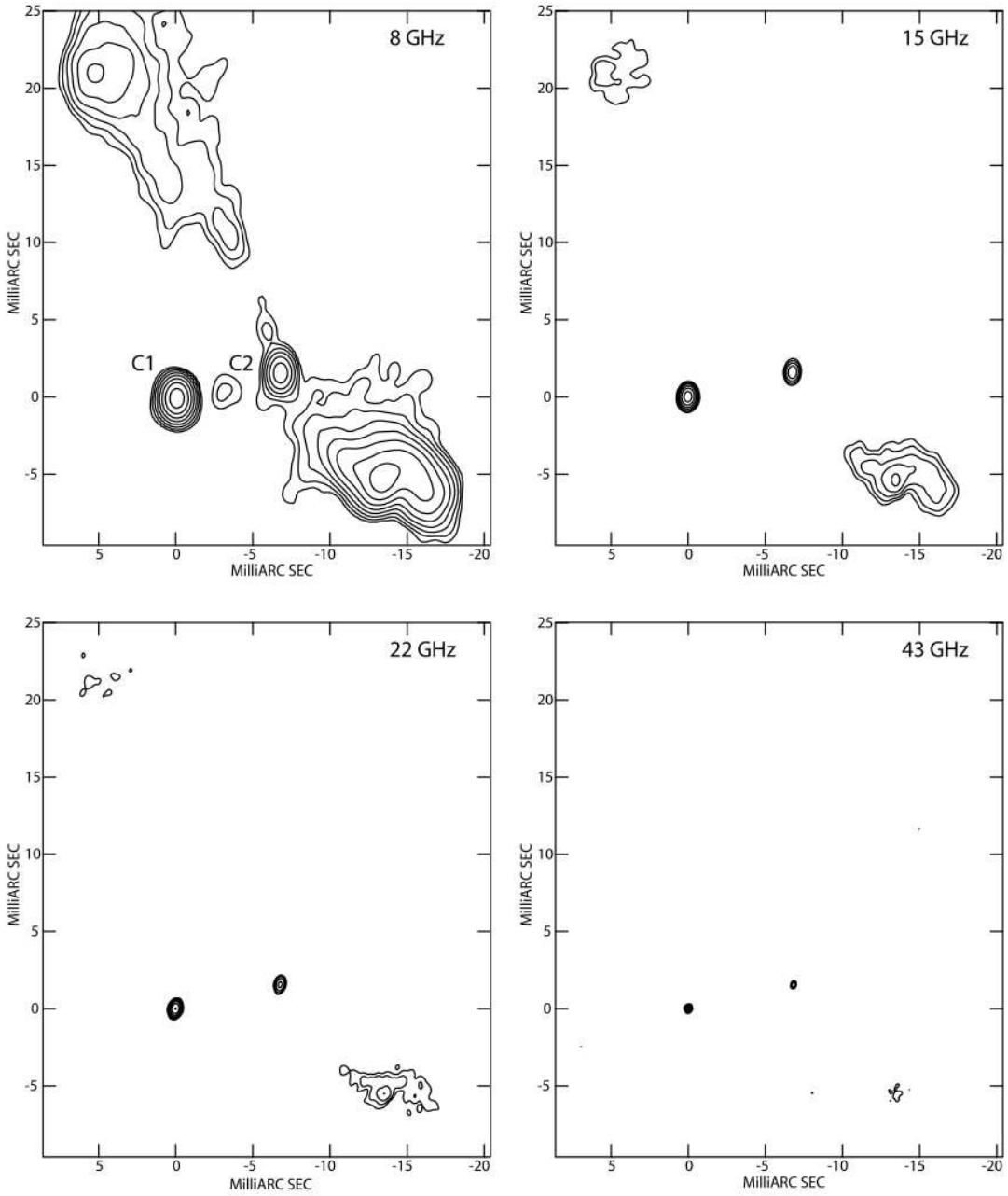

Figure 1.1: VLBA images of the dual AGN in radio galaxy 0402+379. The images are at 8, 15, 22 and 43 GHz, respectively. Contours are drawn beginning at 3σ and increase by factors of 2 thereafter. The labels shown in the 5 GHz map indicate the positions of the two strong, compact, central components determined to be AGN with a separation of 7.3 pc. For more detail, see the paper.

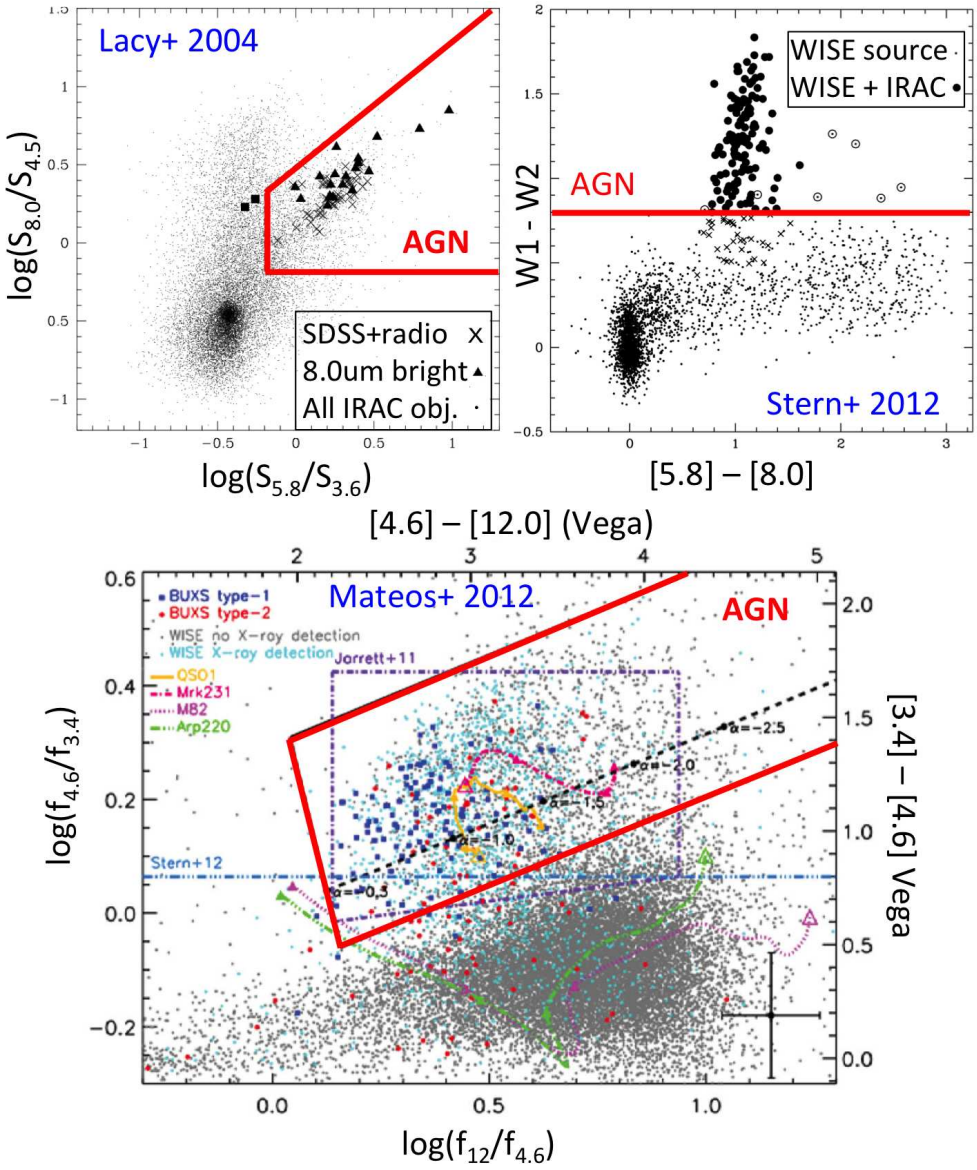

Figure 1.2: Mid-IR diagnostics for Distinguishing AGNs. Objects within the assorted red regions are determined to be AGNs. **Top Left:** Lacy et al. (2004) Spitzer IRAC diagnostic. Dots are 16,000 random objects observed in all 4 IRAC bands. Crosses are SDSS and radio-selected quasars and triangles are the bright $S_{8.0\mu m}$ sample of obscured AGNs. **Top Right:** Stern et al. (2012) WISE 2 color diagnostic. WISE W1–W2 colors are plotted against Spitzer IRAC [5.8]–[8.0]. Large filled circles are AGN according to both W1–W2 and IRAC colors, large empty circles are AGNs by W1–W2 only, and dots are random WISE sources. **Bottom:** Mateos et al. (2012) WISE 3 color diagnostic. WISE W1–W2 ([3.4]–[4.6]) are plotted against W2–W3 ([4.6]–[12]). The small cyan and grey dots are WISE sources in the Bright Ultra-hard XMM-Newton survey area with and without an X-ray detection at 2–10 keV, respectively. The large symbols are spectroscopically identified XMM AGNs. For more detail, see the paper.

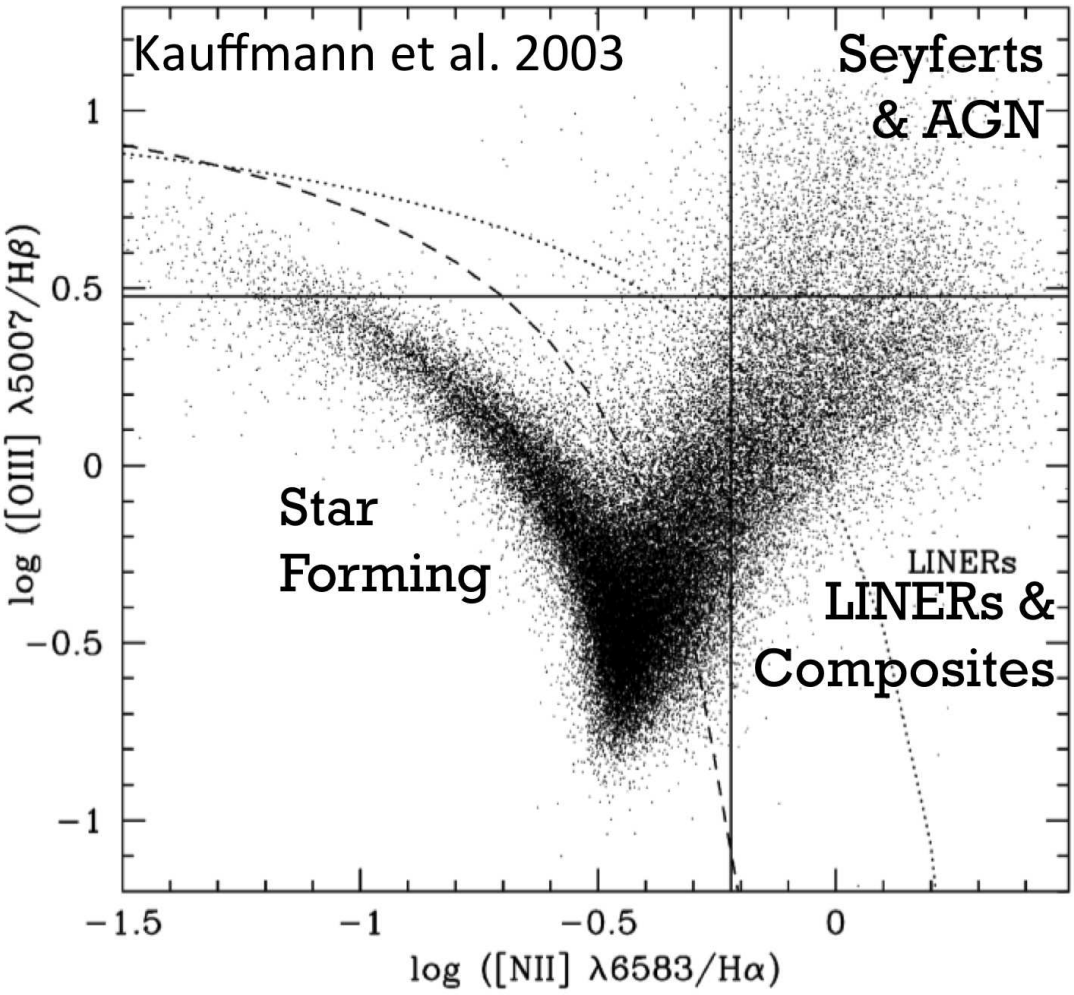

Figure 1.3: Baldwin–Philips–Terlevich diagram in which we plot the emission line flux ratios [O III] λ5008Å/Hβ vs. the ratios [N II] λ6584Å/Hα for a sample of 14,708 low redshift (z<0.3) SDSS galaxies in which all four lines are detected with S/N > 3. The dotted curve shows the dividing line between starburst galaxies and AGNs as defined by Kauffmann et al. (2003).

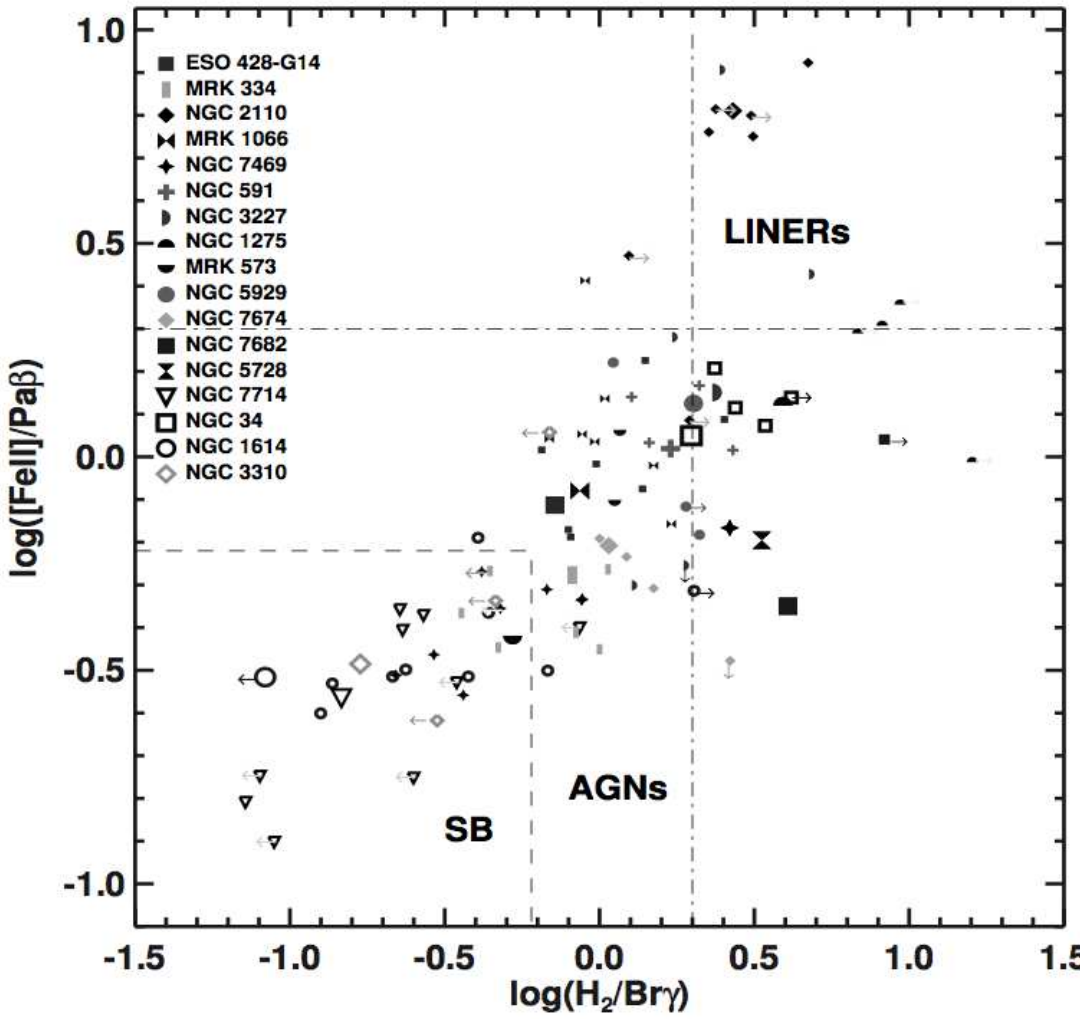

Figure 1.4: Near-infrared AGN/star-formation emission line diagnostic diagrams (Larkin et al., 1998), similar to the optical BPT diagram. Rodríguez-Ardila et al. (2008) plot the emission line flux ratios [Fe II] $\lambda 1.2570\mu$m/Paβ vs. H_2 $\lambda 2.121\mu$m/Brγ of star-forming galaxies and Type 1 and 2 Seyfert AGNs as various symbols; dotted lines mark the star-forming, AGN, and inconclusive/LINER regions of the diagram.

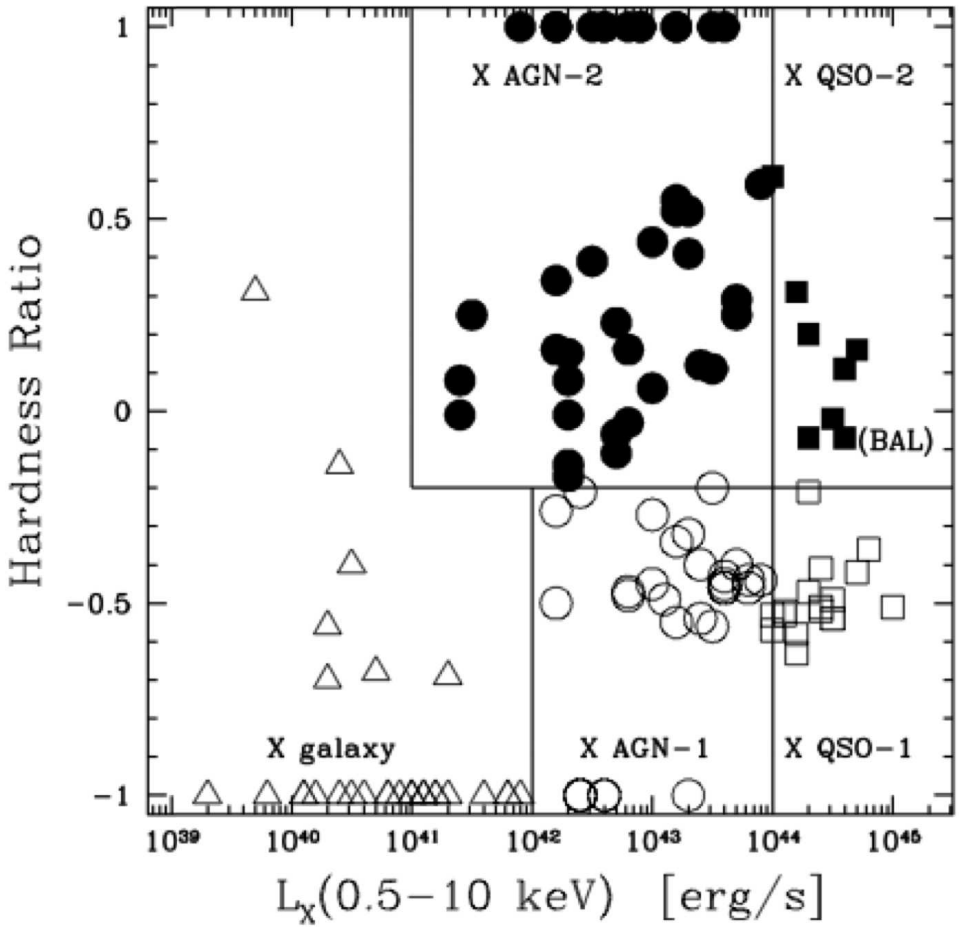

Figure 1.5: Hardness ratio vs. observed X-ray luminosity in the 0.5-10 keV band (Szokoly et al., 2004). Square points correspond to quasars, circular points to AGNs, and triangular points to galaxies. Type 1 and Type 2 AGNs/quasars have open and filled symbols, respectively. Luminosities above 10^{42} ergs s^{-1} indicated that an object's flux is too high to come from star formation, so an AGN must be present.

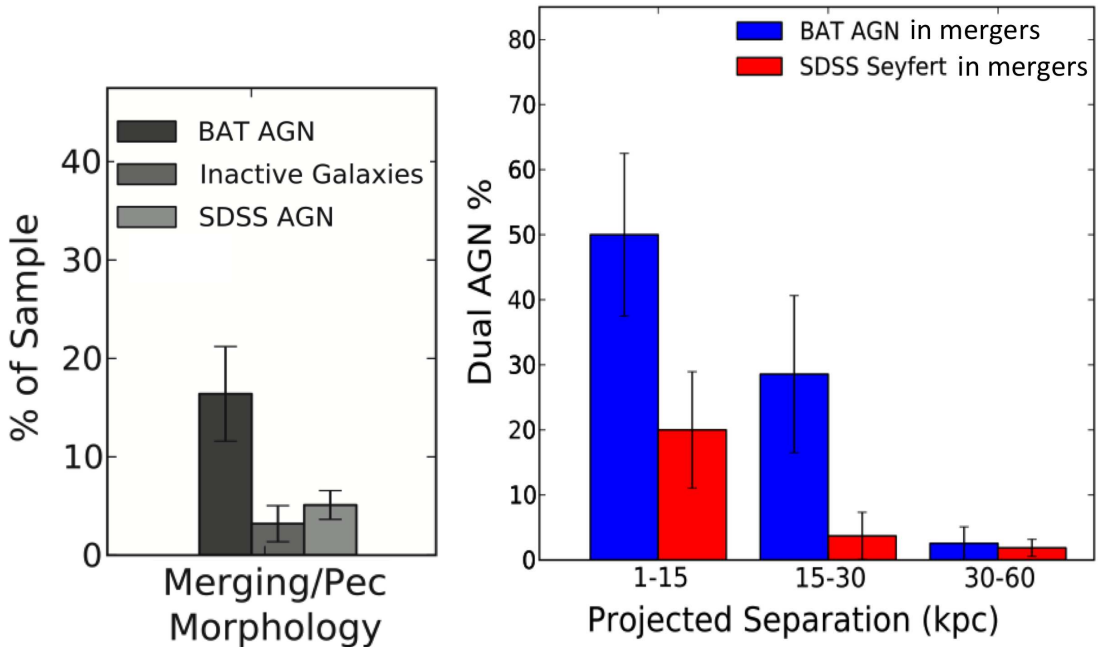

Figure 1.6: **Left**: Koss et al. (2011a) histogram comparing the percentage of BAT AGNs in merging galaxies or in peculiar host galaxies with the similar percentages for mass and redshift-matched control samples of SDSS AGNs and SDSS inactive galaxies (hosting no AGN currently). The percentages for the BAT AGNs, SDSS inactive galaxies, and SDSS AGNs percentage are shown in dark, medium, and light greys, respectively. This illustrates that BAT-detected AGNs are much more likely to be found in mergers than SDSS inactive galaxies or SDSS AGNs. **Right**: Koss et al. (2012) histogram of the fraction of dual AGNs found in galaxy mergers at various projected separation ranges. The blue bars are the fraction of BAT AGN in mergers that have an AGN in each galaxy, and the red bars are the fraction of mass and redshift-matched SDSS AGNs undergoing mergers that have an AGN in the companion galaxy. The fraction of dual AGNs increases at smaller separations in both BAT AGNs and SDSS AGNs, but at a much higher overall rate for the BAT AGNs.

1.4 Current Studies Finding Dual AGNs

As mentioned above, many pairs of AGNs at wide separations (greater than 15 kpc) .

1.5 Outline of Remaining Chapters

In Chapter 2 we present adaptive optics assisted imaging of 140 SDSS AGNs and use the fraction of them found to be spatially double (31%) to speculate on the overall fraction of dual AGNs. In Chapter 3 we introduce the general spectroscopic analysis techniques that will be applied to observations of spatially double candidate dual AGN in our adaptive optics assisted Keck OSIRIS data in Chapter 4 and in our Lick Observatory Shane 3-m Kast Dual Spectograph data in Chapter 5. Chapter 6 summarizes the conclusions of our spectroscopic analysis of the candidates. Chapter 7 discusses our *Chandra* X-ray observations and completes the analysis of one particular candidate that proves to be a dual AGN. Chaper 8 discusses future work to further investigate the results presented here.

We adopt a concordance cosmology with $H_0 = 70$ km s^{-1} Mpc^{-1}, $\Omega_m = 0.28$, and $\Omega_\Lambda = 0.72$ (Hinshaw et al., 2009). Physical scales were calculated using Ned Wright's Cosmology Calculator (Wright, 2006). All quoted wavelengths are in vacuum units, e.g. translating [O III]'s air wavelength of 5007Å to 5008Å.

Part I

Imaging of Candidate Dual AGNs with Double-Peaked [O III]

Chapter 2

Laser Guide Star Adaptive Optics Imaging of Candidate Dual AGNs

As mentioned in the Introduction, confirming the presence of two AGNs in one system is very challenging unless the system has been resolved in previous imaging. Imaging available through the Sloan Digital Sky Survey (SDSS) does not resolve companions at small separations ($<2''$) due to the turbulent blurring of light by the atmosphere. High spatial resolutions are needed to confirm if two bright nuclei are present in the SDSS-unresolved candidate. By measuring and correcting the turbulent blurring effects of the atmosphere with adaptive optics (AO), we can achieve higher spatial resolutions and increased peak intensities, making it possible to resolve pairs of nuclei down to the diffraction limit of the telescope used ($\theta_{\rm diff} = \lambda/{\rm Diameter}_{tel}$).

2.1 Sample Selection

We selected candidate dual AGNs for imaging from the Wang et al. (2009), Smith et al. (2010), and Liu et al. (2010b) catalogs of SDSS Data Release 7 spectroscopic AGNs that show a double-peaked [O III] λ5008Å emission line. Criteria to be considered a double-peaked AGN in Smith et al. (2010) include double-peaked profiles in [O III] λ5008Å and [O III] λ4959Å consistent with the 3:1 intensity ratio fixed by atomic physics, a visual inspection (but no requirement) for double peaks in Hβ, [O II], [Ne III], and [S II] emission lines, and line separations greater than 200 km s^{-1}. Wang et al. selected Type 2 AGNs with z$\leq$0.15, equivalent widths of [O III] λ5008Å greater than 5, peak separations of $\Delta\lambda \geq 1$Å, and peak ratios ranging between 0.3 and 3. Liu et al. required double peaks in both [O III] λ5008Å and [O III] λ4959Å from a sample of galaxies and quasars with z<0.83 and S/N ratios >5 pixel^{-1}. They also required [O III] λ5008Å to be detected at >5σ and with equivalent widths > 4Å, and set the following redshift-dependent line ratio cutoffs: if z>0.33 then [O III]/Hβ >3, or if z<0.33 [O III]/Hβ and [N II]/Hα must be above the Kewley et al. (2001) theoretical limits for star formation excitation. In all three studies, many of their objects also show similar line-splitting in other bright emission lines, such as [O II] λ3728Å and Hβ. Together, Smith et al., Liu et al., and Wang et al. find a total of 340 double-peaked [O III] SDSS AGNs with redshifts between $0.008 < z < 0.686$ and with velocity splittings ranging from 159 to 1400 km s^{-1}.

To this starting list, we applied Laser Guide Star Adaptive Optics (LGS AO) observability requirements, an $r < 17.5$ tip-tilt (TT) star within an arc minute of

the galaxy. We then ranked the targets according to the brightness and separation of their TT stars (which affects the performance of the AO system), the strength of the AGN spectral features ([O III], Hβ) and the galaxy spectral features in their SDSS spectra (which reflects the AGN strength and the contrast between the AGN point stource and the extended galaxy light), and their SDSS magnitude (which determines the signal-to-noise ratio of the final images). Additionally, for our May 2012 observations, seven candidates were selected for observation because Comerford et al. (2012) measured separations greater than $0\farcs3$ between the double emission peaks of the objects using seeing-limited optical long-slit spectroscopy. Measurable separations between their emission lines strengthened these objects as candidate dual AGNs or as AGNs with outflows outflows.

2.2 Imaging Details

The NIRC2 near-infrared (near-IR) camera (PI: Keith Matthews), enhanced by the LGS AO system (Wizinowich et al., 2006), on the Keck II Telescope was used in the wide-camera mode (FOV of $40''$, pixel scale of $0\farcs04$) for most of the imaging campaign. Wide-camera mode was chosen because the increased field of view allows us to sample the environment of the target, fit a WCS solution if more than 3 SDSS targets are present, and potentially image the guide star as a point-spread function reference. Over the three full-nights and four half-nights (two of which were weathered out), we deeply imaged a total of 41 targets; the details are listed in Tables 2.1 and 2.2, and published in Rosario et al. (2010) and McGurk et al. (2015). We used the broadband H

(1.485-1.781μm) filter. A series of short exposures of each candidates' tip-tilt star was taken to develop a point-spread function (PSF) reference. Exposure time ranged from 9 to 34 minutes depending on the brightness of the target and the image depth desired. As is typical in near-IR AO imaging, large numbers of dithered sub-exposures were taken to prevent saturating on the sky background and to remove the effects of flat-field variations over the detector. Sub-exposures were combined in post-processing using the IDL NIRC2 data reduction pipeline (McGurk et al., 2015), modified to robustly handle the very narrow core of the PSF and to use subpixel shifts to stack images into the final mosaic. Our images resolve structures on scales of a kpc or less in all the galaxies.

In addition, Fu et al. (2011a) and Fu et al. (2012) took more shallow NIRC2 snapshots of a total of 100 targets; the details are listed in Tables 2.1 and 2.2. Using the broadband *Kp* (1.948-2.299 μm), Fu et al. took exposures totaling between 1 to 17 minutes. The observations from Fu et al. (2011a) and Fu et al. (2012) were downloaded from the Keck Observatory Archive and processed identically to our images.

Combining these aforementioned NIRC2 images with 2 OSIRIS images, 2 HST ACS images, and 3 HST WFPC2 images, and removing targets imaged twice, creates an imaging sample of 140 double-peaked [O III] emitters. Out of the combined sample, 43 objects (31%) show a second object that lies within $3''$ of the main object. We refer to these objects as having double spatial components or double spatial structure because our images do not prove that the second object is a companion galaxy or an AGN, only that the object has a projected separation of $<3''$, potentially within the aperture of the SDSS fiber. To be responsible for the double-peaked emission lines, the companion must

have been included in the SDSS fiber. We include all companions, with continuum flux ratios major or minor, within this spatially double sample. Images of all 140 objects are shown in Figures 2.1-2.7, separating the objects with double spatial structure (Figures 2.1-2.3) and those with single spatial structures (Figures 2.3-2.7).

Table 2.1: Imaging of Double-peaked [O III] SDSS AGNs with Companions within 3″

SDSS Coordinates:	[O III]			Companion Separation			Exp. Time	UT Observed	Seeing	Refer-
	z	ΔV (km s^{-1})	AGN Type	(″)	(kpc)	Imager	(min)	(yymmdd)	(″)[1]	ence[2]
020011.52−093126.1	0.361	200	1	1.17	5.8	NIRC2/H	1440	090922		S
072554.42+374436.9	0.634	250	1	2.91	19.9	NIRC2/H	1560	090922		S
080315.67+483603.0	0.635	280	1	2.63	18.0	NIRC2/Kp	420	110105	0.6	S
081507.41+430427.0	0.510	500	1	1.95	12.0	NIRC2/Kp	360	110105	0.6	S
083713.48+150037.2	0.141	388	2	1.37	3.4	NIRC2/Kp	480	110106	0.9	L
085841.76+104122.1	0.148	384	2	0.40	1.0	NIRC2/H	800	120519	0.5	W,L
090246.93+012028.2	0.513	240	2	2.71	16.8	NIRC2/Kp	600	110106	0.8	S
090615.92+121845.6	0.644	200	1	0.61	4.2	NIRC2/Kp	448	110105	0.5	S
091646.03+283526.7	0.142	425	2	1.23	3.1	NIRC2/Kp	668	110106	1.0	L
092455.24+051052.0	0.150	410	2	0.44	1.2	NIRC2/Kp	660	110106	1.0	S
094032.25+311328.6	0.170	371	2	2.45	7.1	NIRC2/Kp	840	110106	1.0	L
094236.68+192541.1	0.539	680	1	0.44	2.8	NIRC2/Kp	640	110105	0.5	S
095207.62+255257.2	0.339	475	1	1.00	4.8	NIRC2/H	1380	100105		S
105104.54+625159.3	0.436	360	1	1.52	8.6	NIRC2/Kp	600	110105	0.5	S

Continued on next page

Table 2.1 – *Continued from previous page*

SDSS Coordinates:	[O III]			Companion Separation		Imager	Exp. Time (min)	UT Observed (yymmdd)	Seeing ($''$)[1]	Reference[2]
	z	ΔV (km s^{-1})	AGN Type	($''$)	(kpc)					
110851.04+065901.4	0.182	209	2	0.73	2.2	NIRC2/Kp	192	100604	0.3	L
114642.47+511029.6	0.130	284	2	2.84	6.6	NIRC2/Kp	704	100604	0.4	L
115106.69+471157.7	0.318	490	1	1.29	6.0	NIRC2/Kp	600	110105	0.4	S
115523.74+150756.9	0.287	560	1	0.58	2.5	NIRC2/Kp	352	100603	0.7	S
115714.97+081632.0	0.201	420	2	2.61	8.6	NIRC2/Kp	448	100603	0.7	S
120320.65+131931.3	0.058	296	2	1.91	2.1	NIRC2/Kp	224	100603	0.6	W
123915.40+531414.6	0.202	800	1	1.26	4.2	NIRC2/Kp	896	100604	0.3	S
124037.84+353437.3	0.161	513	2	0.19	0.5	OSIRIS/Hbb	960	100307	0.7	L
124046.63+512902.1	0.597	260	1	1.70	11.0	NIRC2/H	1500	120520	0.5	S
124859.72-025730.8	0.487	345	1	0.53	3.2	NIRC2/Kp	768	100604	0.4	S
124859.72-025730.8	0.487	345	1	0.53	3.2	NIRC2/H	2040	100421	0.8	S
125327.50+254747.4	0.483	680	1	0.72	4.3	NIRC2/Kp	420	110105	0.4	S
130128.76−005804.3	0.246	394	2	1.40	5.4	ACS/F550M	2148	030809		L
130724.08+460400.9	0.353	580	1	2.37	11.6	NIRC2/H	900	100421	0.5	S
130724.08+460400.9	0.352	580	1	2.40	11.7	NIRC2/Kp	448	100604	0.3	S

Continued on next page

Table 2.1 – *Continued from previous page*

SDSS Coordinates:	[O III]			Companion Separation			Exp. Time	UT Observed	Seeing	Reference[2]
	z	ΔV (km s^{-1})	AGN Type	($''$)	(kpc)	Imager	(min)	(yymmdd)	($''$)[1]	
133226.34+060627.3	0.207	420	2	1.58	5.4	NIRC2/Kp	768	100604	0.4	S,L
135024.66+240251.3	0.557	240	1	1.80	11.6	NIRC2/Kp	420	110105	0.4	S
135646.10+102609.0	0.123	413	2	1.32	2.9	NIRC2/Kp	704	100603	0.8	L
140318.10+164959.6	0.455	340	1	1.20	6.7	NIRC2/H	1260	120519	0.4	S
140646.11+234821.0	0.519	310	1	0.90	5.4	NIRC2/H	1320	120519	0.3	S
150243.09+111557.3	0.390	720	1	1.47	7.8	NIRC2/Kp	448	100603	0.7	S
151735.17+214532.5	0.399	500	1	1.10	5.9	NIRC2/Kp	1024	100604	0.4	S
152117.30+075955.4	0.463	500	1	1.30	7.4	NIRC2/H	1200	120520	0.7	S
152327.57+262940.7	0.236	540	2	1.20	4.3	NIRC2/H	1200	120519	0.4	S
154107.81+203608.8	0.508	400	1	2.00	12.3	NIRC2/Kp	448	100604	0.3	S
154107.81+203608.8	0.508	400	1	2.00	12.2	NIRC2/H	560	100421	0.7	S
155634.15+105616.7	0.449	420	1	1.40	7.8	NIRC2/H	960	120520	0.6	S
155645.97+241828.5	0.220	530	1	1.00	3.4	NIRC2/H	1140	120519	0.3	S
161027.41+130806.8	0.229	290	1	2.35	8.6	NIRC2/Kp	192	100604	0.3	S
161027.41+130806.8	0.229	290	1	2.35	8.6	NIRC2/H	540	100421	0.7	S

Continued on next page

Table 2.1 – *Continued from previous page*

SDSS Coordinates:	[O III]			Companion Separation			Exp. Time	UT Observed	Seeing	Reference[2]
	z	ΔV (km s^{-1})	AGN Type	($''$)	(kpc)	Imager	(min)	(yymmdd)	($''$)[1]	
165206.15+310707.6	0.075	310	2	2.96	4.2	NIRC2/Kp	320	100603	0.6	W,L
165603.68+261722.1	0.467	210	1	0.70	1.5	NIRC2/H	1140	120519	0.3	S
172049.25+310646.4	0.095	419	2	0.38	0.7	NIRC2/Kp	384	100603	0.5	L

[1] Blank entries indicate no seeing data was logged by the differential image motion monitor of the Canada-France-Hawaii Telescope on that night, or that the data was taken from space.

[2] Source references — **S** = Smith et al. (2010); **L** = Liu et al. (2010b); and **W** = Wang et al. (2009).

For the systems with double structure, the projected separations between the two galaxy components are listed in Table 2.1 in both arcseconds and kiloparsecs at the SDSS redshift. Figure 2.8 shows the separations between the main galaxy and the companion galaxy, in arc seconds and in kiloparsecs, plotted with respect to the SDSS redshift of the main galaxy. When we plot companion separation in arcseconds, the distribution of galaxies across the space is fairly even across the parameter space. While we do include objects for consideration that have separations out to $3''$, objects with separations greater than $1\farcs5$ are less likely to be dual AGNs since the companion is unlikely to have fallen into the $1\farcs5$ radius SDSS fiber if it is centered on the main galaxy; the exception to this statement is if the fiber was mis-centered between two SDSS-unresolved galaxies undergoing a major merger. In the plot of the companion separations in kiloparsecs versus the redshfit, 40 of the 43 AGNs with possible companions have projected separations of less than 15 kpc. The remaining 3 objects with separations greater than 15 kpc are at higher redshifts; although this is wider than the separation range generally considered to be dual AGN candidates (< 15 kpc), the companions still fall within the $3''$fiber (dashed curve) and thus could be responsible for the double-peaked emission lines.

2.3 Simple Trends

We can use our sample to look for simple characteristic trends; we use bootstrap resampling of 1000 subsamples of 100 galaxies to estimate errors for our percentages. Of the 140 double-peaked emitters imaged, 57 (41%) are Type 1 AGNs and 83

(59%) are Type 2 AGNs. In our sample we find that Type 1 AGNs are 46%±4% spatially double and 54%±4% spatially single, while Type 2 AGNs are 20%±3% spatially double and 80%±3% spatially single. This statistically significant difference (46%±4% Type 1 AGNs are double, versus 20%±3% of Type 2 AGNs) suggests that selecting Type 1 AGNs with double-peaked narrow lines for future dual AGN searches may improve the chances of finding spatially double dual AGN candidates. This in turn increases our chances of building a uniformly selected sample of confirmed dual AGNs.

Table 2.2: Imaging of Double-peaked [O III] SDSS AGNs without Companions within 3″

SDSS Coordinates:	z	[O III] ΔV (km s^{-1})	AGN Type	Imager	Exp. Time (min)	UT Observed (yymmdd)	Seeing (″)[3]	Reference[4]
000249.07+004504.8	0.087	530	2	NIRC2/Kp	192	110105	0.6	W,L
000656.85+154847.9	0.125	386	2	NIRC2/Kp	300	110105	0.7	W
011802.94−082647.2	0.137	350	2	NIRC2/H	630	090922		S
013555.82+143529.7	0.072	272	2	NIRC2/Kp	960	090911		W,L
014209.01−005050.0	0.133	248	2	NIRC2/Kp	240	110105	0.7	W
040001.59−065254.1	0.171	392	2	NIRC2/Kp	480	090911		L
073509.49+403624.3	0.103	260	2	NIRC2/Kp	420	110105	0.7	W
073656.47+475946.8	0.096	251	2	NIRC2/Kp	240	110105	0.7	L
073849.75+315611.9	0.297	297	2	NIRC2/Kp	240	110105	0.7	L
074129.66+392835.9	0.210	480	2	NIRC2/Kp	240	110105	0.6	S
074729.76+344018.1	0.130	322	2	NIRC2/Kp	240	110105	0.6	W
080740.99+390015.2	0.023	609	2	WFPC2/F606W	500	950226		W
080841.21+481351.9	0.124	340	2	NIRC2/Kp	720	110106	0.6	S,W
081542.53+063522.9	0.244	280	1	NIRC2/H	1140	090922		S
082107.89+502115.8	0.095	342	2	NIRC2/Kp	600	110106	0.9	W,L

Continued on next page

Table 2.2 – *Continued from previous page*

SDSS Coordinates:	z	[O III] ΔV (km s^{-1})	AGN Type	Imager	Exp. Time (min)	UT Observed (yymmdd)	Seeing ($''$)[3]	Reference[4]
082357.80+391630.9	0.166	700	1	NIRC2/Kp	420	110105	0.5	S
082857.99+074255.7	0.554	300	2	NIRC2/H	1000	100105		S
084130.18+393119.2	0.132	326	2	NIRC2/Kp	480	110106	1.0	L
084227.46+054716.4	0.275	486	2	NIRC2/Kp	480	110106	0.8	L
085358.65+233911.4	0.113	223	2	NIRC2/Kp	480	110106	0.9	L
090753.98+141509.2	0.120	290	2	NIRC2/Kp	900	110106	0.8	L
090947.85+312443.6	0.264	1050	1	NIRC2/Kp	360	110105	0.5	S
090958.32+085542.2	0.159	240	2	NIRC2/Kp	720	110106	0.9	S
091649.41+000031.5	0.222	310	1	NIRC2/H	1150	100105		S
091654.09+521723.0	0.219	315	1	NIRC2/Kp	424	110105	0.5	S
094100.81+143614.4	0.383	870	2	NIRC2/Kp	480	110106	1.2	S
094124.02+394441.8	0.108	440	2	WFPC2/F555W	600	990426		W
094144.83+575123.6	0.159	410	1	NIRC2/Kp	420	110105	0.5	S
095833.20−005118.6	0.086	406	2	NIRC2/Kp	480	110106	1.2	W,L
095833.98+251235.4	0.116	335	2	NIRC2/Kp	480	110106	0.9	L
095920.52+422141.7	0.153	297	2	NIRC2/Kp	480	110106	0.8	L

Continued on next page

Table 2.2 – *Continued from previous page*

SDSS Coordinates:	z	[O III] ΔV (km s^{-1})	AGN Type	Imager	Exp. Time (min)	UT Observed (yymmdd)	Seeing ($''$)[3]	Reference[4]
095942.61+261914.2	0.051	248	2	NIRC2/H	1200	120520	0.5	L
100145.30+283330.3	0.116	550	2	NIRC2/Kp	480	110106	0.8	S
100654.20+464717.2	0.123	293	2	NIRC2/Kp	480	110106	0.8	L
101241.20+215556.0	0.111	210	1	NIRC2/Kp	420	110105	0.5	S
102004.36+324342.5	0.484	340	1	NIRC2/Kp	420	110105	0.5	S
102325.57+324348.4	0.127	386	2	NIRC2/H	1200	120519	0.4	W
103138.67+380651.7	0.492	730	1	NIRC2/Kp	540	110105	0.5	S
104257.96+385347.2	0.107	440	2	NIRC2/H	1140	120520	0.6	S,L
105052.46+083934.8	0.169	324	2	NIRC2/Kp	540	110106	0.9	L
111013.20+053338.8	0.152	830	1	NIRC2/Kp	600	110105	0.4	S
112659.54+294442.8	0.102	318	2	NIRC2/Kp	120	110106	0.9	W,L
112907.10+575605.4	0.313	337	2	NIRC2/Kp	540	110106	0.9	L
113020.99+022211.5	0.241	330	1	NIRC2/Kp	576	110105	0.4	S
113045.33+505509.1	0.592	270	1	NIRC2/Kp	420	110105	0.4	S
113105.07+610405.1	0.338	330	1	NIRC2/Kp	636	110105	0.4	S
113257.84+604653.6	0.233	330	1	NIRC2/Kp	360	110105	0.3	S

Continued on next page

Table 2.2 – *Continued from previous page*

SDSS Coordinates:	z	[O III] ΔV (km s^{-1})	AGN Type	Imager	Exp. Time (min)	UT Observed (yymmdd)	Seeing ($''$)[3]	Reference[4]
114852.65+151415.8	0.113	260	1	NIRC2/Kp	360	110105	0.4	S
114908.49+144547.0	0.595	200	1	NIRC2/Kp	420	110105	0.4	S
115249.33+190300.3	0.097	318	2	NIRC2/Kp	448	100603	0.6	W,L
120240.68+263138.6	0.476	450	1	NIRC2/Kp	192	100604	0.4	S
120343.22+283557.8	0.374	850	1	NIRC2/H	1200	120520	0.4	S,W,L
121911.16+042905.9	0.555	480	1	NIRC2/H	720	100421	0.8	S
121911.16+042905.9	0.555	480	1	NIRC2/Kp	64	100603	0.7	S
121957.51+190003.5	0.117	417	2	NIRC2/Kp	448	100603	0.6	L
131106.74+195234.2	0.156	319	2	NIRC2/Kp	448	100603	0.7	L
131235.96+500415.8	0.116	390	2	NIRC2/Kp	128	100604	0.4	W
132104.59−001445.8	0.082	330	2	NIRC2/Kp	448	100603	0.7	L
140231.58+021546.4	0.180	308	2	NIRC2/Kp	448	100603	0.7	L
140534.85+244735.0	0.130	307	2	NIRC2/Kp	224	100604	0.4	L
140845.73+353218.5	0.166	374	2	NIRC2/Kp	448	100603	0.7	L
140923.51−012430.5	0.405	270	1	NIRC2/H	1020	100421	0.4	S
143135.43−011159.8	0.560	490	1	NIRC2/H	1140	120519	0.4	S

Continued on next page

Table 2.2 – *Continued from previous page*

SDSS Coordinates:	z	[O III] ΔV (km s^{-1})	AGN Type	Imager	Exp. Time (min)	UT Observed (yymmdd)	Seeing ($''$)[3]	Reference[4]
144012.74+615633.0	0.275	800	1	NIRC2/Kp	448	100603	0.7	S
144157.24+094859.1	0.220	810	2	NIRC2/Kp	320	100604	0.4	S
144804.17+182537.9	0.038	251	2	NIRC2/H	1200	120519	0.5	L
145156.82+301602.7	0.158	513	2	NIRC2/Kp	320	100603	0.8	L
145408.36+240521.3	0.535	400	1	NIRC2/H	1140	120519	0.4	S
145717.69+110412.4	0.462	200	1	NIRC2/H	1200	120520	0.7	S
150125.57+111356.6	0.151	940	1	NIRC2/H	1200	120520	0.8	S
150437.67+541149.6	0.305	700	1	NIRC2/Kp	224	100603	0.7	S
150452.34+321414.8	0.113	254	2	NIRC2/Kp	384	100603	0.8	W
151659.24+051751.5	0.051	324	2	NIRC2/Kp	160	100604	0.5	W,L
151757.36+114452.6	0.227	400	2	NIRC2/Kp	320	100603	0.7	S
151842.95+244026.0	0.561	280	2	NIRC2/H	1200	120520	0.6	S
152431.41+323750.6	0.629	350	2	NIRC2/H	1620	120520	0.7	S
152606.15+414014.4	0.008	285	2	WFPC2/F606W	500	940828		W
153231.80+420342.7	0.209	300	1	NIRC2/Kp	448	100604	0.4	S
153231.80+420342.7	0.209	300	1	NIRC2/H	600	100421	0.6	S

Continued on next page

Table 2.2 – *Continued from previous page*

SDSS Coordinates:	z	[O III] ΔV (km s^{-1})	AGN Type	Imager	Exp. Time (min)	UT Observed (yymmdd)	Seeing ($''$)[3]	Reference[4]
153301.43+070513.7	0.354	510	1	NIRC2/H	600	120519	0.4	S
155009.59+080838.8	0.232	400	2	NIRC2/Kp	128	100604	0.3	L
155619.30+094855.6	0.068	410	2	NIRC2/H	1020	120520	0.6	W,L
160027.78+083743.0	0.227	420	2	NIRC2/Kp	320	100604	0.3	L
160436.21+500958.1	0.146	367	2	NIRC2/Kp	320	100604	0.3	W,L
160631.37+273643.0	0.158	319	2	NIRC2/Kp	128	100604	0.4	L
160659.57+083514.6	0.187	380	2	NIRC2/H	630	120520	0.6	S
161826.93+081950.7	0.446	340	1	NIRC2/Kp	160	100603	0.6	S
161847.93+215925.4	0.334	320	1	NIRC2/Kp	160	100603	0.6	S
162345.20+080851.1	0.199	470	2	NIRC2/H	540	120520	0.6	S,L
162939.58+240856.0	0.059	257	2	NIRC2/H	630	120520	0.6	W
163056.75+164957.2	0.034	295	2	NIRC2/Kp	192	100604	0.5	L
163316.03+262716.3	0.071	312	2	NIRC2/Kp	320	100603	0.6	W
163316.03+262716.3	0.071	312	2	NIRC2/H	1050	100831	0.6	W
171544.02+600835.4	0.157	350	2	NIRC2/Kp	320	100603	0.6	S,L
171930.56+293412.8	0.180	1000	1	NIRC2/Kp	160	100603	0.6	S

Continued on next page

Table 2.2 – *Continued from previous page*

SDSS Coordinates:	z	[O III] ΔV (km s^{-1})	AGN Type	Imager	Exp. Time (min)	UT Observed (yymmdd)	Seeing ($''$)[3]	Reference[4]
210449.13−000919.1	0.135	380	2	NIRC2/H	660	120519	0.5	S
230442.82−093345.3	0.032	319	2	NIRC2/Kp	320	100603	0.7	W,L
231051.95−090011.9	0.094	327	2	ACS/F606W	720	050819		W,L
233313.17+004911.8	0.170	444	2	NIRC2/Kp	384	100603	0.7	L
235256.62+001155.2	0.167	310	2	NIRC2/Kp	384	100604	0.5	L

[3] Blank entries indicate no seeing data was logged by the differential image motion monitor of the Canada-France-Hawaii Telescope on that night, or that the data was taken from space.

[4] Source references — **S** = Smith et al. (2010); **L** = Liu et al. (2010b); and **W** = Wang et al. (2009).

By cross-referencing our list of double peaked emitters to the Faint Images of the Radio Sky at Twenty Centimeters (FIRST) radio catalog (Becker et al., 1995; Helfand et al., 2015), we can classify all but three of our AGNs as radio-detected or undetected; the excluded three objects (SDSS J000656.85+154847.9, SDSS J013555.82-+143529.7, and SDSS J040001.59−065254.1) are spatially single AGN that fall outside of the coverage footprint of the FIRST survey. 60 (42%) of the 137 AGNs are radio-detected by the FIRST survey, and 77 (58%) are radio-undetected. When broken in spatially double and spatially single subgroups, the fraction of radio-detected (42% and 43%, respectively) are similar to the fraction for the entire sample. While radio-detected AGNs are frequently associated with disturbed emission line regions caused by interactions with radio jets (Wilson & Willis, 1980; Whittle & Wilson, 2004; Rosario et al., 2010), our sample shows no trend between being radio-detected/undetected and having or lacking a companion within $3''$. It should be noted that the lack of a FIRST detection does not indicate a total absence of radio flux or of radio jets. High-redshift objects with no FIRST detection may have marginal flux which could have been detected at lower redshifts; additionally, the orientation of the radio source can affect the flux detected. Therefore, some objects with radio jets may fall below the FIRST detection limit, skewing our results.

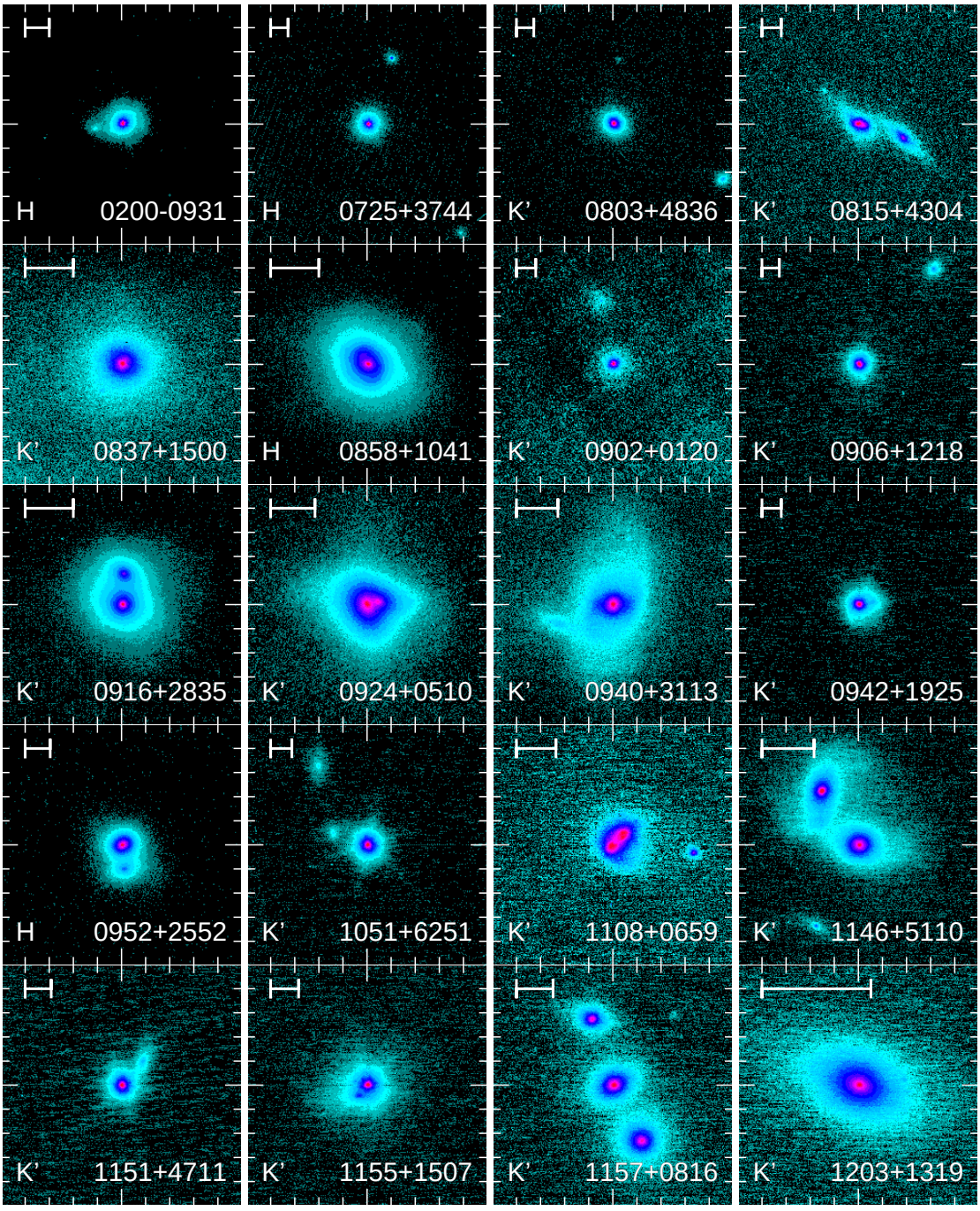

Figure 2.1: Keck NIRC2 images of spatially double SDSS double-peaked [O III] AGN, taken with Laser Guide Star Adaptive Optics. Each $10''\times10''$ wide camera image ($0\farcs04$ pixel^{-1}) is displayed on a log colorscale. North is up and East is left. The scalebar in the top left corner of each image corresponds to 5 kpc at the redshift of the system, and the filter used for each object is indicated in the lower left corner. The original images were downloaded from the Keck Observatory Archive (PIs: Claire Max and George Djorgovski) and reprocessed. These objects have double structures with separations less than $3''$, which means they are candidate dual AGNs.

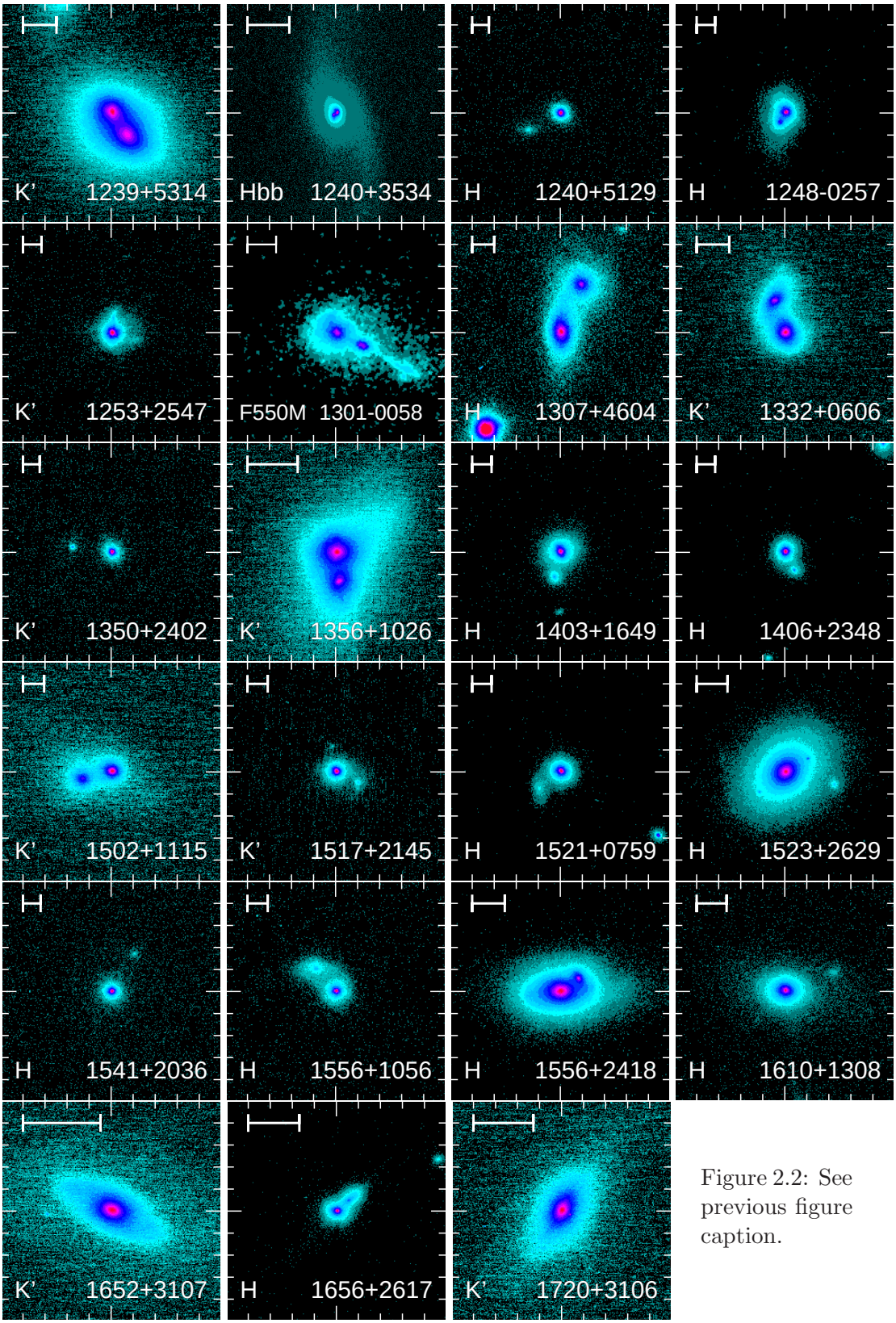

Figure 2.2: See previous figure caption.

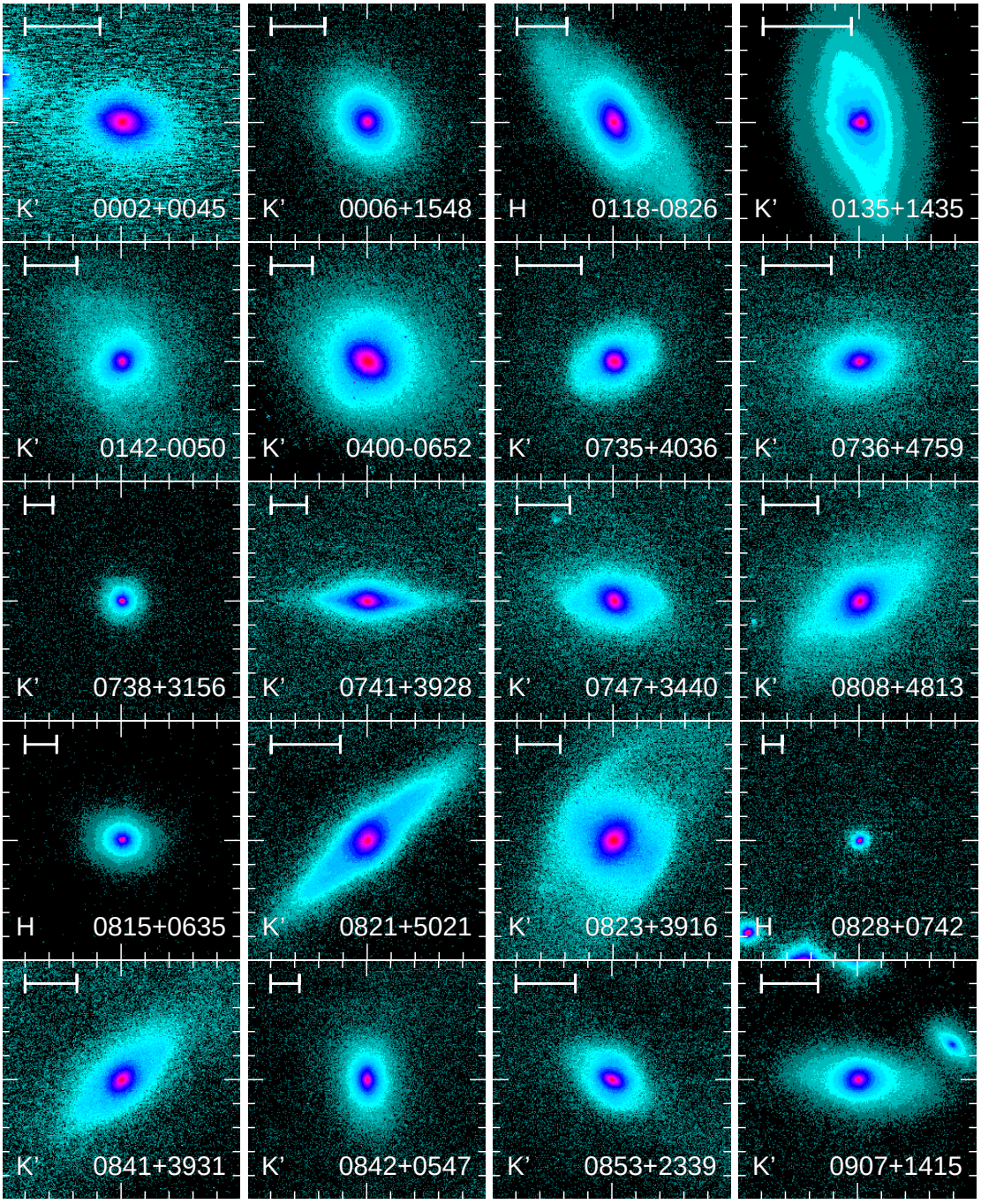

Figure 2.3: Keck NIRC2 images of spatially single SDSS double-peaked [O III] AGN, taken with Laser Guide Star Adaptive Optics. This Figure is continued on Figures 2.4–2.7. Each $10'' \times 10''$ image is displayed on a log colorscale. N is up and E is left. The scalebar in the top left corner of each image corresponds to 5 kpc at the redshift of the system, and the filter used for each object is indicated in the lower left corner. The original images were downloaded from the Keck Observatory Archive (PIs: Claire Max and George Djorgovski) and reprocessed. These objects show single spatial structures; their double [O III] lines are likely due narrow line region kinematics, outflows, jets, rings of star formation, or an unresolved close pair of AGNs.

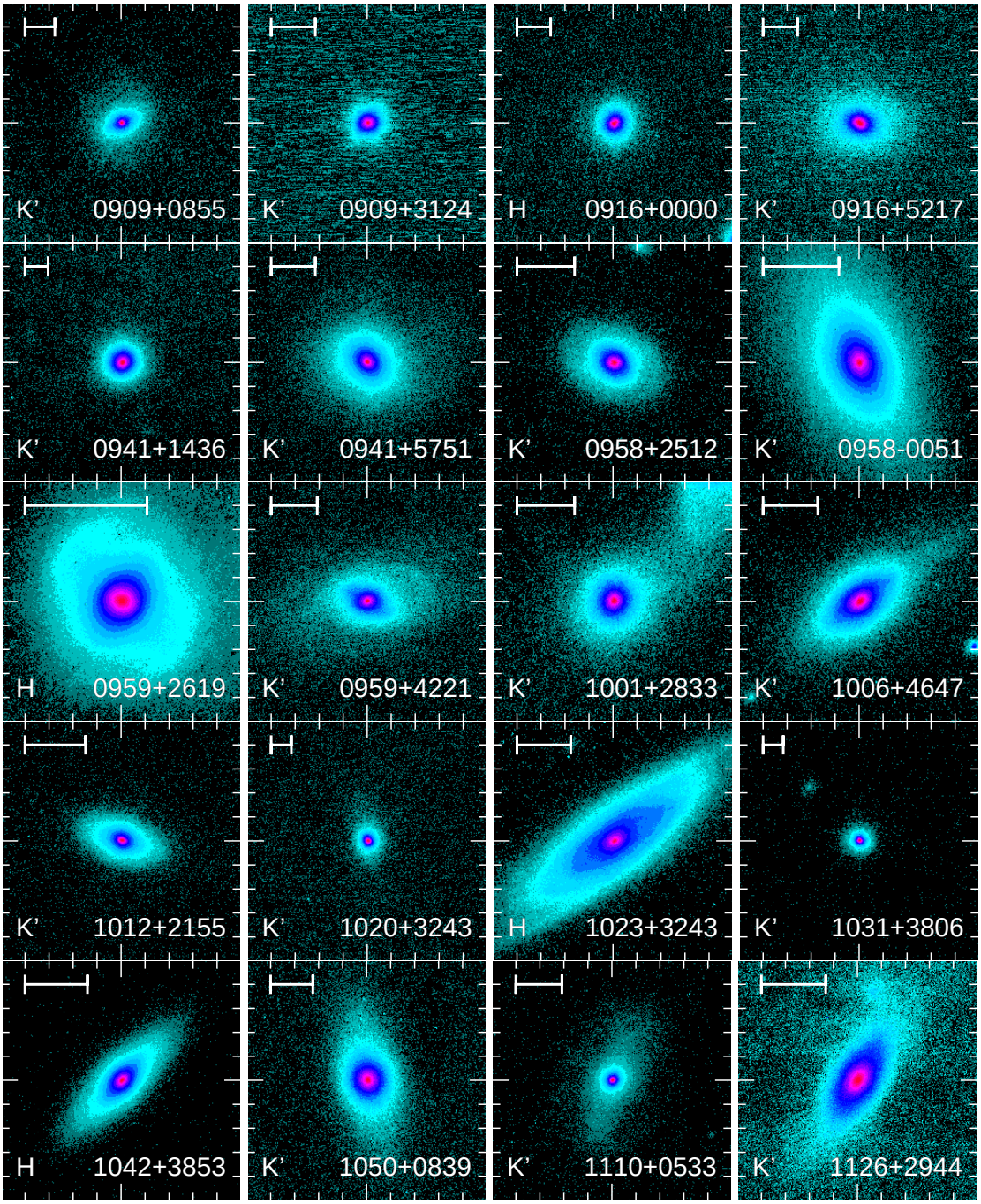

Figure 2.4: Continued from Figure 2.3, onto Figures 2.5–2.7. Keck NIRC2 images of spatially single SDSS double-peaked [O III] AGN, taken with Laser Guide Star Adaptive Optics. These objects show single spatial structures; their double-peaked [O III] lines are likely due narrow line region kinematics, outflows, jets, rings of star formation, or an unresolved close pair of AGNs.

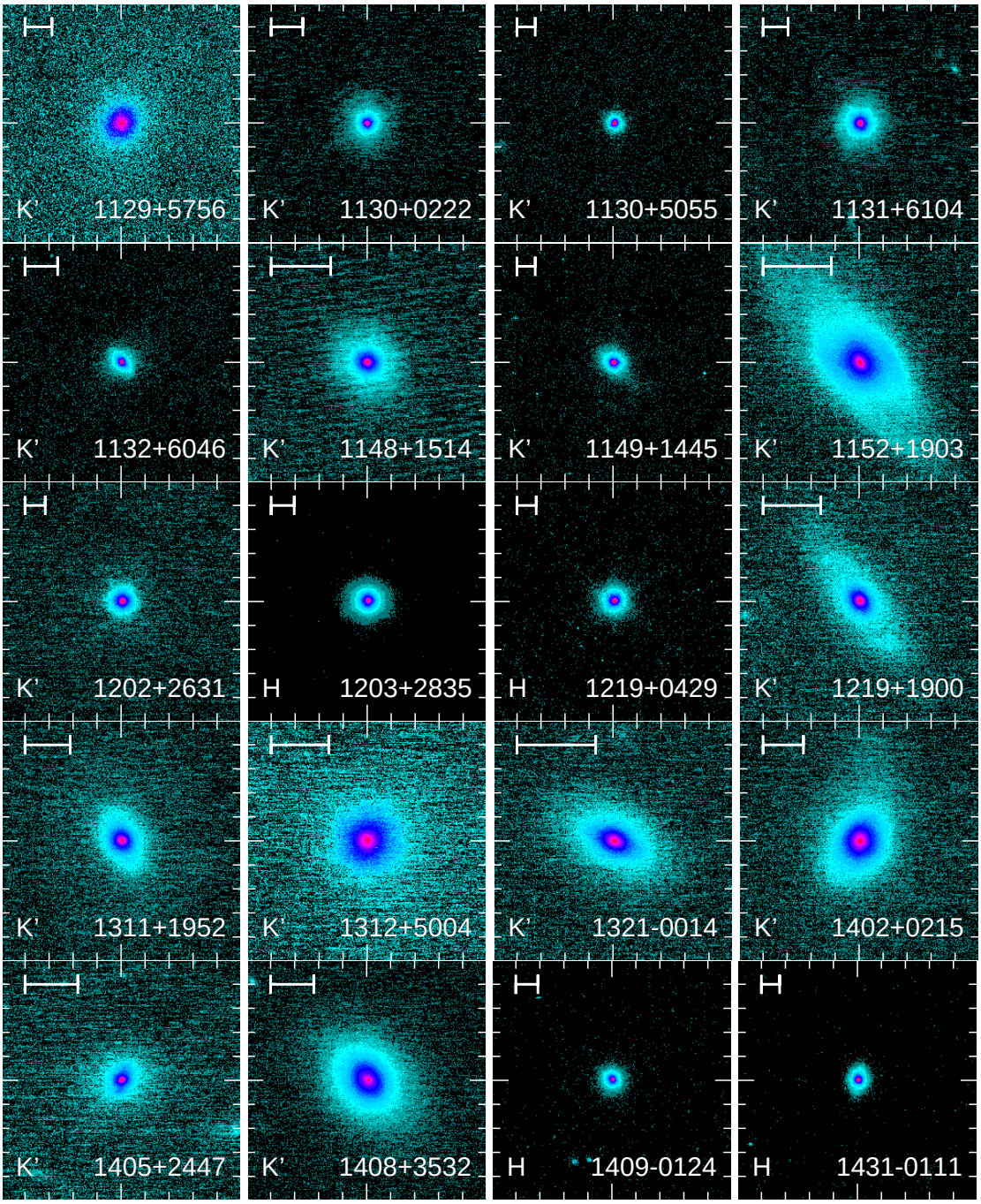

Figure 2.5: Continued from Figures 2.3–2.4, onto Figures 2.6–2.7. Keck NIRC2 images of spatially single SDSS double-peaked [O III] AGN, taken with Laser Guide Star Adaptive Optics. These objects show single spatial structures; their double-peaked [O III] lines are likely due narrow line region kinematics, outflows, jets, rings of star formation, or an unresolved close pair of AGNs.

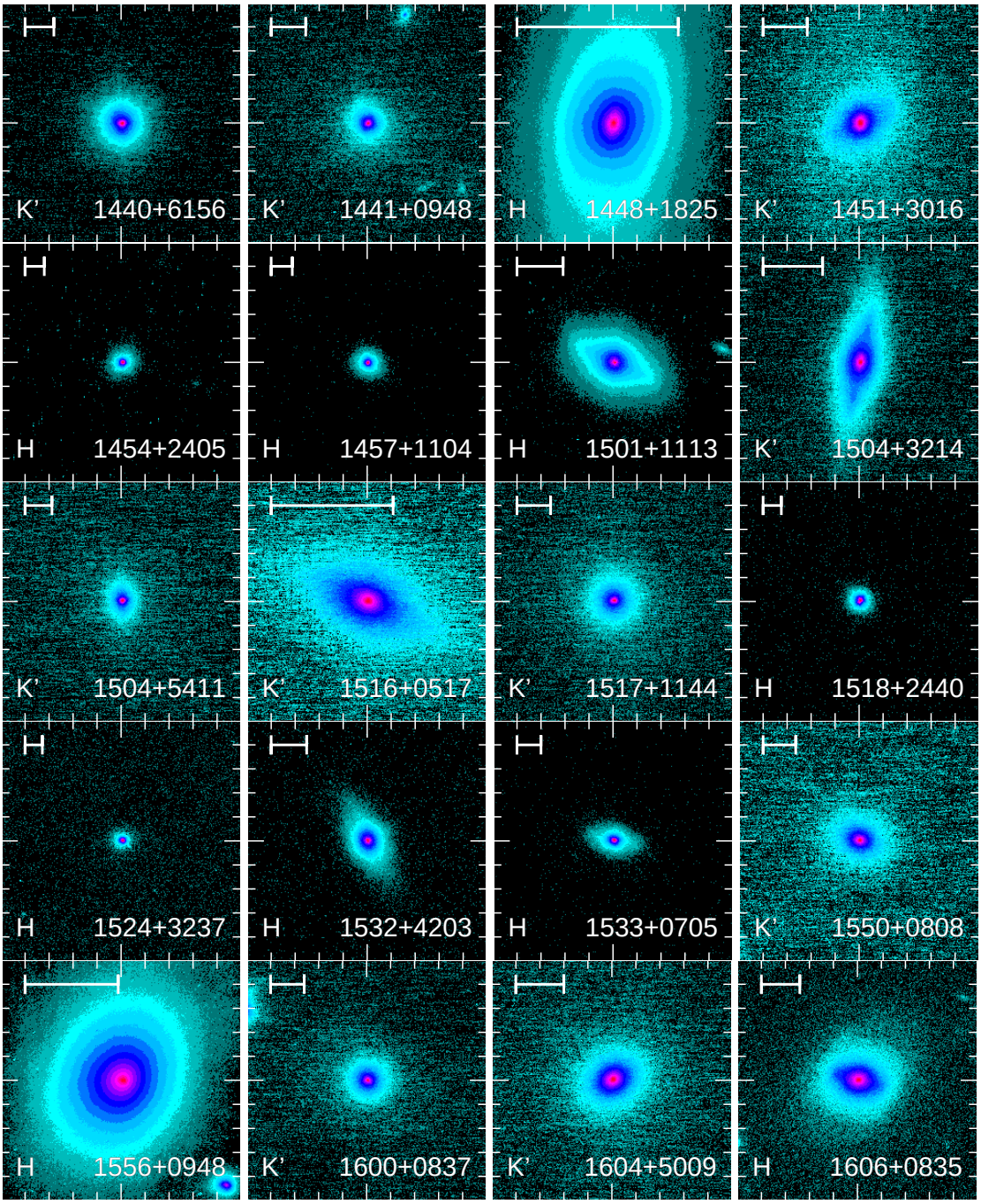

Figure 2.6: Continued from Figures 2.3–2.5, onto Figure 2.7. Keck NIRC2 images of spatially single SDSS double-peaked [O III] AGN, taken with Laser Guide Star Adaptive Optics. These objects show single spatial structures; their double-peaked [O III] lines are likely due narrow line region kinematics, outflows, jets, rings of star formation, or an unresolved close pair of AGNs.

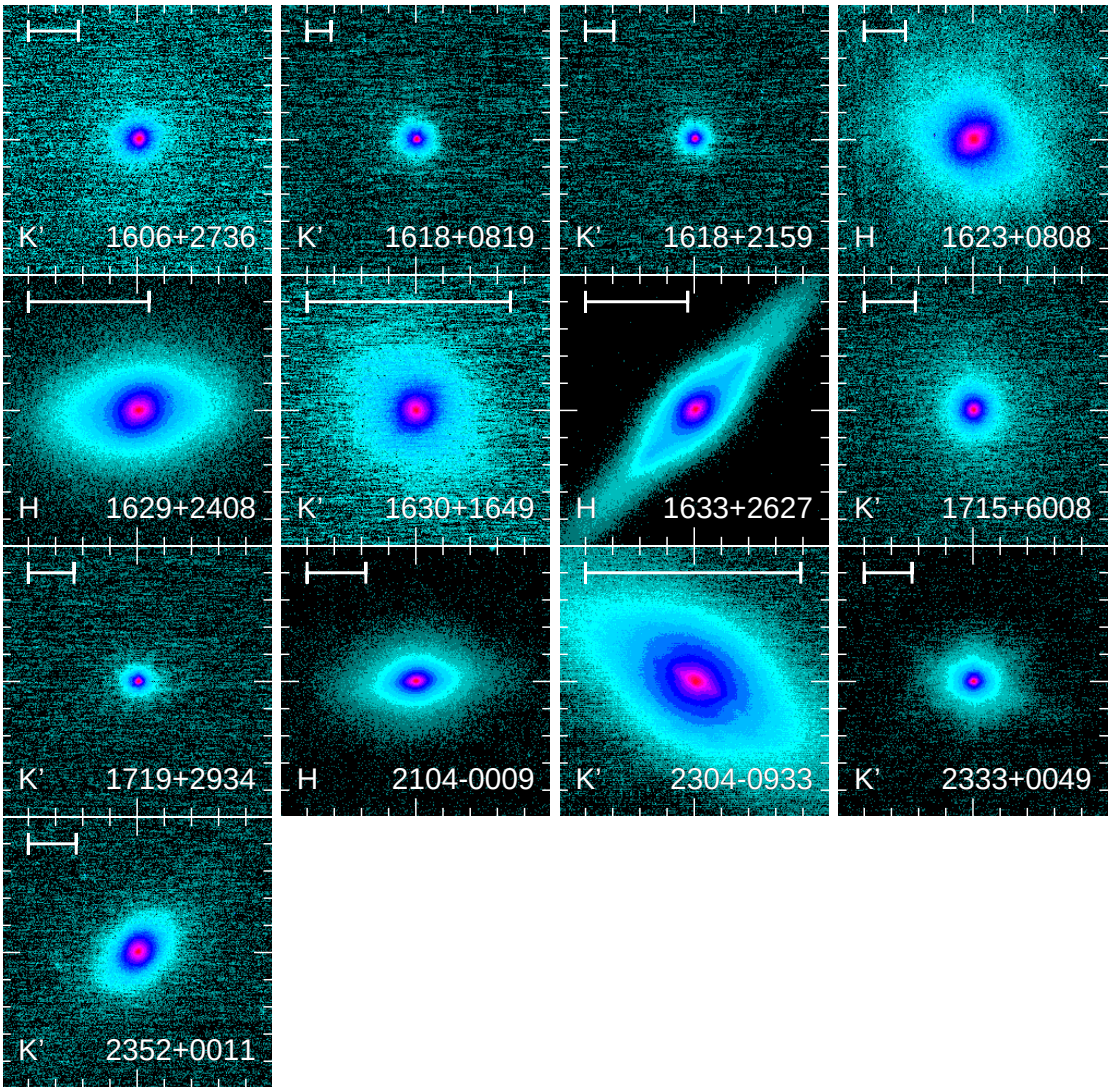

Figure 2.7: Continued from Figures 2.3–2.6. Keck NIRC2 images of spatially single SDSS double-peaked [O III] AGN, taken with Laser Guide Star Adaptive Optics. These objects show single spatial structures; their double-peaked [O III] lines are likely due narrow line region kinematics, outflows, jets, rings of star formation, or an unresolved close pair of AGNs.

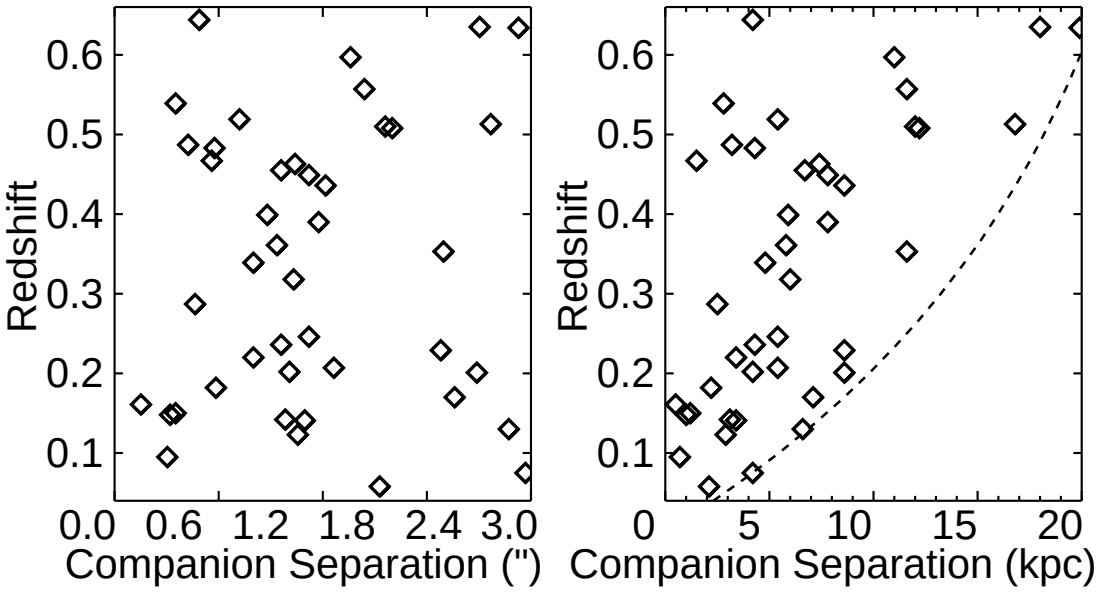

Figure 2.8: Companion separations versus redshift of the 43 SDSS AGNs with separations less than 3″ between the main galaxy and the companion galaxy. *(left)* Companion separations measured in arc seconds. This distribution is fairly uniform. While we do include for consideration objects with separations out to 3″, objects with separations greater than 1.″5 are less likely to be dual AGNs since the companion is unlikely to have fallen into the 1.″5 radius fiber centered on the main galaxy; the exception to this statement is if the fiber was centered between two galaxies undergoing a major merger. *(right)* Companion separations measured in kiloparsecs. Scaling the 3″ SDSS fiber to the projected separation with redshift creates the dashed curve. 40 of these 43 AGNs have a possible companion with a projected separation of less than 15 kpc. The remaining 3 objects are at higher redshifts; the companions still fall within the 3″fiber and thus could be responsible for the double-peaked emission lines.

2.4 Fraction of AGNs with Dual SMBHs

The SDSS spectra and our selection criteria guarantee that there is one AGN present in all of our objects, spatially double or spatially single. In our spatially double sample, we will need further observations to prove if the companion object near the main AGN actually contains a second AGN as hinted by the second [O III] emission peak. However, we can use our data to place some upper limits on the fraction of AGN pairs separated by <20 kpc and detectable by SDSS double-peaked [O III] emission lines.

The two peaks of the [O III] λ5008Å line imply that there could be two AGNs present in our targets. Assuming that the companion object of each spatially double candidate is a galaxy hosting an AGN, the fraction of our targets that are spatially double places an upper limit on the fraction of dual AGNs with double-peaked emission lines. From our imaging data, the upper limit fraction of double-peaked AGN pairs with separation scales of 0.5–20 kpc is 31%±3%. Additionally, Smith et al. (2010), Liu et al. (2010b), and Ge et al. (2012) independently conclude that roughly 1% of SDSS AGNs have double-peaked emission lines. Stringing these statements together results in the conclusion that 0.3% of SDSS AGNs (1 in 300 AGNs) have both double-peaked emission lines and have a second object, possibly a galaxy hosting an AGN, near the main AGN, and thus could contain two AGNs.

2.5 Statistical Identity of the Companions

Chance alignments with background or foreground galaxies are not a likely explanation for the companions that we find around our QSOs. As calculated in Decarli et al. (2010), the probability of a chance superposition for two AGNs with separations $< 1\farcs5$ with $0.35 < z < 0.45$ is $\sim 2 \times 10^{-7}$, which is negligible with respect to the number of SDSS DR7 AGNs in this redshift range (~ 3300). However, this prediction applies to one specific redshift and separation range and for pairs of AGNs only. To characterize the likelihood of a chance superposition of objects near an SDSS, a useful exercise would be to take all SDSS AGNs with appropriate redshifts and cross-correlate them with the HST and Keck NIRC2 archives to get high resolution images for as many AGNs as possible. By visually inspecting this sample, we could determine fraction of normal AGNs with a faint neighbor within 15 kpc. This would allow us to determine if selecting candidates with double-peaked [O III] enhances the fraction of close companions found. We submitted the ∼88,000 AGNs in SDSS Data Release 4 to the HST archives, and found that 208 (0.2%) of the AGNs have archival HST observations. At least 25 of these objects are follow-up observations of AGNs with double-peaked [O III]. This exercise is currently challenging with the Keck Observatory Archive as it takes hours to search for observations of a list of 999 objects, let alone the ∼88,000 objects. In the 8,000 AGNs submitted to the Keck Archive, only 1 (0.01%) returned with imaging data, and it was a double-peaked [O III] AGN.

Rosario et al. (2011) has already performed an abbreviated version of this search in order to estimate the fraction of normal QSOs with faint neighbors. Rosario

et al. examined a set of Hubble Space Telescope (HST) Near Infrared Camera and Multi-Object Spectrometer (NICMOS) images of 28 QSOs published as part of the QUEST survey. Despite the median redshift of the QUEST QSOs being lower than ours (~ 0.14, as compared to 0.35 for our NIRC2 sample), we use this homogenous, high-resolution, deep H-band imaging data set of normal QSOs to compare and estimate the fraction of faint neighbors. Since only 1% of AGN have double-peaked emission lines, we assume that the QUEST QSOs are primarily normal QSOs that would not have made it into the Smith et al., Wang et al., and Liu et al. catalogues, and that there has not been major evolution in the host galaxy properties between $z \sim 0.1$ and $z \sim 0.4$. From an examination of the QUEST images, Rosario et al. determined that approximately 35% of 22 radio-quiet QSOs have a fainter companion within 15 kpc, but only 2 ($\sim$9%) show obvious spatially resolved signs of merger activity. Our double-peaked AGN sample has roughly the same fraction of spatially double objects, although a much higher fraction of mergers. Assuming that the statistics for the QUEST sample apply to the SDSS parent population of AGNs, we conclude that some or all of the doubles with minor merger ratios in our sample may arise from satellite galaxies around AGN host galaxies. If these satellites also host AGNs, then the double-peaked narrow lines may indeed come from two separate active nuclei. However, it is also possible that the double-peaked structure in the minor doubles could come solely from the active nucleus containing the AGN, as in the 69% of the NIRC2 sample that do not show double structure. Without additional information, we are unable to differentiate between these two possible explanations for our spatially double objects.

2.6 Conclusions

From a sample of Type 1 and 2 SDSS AGNs that display double-peaked emission lines in [O III] λ5008Å, we identify double spatial structure in 43 objects of 140 (31%) primarily using Keck NIRC2 LGS AO imaging. Our statistics suggest that Type 1 AGNs are approximately twice as likely to be spatially double as Type 2 AGNs, suggesting that selecting Type 1 AGNs for future dual AGN searches may improve the chances of finding spatially double dual AGN candidates. While radio-detected AGNs are often associated with radio jets interacting with and disturbing emission line regions, our sample shows no trend between radio detection or non-detection and the presence or absence of a companion within $3''$. Our calculated upper limit for the fraction of dual SDSS AGNs selected via double-peaked [O III] is 0.31%$\pm$0.03%, which roughly agrees with the values of Blecha et al. (2013).

Part II

Spectroscopic Confirmation

Chapter 3

Introduction to Spectroscopic Confirmation of Candidate Dual AGNs

Confirming dual spatial structure as in Chapter 2 is an important first step to determining if a double-peaked [O III] target is a dual AGN. The next steps are to investigate if the companion is responsible for one of the double [O III] peaks and to confirm if there is an AGN present in the companion as well as the main AGN.

Unfortunately, many of the techniques mentioned in the Introduction for confirming dual AGNs are observationally expensive for large samples of candidate dual AGNs or, in the case of X-ray observations, lack the spatial resolution to distinguish the galaxy pairs with small separations. The spatial and spectral resolution afforded by long-slit and integral field spectroscopy can be leveraged instead; by spectrally sep-

arating the double-peaked emission, we can determine if the emission lines come from spatially separated regions along the slit (e.g., Comerford et al., 2012; Liu et al., 2010a; Fu et al., 2012). While fairly expensive, integral field spectroscopy provides an extra dimension of spatial information, in addition to the spectral information, that is extremely helpful in determining the source of the double emission lines. Since we also have images of the potential galaxy pairs, we can orient the long-slit or integral field unit along the pair of objects, to better distinguish each object's identity (Liu et al., 2010a).

In the following chapters, we present IFU and long-slit spectroscopy for 13 of our candidate dual AGNs, in order to confirm or disprove them as dual AGNs. Section 3.1, below, discusses the analysis techniques in common between our IFU and long-slit spectroscopy results, and briefly summarizes the results. In Chapter 4, we describe our spectroscopic observations (Section 4.1) and data reduction (Section 4.2) for 4 spatially double candidates performed using laser guide star adaptive optics assisted integral field spectroscopy from Keck Observatory's OH Suppressing InfraRed Spectrograph (OSIRIS). In Section 4.3, we match resolved spatial components seen in our imaging to the double-peaked emission lines observed with OSIRIS and discuss conclusions for each object. In Chapter 5, we describe our spectroscopic observations (Section 5.1) and data reduction (Section 5.2) for 10 spatially double candidates observed using seeing-limited long-slit spectroscopy from Lick Observatory's Shane 3-m Telescope Kast Double Spectrograph. In Section 5.3, we match resolved spatial components seen in our imaging to the double-peaked emission lines observed with Kast, and discuss what type

of physical mechanisms are generating these emission lines. Chapter 6 summarizes our conclusions for these observations and analysis.

3.1 Shared Analysis Techniques

Spatially resolved spectroscopy will help us answer two questions: (1) Do the spatial separations and redshifts measured by OSIRIS and Kast of the resolved spatial structures seen by NIRC2 match the redshifts of the double peaks of the SDSS [O III] λ5008Å emission lines? and (2) Using the presence or absence of broad lines and emission line diagnostics, what types of objects are the main galaxy and the companion object: Type 1 AGN, Type 2 AGN, a star-forming galaxy, an outflow, or a quiescent foreground/background object? We approach answering these questions for each object with the following procedure and discuss the conclusions for each.

1. *Velocities and Redshifts: Matching Spatial Structures to Spectral Double Peaks* – By fitting Gaussians to the spectra as described in Sections 4.2 and 5.2, we measured central wavelengths for the available emission features (e.g. Hβ, [O III] λ5008Å, [Fe II] λ1.2570μm, Paβ, Paα). All of the velocity offsets are calculated with respect to the reported SDSS redshift for each object. Table 4.2 shows the velocity offsets and calculated redshifts for the lines fit to each OSIRIS spatial component, as well as the velocities and redshifts calculated for the SDSS emission lines. Table 5.2 shows the velocity offsets and spatial separations of the Kast long-slit lines, as well as the velocities calculated for the SDSS emission lines. As shown in Tables 4.2 and 5.2, the main galaxies' redshift matches an SDSS

[O III] component redshift in all of our 13 objects. However, understanding the origin of the second SDSS [O III] component is complicated, and is discussed below for the specific objects.

2. *Fluxes: Comparing Spatially Resolved Spectral Peaks to SDSS Spectral Peaks* – For our OSIRIS data, we have the opportunity to compare the relative strengths of near-infrared emission lines to comparable lines in the optical. Interestingly, the relative fluxes of the red peak to the blue peak are not the same for visible emission lines as for near-IR emission lines (Table 4.2), as observed in McGurk et al. (2011). We suggest that differences between the near-IR and visible flux ratios are due to dust obscuring one of the two components, leading to lower visible flux ratios and higher near-IR flux ratios. We also compared the [O III] λ5008Å flux ratios measured from our extracted Kast spectra and the SDSS spectra. Unexpectedly, the Kast flux ratios differ from than the SDSS flux ratios by more than 1-sigma for 5 of 9 objects and by more than 3-sigma for 4 of 9 objects. The discrepancy between the flux ratios is independent of the separation between the emission peaks, with 3-sigma differing flux ratios in 1 of 3 objects with unseparated peaks, 2 of 4 objects with intermediate peak separations, and 1 of 2 objects with peak separations matching the observed galaxies. We suggest that these disagreements result from the fact that the two sets of spectra are extracted from differing spatial regions: our 1-2″ long-slit is oriented to fully cover both the main and companion objects, while the SDSS fibers cover a 1.″5 radius circle centered on the main galaxy. Line variability is another possibility for the differences between our observations

and those of the SDSS, according to long term monitoring of one broad-line radio galaxy (Clavel & Wamsteker, 1987; Zheng et al., 1995).

3. *Identity of the Two Objects* – The presence of double peaks in spectral lines or of spatially-separated companion galaxies could be explained by a range of phenomena: dual AGN, chance superposition of two objects, a recoiling SMBH, jets, outflows from a single AGN, gravitationally lensed sources, starbursts, narrow line gas kinematics, or rings of star formation. Spatially resolved spectroscopy helps rule out many of these options, and conclusions must be made for each object. To distinguish between Type 2 AGNs and star-forming galaxies, measurements of [N II] λ6584Å/Hα and [O III] λ5008Å/Hβ place the object on the Baldwin-Philips-Terlevich (BPT) diagram (Baldwin et al., 1981; Kauffmann et al., 2003, and references therein); since our objects often have complicated and noisy overlapping structures of the broad Hα and double-peaked narrow Hα and two [N II] lines, or we lack spectral coverage of those lines, the measurement of [O III]/Hβ alone is used in this paper to differentiate between a star-forming companion and a Type 2 AGN. For three of our four candidates observed with OSIRIS, we also use near-IR emission line ratios to distinguish between emission originating from AGN or star formation. Similar in concept to the optical BPT diagram, Larkin et al. (1998) and Rodríguez-Ardila et al. (2008) plot the emission line flux ratios [Fe II] λ1.2570μm/Paβ vs. H_2 λ2.121μm/Brγ as a near-infrared AGN/star-formation emission line diagnostic diagram. We discuss the evidence for each target and conclude whether each candidate is likely a dual AGN or some other phenomena.

Overall, we find two dual AGNs (J0952+2552, J1146+5110), two pairs of an AGN and a star-forming galaxy, one galaxy with an outflow, three objects with no resolved spatial separation between their emission peaks, and five objects with spatial separations between their emission peaks that do not match the near-infrared separations measured. For these last two object categories, the emission peaks could be due to outflows or jets that are misaligned to the long-slit, complicated narrow line regions, or a second black hole retaining only its narrow line region and accretion disk. Further data are required to distinguish between these cases.

Chapter 4

Keck Near-Infrared Integral Field Spectroscopy

4.1 Observation Details

We used the OH Suppressing InfraRed Spectrograph (OSIRIS) (Larkin et al., 2006) and the Laser Guide Star Adaptive Optics system on the Keck II telescope to obtain spatially resolved spectroscopy for SDSS J091646.03+283526.7, SDSS J095207.62+255257.2, SDSS J110851.04+065901.4, and SDSS J115714.97+081632.0 (respectively shortened to J0916+2835, J0952+2552, J1108+0659, and J1157+0816 for the remainder of the paper). These four candidates were selected to have optimal guide stars, more equal ratios of the main galaxy flux to the companion galaxy flux (more equal merger ratios), and redshifts that placed the desired emission lines within one filter's bandpass.

OSIRIS observation details are summarized in Table 4.1. The 0.″100/spatial

pixel (spaxel) plate scale was used to maximize sensitivity. Observing with this plate scale in the J (1.180-1.416μm), H (1.473-1.803μm) and K (1.965-2.381μm) broad-band filters results in a spectral resolution of $\sim$3000 and a field of view of $1\farcs6 \times 6\farcs4$. We observed J0916+2835 on 2011 December 29 for a total of 40 minutes in K-band, J0952+2552 on 2010 December 30 for a total of 100 minutes in J-band and 80 minutes in H-band, J1108+0659 on 2011 December 27 and 28 for a total of 80 minutes in H-band, and J1157+0816 on 2011 December 29 for a total of 50 minutes in H-band. For each target we also imaged the tip-tilt star for PSF calibration and an A5V star at a matching airmass as a telluric standard. For J0916+2835, J0952+2552, J1108+0659, and J1157+0816 respectively, our tip-tilt stars had R magnitudes of 13.2, 14.6, 15.8, and 17.7 and separations from the target of $36\farcs9$, $40\farcs9$, $41\farcs0$, and $57\farcs1$. The estimated 550 nm seeing from the Mauna Kea MASS-DIMM for the four nights, listed in order, was $0\farcs8$, $0\farcs3$, $0\farcs8$, and $0\farcs3$.

Accurate sky subtraction is very important due to the abundance and the variation of sky lines in the near-IR. Since the detector's field of view is $6\farcs4$ long and the spatial extent of each galaxy pair is $3\farcs0$ or less, we positioned the galaxy pair on one half of the detector and empty sky on the other half, and then nodded the telescope so that in the next exposure the sky and object positions on the detector were flipped. This pattern allows us to capture and remove the longer timescale variations of the sky lines from our data.

Table 4.1: OSIRIS Spectroscopic Observation Details

SDSS Parameters:		[O III]	NIRC2			Exp.		UT
		ΔV	Separation			Time	Angle	date
ID	z	(km s^{-1})	($''$)	(kpc)	Filter	(hrs)	(deg)	(yymmdd)
J091646.03+283526.7	0.142	425	1.23	3.1	Kcb	0.67	358	111229
J095207.62+255257.2	0.339	422	1.00	4.8	Jbb	1.67	6	101230
					Hbb	1.33	6	101230
J110851.04+065901.4	0.182	209	0.73	2.2	Hbb	0.67	132	111227
						0.67	132	111228
J115714.97+081632.0	0.201	420	2.61	8.6	Hbb	0.83	27	111229

4.2 OSIRIS Data Reduction and Fitting

We used a modified[5] version of the OSIRIS Data Reduction Pipeline (ODRP) v2.3[6] to process our images. Instead of using the standard mosaicking tools provided in the ODRP, we determined relative offsets between the images by fitting two-dimensional Lorentzian profiles to the main galaxy in each frame, and then input the relative offsets directly into the mosaicking module of the ODRP[7]. Finally, we extracted and combined spectra from the ten spatial pixels with the highest signal-to-noise ratio (S/N) of the main galaxy, the companion galaxy, and any interesting local features, as shown in Figures 4.1, 4.2–4.3, 4.6, and 4.7 for J0916+2835, J0952+2552, J1108+0659, and J1157+0816, respectively. These figures also include a NIRC2 image and an OSIRIS image, created by summing up the flux over all of the wavelengths.

After extracting the final spectra, we use the IDL non-linear least squares curve fitting routine *MPFIT* (Markwardt, 2009)[8] to fit Gaussians to the detected emission

[5]Correcting for a ~ 6Å shift of the previous wavelength calibration, now incorporated into v3 of the ODRP (Wright, 2011).

[6]http://irlab.astro.ucla.edu/osiris/pipeline.html

[7]See http://irlab.astro.ucla.edu/osiriswiki/dokuphp?id=mosaic_with_a_list_of_offsets for a detailed explanation.

[8]http://purl.com/net/mpfit

lines. *MPFIT* independently fits a linear continuum and one or two Gaussians to the present lines using an input noise estimate. We calculate relative estimates of the noise using the square root of the raw frames so that portions of the spectrum with sky lines will have higher noise levels. Errors on the fitted parameters of the one or two Gaussian peaks are modeled with Monte Carlo simulations of Gaussian peaks with superimposed random errors. We measure the standard deviation (noise) of our extracted spectra with the fitted two Gaussian peaks removed, combine the two Gaussians with 300 iterations of randomly generated noise whose standard deviation matches the data to create 300 artificial spectra, and then fit each iteration of the artificial spectra with two Gaussians. The errors for each fitting parameter are the standard deviation of the 300 measurements of each fitting parameter. We include the best-fit parameters as red lines plotted over the extracted spectra in Figures 4.1-4.7, and list the fitted wavelength centers as offset velocities and redshifts in Table 4.2. In summary, J0916+2835 has detectable Brϵ, H_2 1-0 S(5) λ1.835μm, Paα, Brδ, H_2 1-0 S(3) λ1.958μm, and [Si VI] λ1.964μm. Both galaxies in J0952+2552 have detectable [S III] λ9073Å, [S III] λ9534Å, [Fe II] λ1.2570μm, and Paβ; the main galaxy of J0952+2552 also has detectable [Fe II] λ9188Å and O I. Both galaxies of J1108+0659 have detectable [Fe II] λ1.2570μm and Paβ. The main galaxy of J1157+0816 has [Fe II] λ1.2570μm and Paβ.

4.3 Discussion of Individual Objects

As mentioned in the Spectroscopic Confirmation Introduction, we use spatially resolved spectroscopy to answer two questions: (1) Do the spatial separations

and redshifts measured by OSIRIS of the resolved spatial structures seen by NIRC2 match the redshifts of the double peaks of the SDSS [O III] λ5008Å emission lines? and (2) Using the presence or absence of broad lines and emission line diagnostics, what types of objects are the main galaxy and the companion object: Type 1 AGN, Type 2 AGN, a star-forming galaxy, an outflow, or a quiescent foreground/background object? We approach answering these questions for each object with the following procedure (explained more elaborately in Section 3.1):

1. Matching the velocities and redshifts of the spatial structures to spectral double peaks

2. Comparing the fluxes of the spatially resolved spectral peaks to the fluxes of the SDSS spectral peaks

3. Identify the spatial structures using emission line diagnostic diagrams and the presence/absence of broad emission lines

We will discuss the conclusions for each object.

4.3.1 Keck OSIRIS Observations of J0916+2835

Our NIRC2 imaging of J0916+2835 (top left panel of Figure 4.1) reveals two distinct spatial structures separated by 1.″23 (3.1 kpc). As shown in Figure 4.1, J0916+2835 has Brϵ, H_2 λ1.835μm, Paα, Brδ, H_2 λ1.958μm, and [Si VI] λ1.964μm in the main galaxy at a redshift of 0.142; the detection of strong [Si VI] confirms the presence of an AGN. The companion object has continuum emission and no significant emission lines (barring a cosmic ray hit at 2.195 μm), making it either a quiescent galaxy

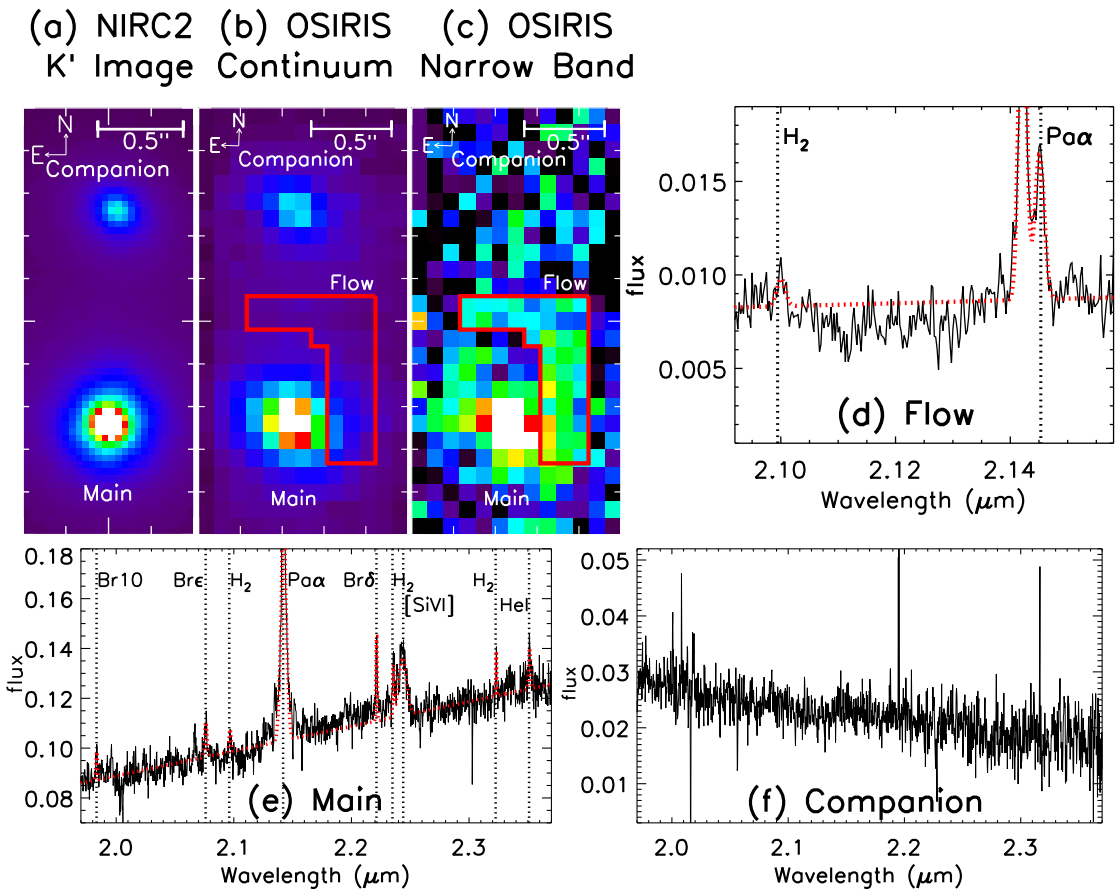

Figure 4.1: Keck LGS AO imaging and spectroscopy of J0916+2835, a Type 1 AGN with double-peaked narrow lines at z=0.142. **(a)** NIRC2 wide camera (0.″04 pixel^{-1}) *K'*-band ($\lambda_{\rm cen}$ = 2.124μm) linearly-scaled image. **(b)** OSIRIS 100 milli-arcsec (mas) platescale *Kcb*-band ($\lambda_{\rm cen}$ = 2.173μm) linearly-scaled continuum image. **(c)** OSIRIS 100 mas logarithmically-scaled image of the continuum-subtracted Paα flux from 288–603 km s^{-1} around the AGN's systemic velocity (2.14400–2.14625μm), revealing a continuum-less arc-shaped emitting region 1.0-1.9″ North-West of the AGN (outlined in red). This ionized gas emission without matching stellar continuum is well explained by an ionized outflow or inflow (labeled "flow"). Images **(a)**, **(b)**, and **(c)** show the main galaxy, companion, and flow with scale bars of 0.″5 (1.25 kpc). Ticks are spaced 0.″25 apart. **(d)** OSIRIS spectra of the flow region with a H_2 and Paα peak at +450 km s^{-1}, consistent with the SDSS [O III] λ5008Å velocity difference of 425 km s^{-1}. **(e)** OSIRIS spectra of the main galaxy. A broad Paα line and multiple narrow lines, including [Si VI], are observed in the main galaxy's AGN at the SDSS redshift of 0.142. **(f)** OSIRIS spectra of the companion. The companion galaxy contains continuum emission and no significant emission lines, revealing that it is either a quiescent galaxy or a foreground or background object.

or a foreground or background object. Finally, we detect a second set of Paα and H_2 λ1.835μm emission peaks at +450 km s^{-1} from a continuum-free arc-shaped region 1.0 kpc West, 1.9 kpc North-West, and 1.6 kpc North of the AGN. The measured velocity difference between this arc and the main galaxy is consistent with the 408 km s^{-1} velocity difference of the SDSS [O III] λ5008Å line. No NIRC2 spatial component, and thus no stellar continuum, is observed in this location. This extended ionized gas emission without a continuum counterpart can be well explained as an ionized outflow. Although the ionized emission could be due to a black hole retaining only its narrow line region and accretion disk, this would not explain the extended morphology of the emission.

The near-IR narrow H_2 λ1.835μm and Paα of J0916+2835 are, respectively, 58 and 7 times brighter in the main galaxy than the outflow. In the visible SDSS Hβ and [O III] λ5008Å lines for J0916+2835, the main galaxy's blue peak is, respectively, 6.2 and 2.4 times brighter than the outflow's red peak. Since we have determined that the outflow is the cause of the red emission peak, we can use the [O III] λ5008Å/Hβ flux ratio on the Baldwin-Phillips-Terlevich (BPT) diagram to determine the ionization source of the flow. The $\log_{10}$([O III]/Hβ) ratio of 1.09 for the flow indicates that the flow may be driven by the AGN, since there are extremely few star-forming galaxies with [O III]/Hβ ratios that high.

4.3.2 Keck OSIRIS Observations of J0952+2552

Our NIRC2 image of J0952+2552 (left panel of Figure 4.2) reveals two distinct spatial structures separated by 1.″00 (4.8 kpc). Figure 4.3 shows that the main galaxy of

J0952+2552 has [S III] λ9073Å, [Fe II] λ9188Å, [S III] λ9534Å, O I, [Fe II] λ1.2570μm, and Paβ at a redshift of 0.33810, and that the companion galaxy has [S III] λ9073Å, [S III] λ9534Å, [Fe II] λ1.2570μm, and Paβ at a redshift of 0.33974. Table 4.2 shows the velocities and redshifts calculated from the fits to these emission lines, as well as those calculated from the SDSS double [O III] components.

The main galaxy's redshift (0.33810 ± 0.00007) matches the SDSS [O III] blue component redshift (0.33798 ± 0.00004), while the companion's redshift (0.33974 ± 0.00007) matches the SDSS [O III] red component redshift (0.33986 ± 0.00004). This clearly illustrates that the double spatial structure corresponds to the double-peaked emission lines.

However, the relative fluxes of the lines in the visible and in the near-IR are not the same (Table 4.2). For our near-IR narrow [S III] λ9073Å, [S III] λ9534Å, [Fe II] λ1.2570μm, and Paβ lines, the main galaxy is 5.3, 5.7, 2.8, and 2.3 times brighter than the companion, respectively. In the visible SDSS [O III] λ5008Å line, the main galaxy's blue peak is 1.5 times stronger than the companion's red peak. In the right panel of Figure 4.2, we show the SDSS spectrum of the [O III] λ4959Å and [O III] λ5008Å lines; the overplotted fits show that although the [O III] λ5008Å red peak is taller, the [O III] λ5008Å blue peak is wider and thus contains more flux. Since we matched the IR-bright main galaxy to the [O III] blue peak and the IR-faint companion to the [O III] red peak, there is clearly more going on with this system to create such varied flux ratios. We suggest that the difference in visible and near-IR flux ratios might be due to dust obscuring the main galaxy and not the companion, which would lead to

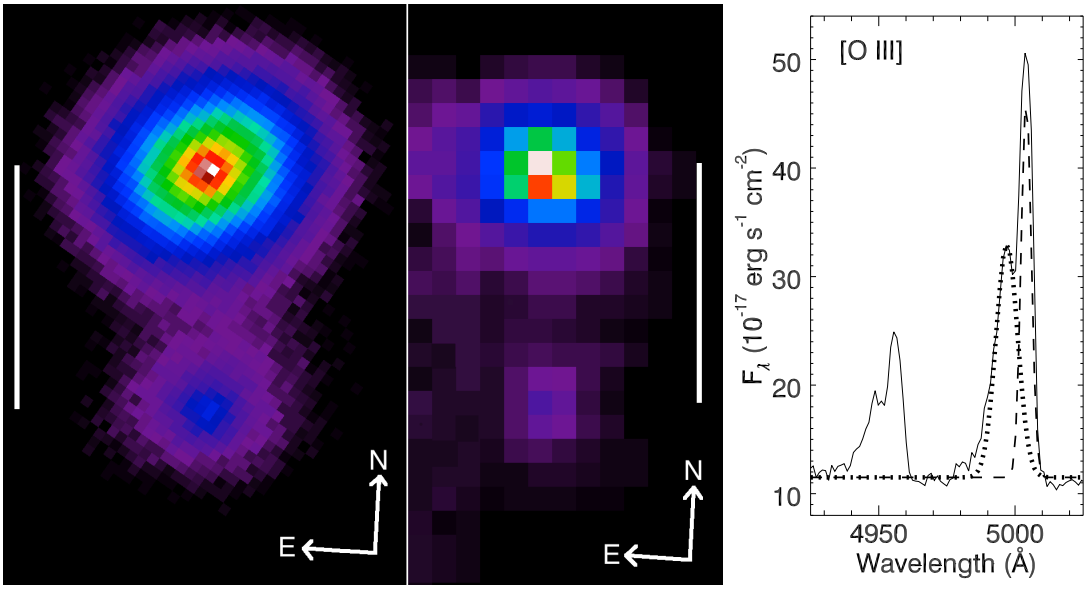

Figure 4.2: (**left** and **middle**) Keck LGS AO imaging of J0952+2552, a Type 1 AGN with double-peaked narrow lines. The white line in both images corresponds to 1.″00 or 4.80 kpc at the redshift of the system. (left) NIRC2 wide camera (0.″04 pixel^{-1}) H-band ($\lambda_{cen} = 1.633\mu$m) log-scaled image. **middle** OSIRIS H-band ($\lambda_{cen} = 1.638\mu$m) log-scaled image, created by summing up the flux over all the wavelengths in each of the spatial pixels. Each OSIRIS spatial pixel has a width of 0.″1 or 0.48 kpc at the redshift of the system. The bright main galaxy and its companion are clearly visible. (**right**) SDSS [O III] λ4959Å and [O III] λ5008Å spectrum of J0952+2552 in rest vacuum wavelengths. The dotted and dashed lines are, respectively, the fits to the blue and red components of the narrow [O III] λ5008Å line.

lower visible flux ratios and higher near-IR flux ratios in the main galaxy.

Identity of the Two Objects

As mentioned in the Introduction, the presence of double peaks in spectral lines or of spatially-separated companion galaxies could be explained by a range of phenomena: chance superposition of two objects, a recoiling SMBH, jets, outflows from a single AGN, gravitationally lensed sources, starbursts, or rings of star formation. Matching the individual components of the double-peaked emission lines to the two

distinct galaxies shows that the double components do not come from rings of star formation and are not a chance superposition of two objects. Since J0952+2552 is radio-quiet, these features are unlikely due to jets interacting with the surrounding medium. Since the two galaxies have different spectra, the two galaxies are not two images of one gravitationally lensed object (Hennawi et al., 2006, and references therein).

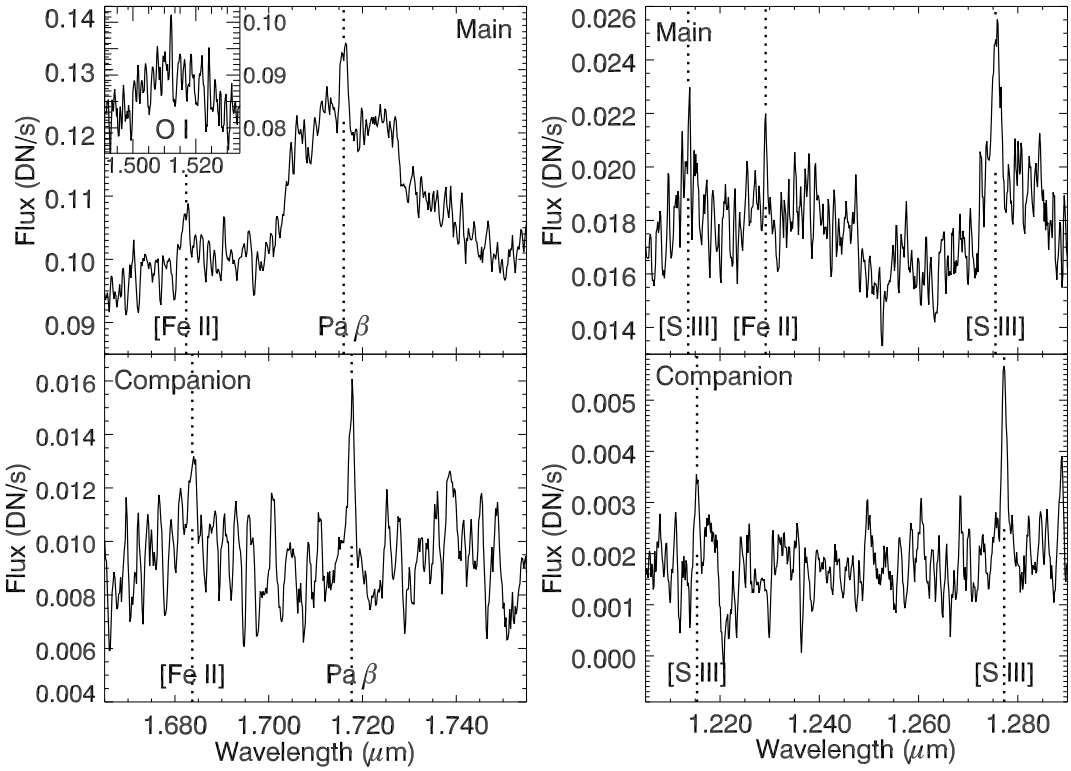

Figure 4.3: H- and J-band (left and right, respectively) spectra of the main galaxy (top) and the companion (bottom). The dotted lines mark the measured centers of the identified narrow lines. The observed wavelengths are in units of vacuum μm. We observe narrow emission lines ([S III] λ9073Å, [Fe II] λ9188Å, [S III] λ9534Å, O I, [Fe II] λ1.2570μm, Paβ) as well as broad Paβ and broad O I from the main galaxy, making it a Type 1 AGN. The broad Paβ has a measured FWHM of 6300 ± 200 km s^{-1}, and the broad O I has a measured FWHM of 5000 ± 500 km s^{-1}. Only narrow emission lines ([S III] λ9073Å, [S III] λ9534Å, [Fe II] λ1.2570μm, Paβ) are evident in the companion, consistent with a Type 2 AGN.

We modeled the NIRC2 H-band image of J0952+2552 using the galaxy struc-

ture fitting code GALFIT v3.0 (Peng et al., 2002). We modeled both the main and the companion galaxies as a combination of a point source for the AGN, and an extended stellar light distribution for the galaxy with a variable Sérsic index, half-light radius, ellipticity, and orientation. The fit was visually examined, and the initial parameters were varied until a good fit was achieved. Both galaxies are disk-like, with Sérsic indices of 1.5 ± 1 (an elliptical has a Sérsic index of 4). Since the companion is a not a lone point source, it is not likely to be a recoiling SMBH. Similarly, since the companion has both a disky host galaxy and a central point source, the companion's emission lines are unlikely to be due to a jet or outflow from the main AGN interacting with the companion galaxy. As we observe no bridge of ionized gas linking the two galaxies, it is likely that no gas has been transferred between the galaxies. Additionally, since both galaxies have disk morphologies and lack a connecting bridge of ionized gas linking the two galaxies, this suggests that both galaxies brought gas to the encounter.

To distinguish between starbursts and AGNs of Types 1 and 2, we examine the observable broad lines and use several emission line ratio diagnostics. In Figure 4.3, the spectrum for the main galaxy (top panels) clearly shows both a broad line for Paβ (left) and narrow emission lines (right). The FWHM of this broad Paβ is 6300 ± 200 km s^{-1}, which roughly agrees with the 5960 ± 90 km s^{-1} FWHM measured for the broad Hβ line in the SDSS spectrum. We also see the broad O I $\lambda 1.12900 \mu m$ fluorescent line in our main galaxy's H-band spectrum. The observed broad O I, with its FWHM of 5000 ± 500 km s^{-1}, is observed in 67% of Type 1 AGNs (Riffel et al., 2006). We measure the central wavelength of broad O I to be $1.5116 \pm 2 \mu m$, corresponding to a redshift of

0.3389 ± 0.0018; this redshift falls between with the average redshifts of the main galaxy and of the companion. The presence of both broad and narrow lines indicates that the main galaxy is a Type 1 AGN.

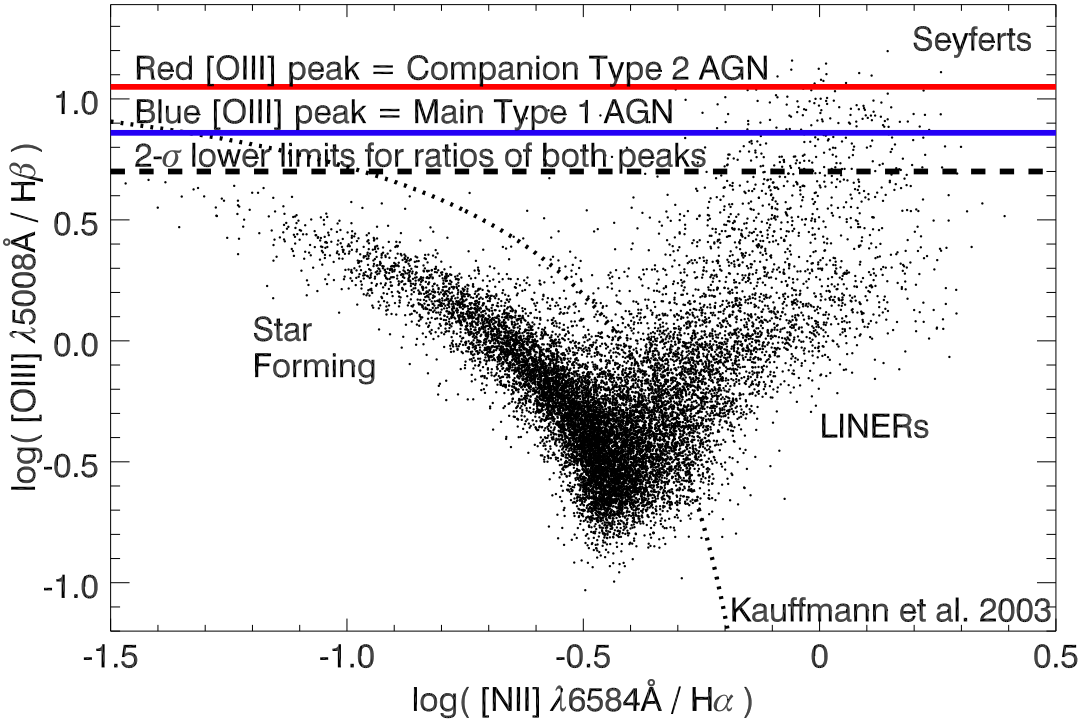

Figure 4.4: Baldwin–Philips–Terlevich diagram in which we plot the emission line flux ratios [O III] λ5008Å/Hβ vs. the ratios [N II] λ6584Å/Hα for a sample of 14,708 low redshift (z<0.3) SDSS galaxies in which all four lines are detected with S/N > 3. The dotted curve shows the dividing line between starburst galaxies and AGNs as defined by Kauffmann et al. (2003). The companion red-component line ratios are plotted by the asterisk symbol, with 1σ error bars in the [N II]/Hα direction. Since we are unable to disentangle an accurate and unique measurement of the SDSS [N II] and Hα double-peaked lines (on top of the broad Type 1 Hα peak), we plot our [O III]/Hβ flux ratios as lines across the diagram. The blue line is the main AGN's blue peak ratio, and the red line is the companion AGN's red peak ratio. The dashed line is the 2σ lower [O III]/Hβ limit of both the red and blue component ratios. Both [O III] components fall above the location of star forming galaxies, meaning that both [O III] components, and thus both the main galaxy and the companion, are due to AGNs.

The companion shows only narrow lines, so it is not a Type 1 AGN. The traditional way to distinguish between Type 2 AGNs and star-forming galaxies is to use

measurements of [N II] λ6584Å/Hα and [O III] λ5008Å/Hβ to place the object on the Baldwin-Philips-Terlevich (BPT) diagram (Baldwin et al., 1981; Kauffmann et al., 2003, and references therein). Since the red component of the SDSS lines has a larger peak height, we were able to measure both [N II]/Hα and [O III]/Hβ for the companion. Unfortunately, due to the complicated and noisy overlapping structure of the broad Hα and double-peaked narrow Hα and two [N II] lines, we are unable disentangle an accurate and unique measurement of [N II]/Hα for the main galaxy. However, the measurement of [O III]/Hβ can still be used to differentiate between a starburst companion and a Type 2 AGN. As shown in Figure 4.4, both objects fall in the exclusively Seyfert/AGN region of the plot. For the main galaxy, we can combine the presence of broad lines in its spectrum with the fact that few star-forming galaxies exist at such high [O III]/Hβ ratios to conclude that it is a Type 1 AGN. The line ratios of the companion place it clearly among the AGNs, allowing us to conclude that the companion is a Type 2 AGN.

Using the OSIRIS spectra, we also use near-IR emission line ratios to distinguish between emission originating from AGN or star formation. Similar in concept to the optical BPT diagram, Larkin et al. (1998) and Rodríguez-Ardila et al. (2008) plot the emission line flux ratios [Fe II] λ1.2570μm/Paβ vs. H_2 λ2.121μm/Brγ as a near-infrared AGN/star-formation emission line diagnostic diagram. Dotted lines show the star-forming, AGN, and LINER/inconclusive regions of the diagram; generally, starbursts have $\log([\text{Fe II}]/\text{Pa}\beta) < -0.22$, AGNs have $-0.22 < \log([\text{Fe II}]/\text{Pa}\beta) < 0.30$, and LINERs have $\log([\text{Fe II}]/\text{Pa}\beta) > 0.30$ (Rodríguez-Ardila et al., 2008). Figure 4.5 shows this diagram for J0952+2552, with the [Fe II]/Paβ line ratios of the main and compan-

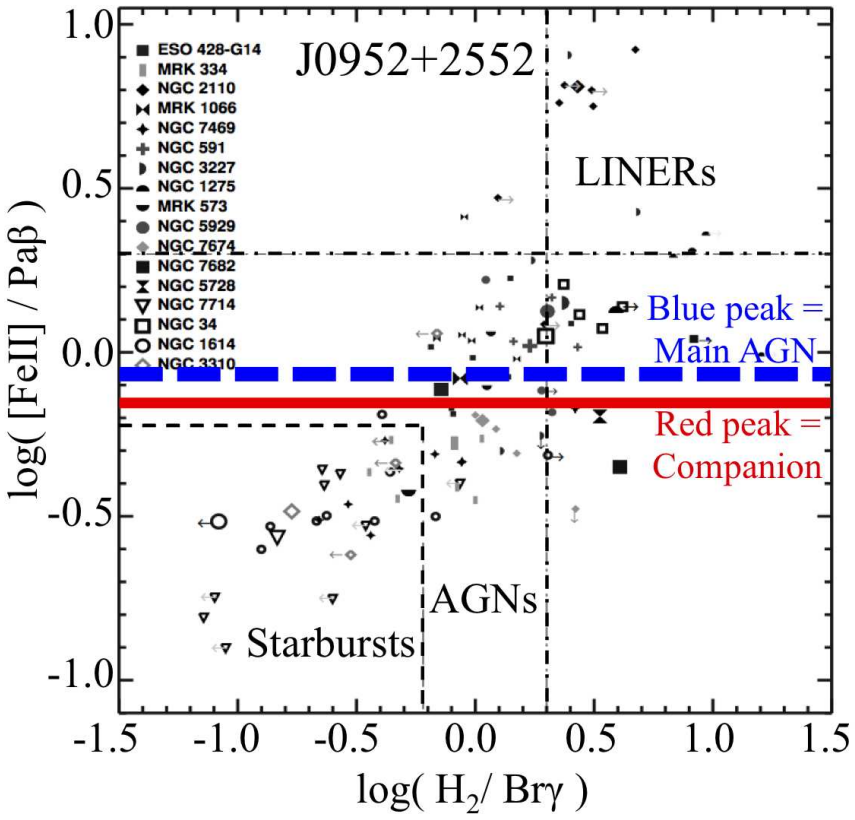

Figure 4.5: Near-infrared AGN/star-formation emission line diagnostic diagrams, similar to the optical Baldwin-Phillips-Terlevich diagram (Larkin et al., 1998). Rodríguez-Ardila et al. (2008) plot the emission line flux ratios [Fe II] λ1.2570μm/Paβ vs. H_2 λ2.121μm/Brγ of star-forming galaxies and Type 1 and 2 Seyfert AGNs as various symbols; dotted lines mark the star-forming, AGN, and inconclusive/LINER regions of the diagram. We have plotted the [Fe II] λ1.2570μm/Paβ line ratios of the J0952+2552 main AGN (blue peak) and companion galaxy (red peak) as, respectively, dashed blue and solid red lines (since we do not have observations of the H_2 λ2.121μm and Brγ lines). The ratios of both galaxies are consistent with being due to an AGN, similar to the optical BPT diagram in Figure 4.4.

ion galaxies shown as, respectively, dashed blue and solid red lines (since we do not have observations of the H_2 λ2.121μm and Brγ lines). The main galaxy and the companion have log([Fe II]/Paβ) ratios, respectively, of -0.07 and -0.16; they fall directly in the AGN region of the diagram, providing further support that both the main galaxy and the companion are AGNs.

Another, weaker, indication that both galaxies are AGNs is that the spectra of both show narrow [S III] λ9073Å and [S III] λ9534Å lines. According to the AGN spectral atlas compiled by Riffel et al. (2006), all AGNs show [S III]. However, because the [S III] lines are also frequently seen in starburst galaxies, the presence of these lines does not clearly distinguish between AGNs and starbursts.

We conclude that J0952+2552 is a dual AGN using both optical and near-IR emission line ratio diagnostics.

4.3.3 Keck OSIRIS Observations of J1108+0659

The NIRC2 imaging of J1108+0659 (top left and center panels of Figure 4.6) shows two spatial structures separated by 0.″73 (2.2 kpc) connected by a bridge of continuum light. The main object has visible substructure in our NIRC2 imaging (0.″04 pixel^{-1}) that is not resolved in our OSIRIS observations using a plate scale of 0.″100 pixel^{-1} (right panel of Figure 4.6). J1108+0659 has [Fe II] λ1.2570μm and Paβ peaks in both the main and companion galaxies. While emission lines are detected in both galaxies, there is insufficient signal-to-noise to determine accurate line centers and velocity differences, especially of the double peaks suggested in the main object's spectrum.

We can, however, use the near-IR line fluxes to place constraints on the origins of the two spatial structures. As described in Section 4.3.2, Larkin et al. (1998) and Rodríguez-Ardila et al. (2008) plot the emission line flux ratios [Fe II] λ1.2570μm/Paβ vs. H_2 λ2.121μm/Brγ as a near-infrared AGN/star-formation emission line diagnostic diagram. The first panel of Figure 4.8 shows this diagram for J1108+0659, with the [Fe II]/ Paβ line ratios of the main and companion galaxies as,

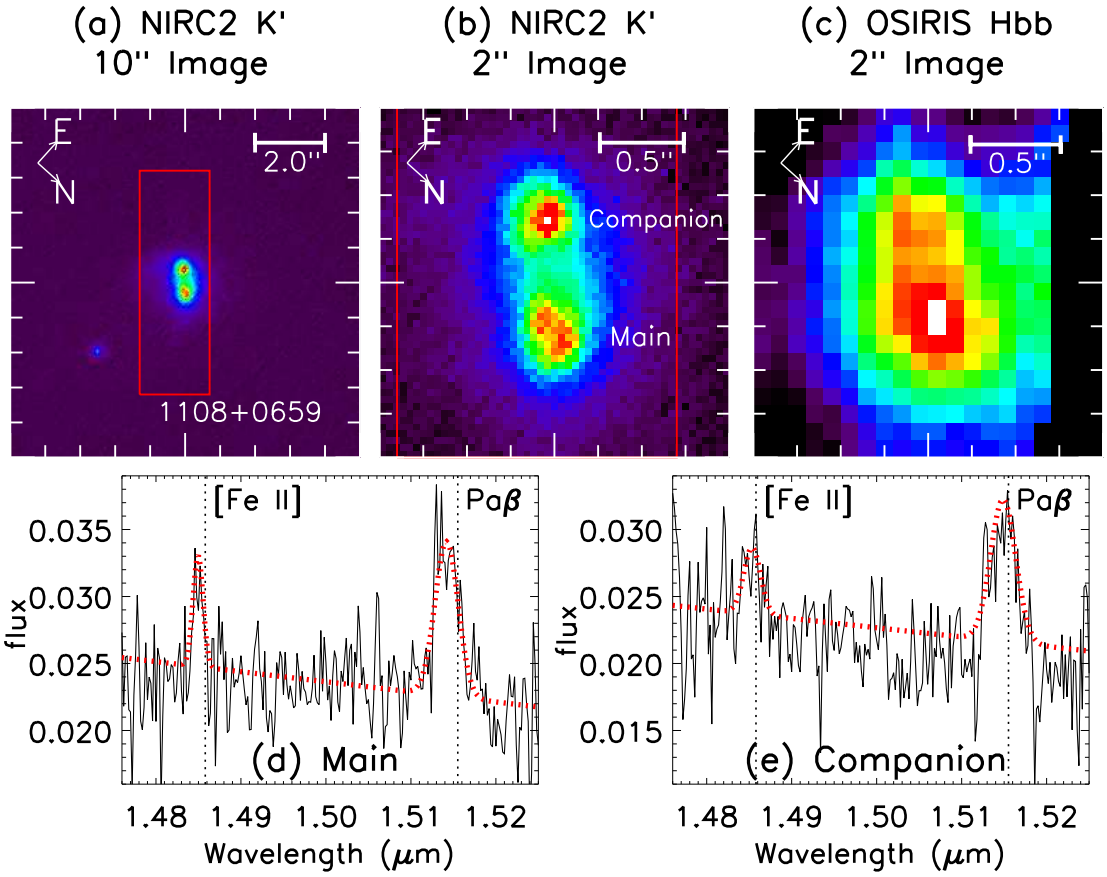

Figure 4.6: Keck LGS AO imaging and spectroscopy of J1108+0659, a Type 1 AGN with double-peaked narrow lines at z=0.182. **(a)** and **(b)** show NIRC2 wide camera (0.″04 pixel^{-1}) *K'*-band ($\lambda_{\rm cen} = 2.124\mu$m) linear-scale images. **(a)** spans $10'' \times 10''$ with a $2''$ scale bar, while **(b)** spans $2'' \times 2''$ with a 0.″5 scale bar. The OSIRIS field of view is outlined in red. **(c)** shows the OSIRIS 100 milli-arcsec platescale *Hbb*-band ($\lambda_{\rm cen} = 1.638\mu$m) linearly-scaled continuum image. The NIRC2 images have been rotated to match the orientation of the OSIRIS images, with North and East rotated as indicated by the compass rose. The extracted OSIRIS spectra from the main galaxy **(d)** and companion galaxy **(e)** both have [Fe II] $\lambda 1.2570\mu$m and Paβ emission lines that, when fitted (red dotted lines), have a velocity difference of 100 km s^{-1}, which does not match the measured 206 km s^{-1} velocity difference of the double [O III] peaks in the SDSS spectrum. The near-IR diagnostic diagram in Figure 4.8 reveal that the [Fe II]/Paβ ratios of both galaxies fall in a region more dominated by star formation than by AGN activity. While the original SDSS spectrum informs us that there is at least one AGN present in the system, we cannot determine which galaxy contains the AGN and we cannot definitively confirm either galaxy as dominated by star formation or AGN activity.

respectively, solid black and dashed blue lines (since we do not have observations of the H_2 $\lambda 2.121 \mu$m and Brγ lines). The line ratios of both the main and companion galaxies fall in a region dominated primarily by star-forming galaxies and less by AGN. While the original SDSS spectrum informs us that there is at least one AGN present in the system, we cannot determine which galaxy contains the AGN and we cannot definitively confirm either galaxy as dominated by star formation or AGN activity.

Fu et al. (2012) classify this object as having an extended narrow line region. Conversely, Liu et al. (2013) observed J1108+0659 with Chandra and HST; Liu et al. derive limits on star formation from the HST U-band imaging and constrain the maximum X-ray luminosity attributable to star formation. The X-ray luminosities of both nuclei are significantly higher than the maximum star formation X-ray luminosities, indicating that both galaxies contain AGN. We likely need higher spatial resolutions and higher S/N observations to distinguish which galaxies contain an AGN and to compare our observations further with Liu et al.'s results of a dual AGN.

4.3.4 Keck OSIRIS and Shane Kast observations of J1157+0816

Our Keck NIRC2 imaging of J1157+0816 shows three objects in a line. The central object is bright, with roughly symmetric companions $2\farcs61$ and $2\farcs90$ (8.6 and 9.6 kpc at the AGN's redshift from the SDSS) to the South and North, respectively. As shown by our Keck OSIRIS data in Figure 4.7 and by our Shane Kast data in Figure 5.6, J1157+0816 has double emission peaks in the central object only; the North and South companions show only featureless continuum both in the optical and in the near-infrared, and thus cannot be distinguished between quiescent galaxies and foreground or

background superpositions. The two peaks of the near-IR narrow [Fe II] λ1.2570μm and Paβ lines of J1157+0816 have the same flux ratios, within our errors, as the two peaks of the SDSS [O III] λ5008Å and Hβ lines, respectively. The flux ratios between our Kast and SDSS [O III] emission peaks are consistent with each other within 1-sigma.

From spatially resampling our Keck OSIRIS data and spatially analyzing our Shane Kast observations of this object, we find the two emission peaks to be spatially coincident down to 0.03$\pm$0.02$''$ (100$\pm$70 pc), which means that we do not detect the 0$\farcs$28 (940 pc) separation measured by Comerford et al. (2012)'s long-slit observations. This suggests that our spectrographs covered different spatial regions than Comerford et al.'s spectrograph. Spatially coincident double emission lines such as those seen in J1157+0816 can be caused unresolved observations of several small-separation scenarios: binary AGNs, small-scale outflows or jets, rings of star formation, gas disks, or complicated narrow line region kinematics. BPT diagrams can sometimes distinguish between the aforementioned cases.

The same near-IR emission line diagnostic ratio as discussed in Subsections 4.3.2 and 4.3.3 can be used for the blue and red emission line peaks detected in the main galaxy of J1157+0816. Plotted as dashed blue and solid red lines in Figure 4.8, respectively, the blue and red peak [Fe II] λ1.2570μm/Paβ line ratios fall in the AGN region of the diagnostic diagram. This indicates that the peaks could be due to complex narrow line kinematics, a very small-scale outflow, or an unresolved dual AGN. Since Hβ is too faint to detect in our Kast observations, we estimate a maximum peak flux for a faint Hβ line camouflaged by the noise, as described in Section 5.2, and then plot the

minimum [O III]/Hβ ratios in the left-middle panel of Figure 5.6. These [O III]/Hβ ratios do not allow us to differentiate between AGN activity and star-formation.

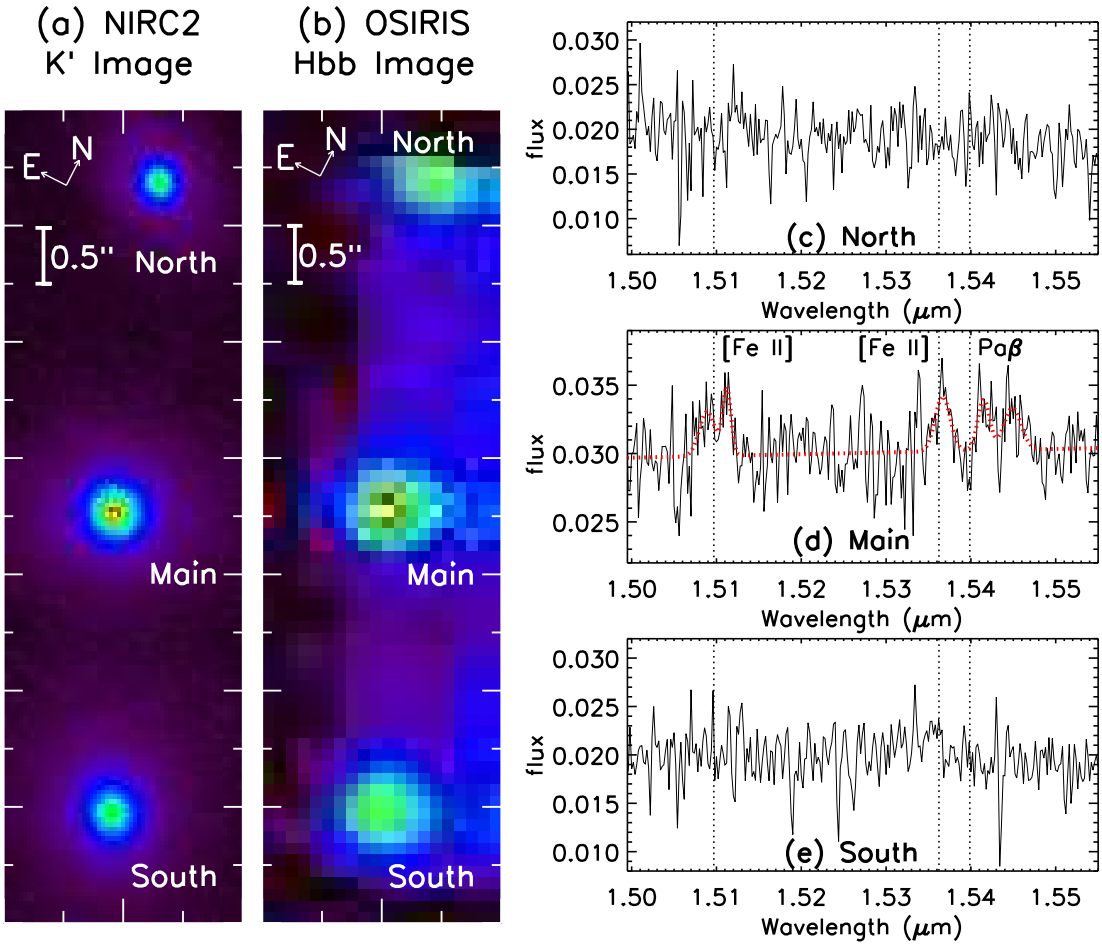

Figure 4.7: Keck LGS AO imaging and spectroscopy of J1157+0816, a Type 2 AGN with double-peaked narrow lines at z=0.201. **(a)** NIRC2 wide camera ($0\farcs04$ pixel^{-1}) K'-band ($\lambda_{\rm cen} = 2.124\mu$m) linear-scale image spanning $2''\times7''$, with North and East rotated as indicated by the compass rose. **(b)** OSIRIS 100 milli-arcsec platescale *Hbb*-band ($\lambda_{\rm cen} = 1.638\mu$m) linearly-scaled image. The right column displays the spectra from the North **(c)**, Main **(d)**, and South **(e)** nuclei. We detect double peaked [Fe II] $\lambda1.2570\mu$m and Paβ in the Main galaxy's AGN. The North and South objects contain continuum emission and no significant emission lines. They are either quiescent galaxies or foreground or background objects.

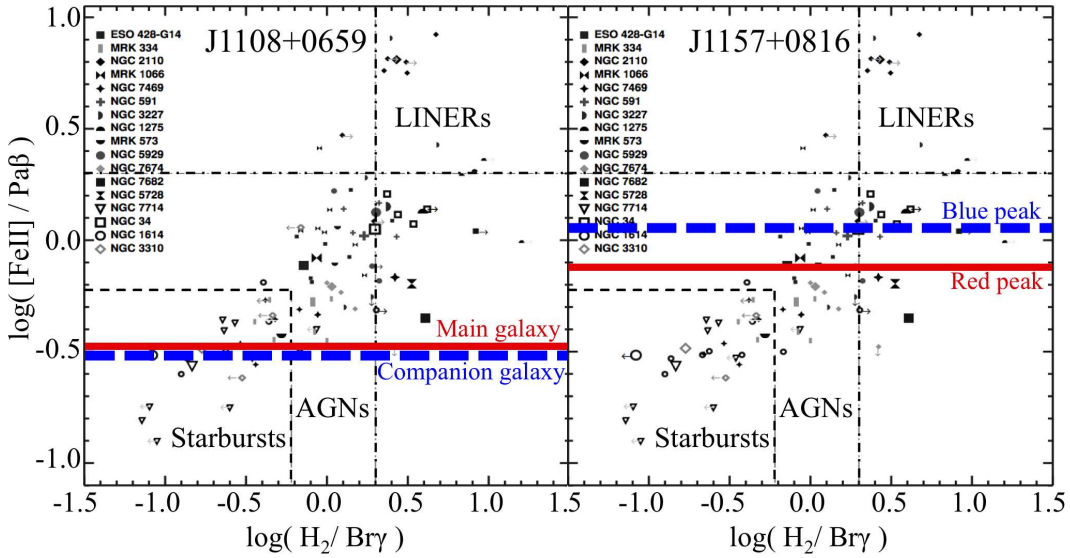

Figure 4.8: Near-infrared AGN/star-formation emission line diagnostic diagrams, similar to the optical Baldwin-Phillips-Terlevich diagram (Larkin et al., 1998). Rodríguez-Ardila et al. (2008) plot the emission line flux ratios [Fe II] $\lambda 1.2570\mu$m/Paβ vs. H_2 $\lambda 2.121\mu$m/Brγ of star-forming galaxies and Type 1 and 2 Seyfert AGNs as various symbols; dotted lines mark the star-forming, AGN, and inconclusive/LINER regions of the diagram. In the *left* panel, we have plotted the [Fe II] $\lambda 1.2570\mu$m/Paβ line ratios of the J1108+0659 main AGN and companion galaxy as, respectively, solid red and dashed blue lines (since we do not have observations of the H_2 $\lambda 2.121\mu$m and Brγ lines). While the original SDSS spectrum informs us that there is at least one AGN present in the system, the line ratios of both the main and companion galaxies fall in a region dominated primarily by star-forming galaxies and less by AGN, making it difficult to definitively determine the source of the emission in either galaxy; we likely need higher spatial resolutions and higher S/N observations. In the *right* panel, the [Fe II] $\lambda 1.2570\mu$m/Paβ line ratios of the blue and red peaks in the main J1157+0816 galaxy are plotted as, respectively, dashed blue and solid red lines. The ratios of both peaks are consistent with being due to an AGN; this signature could be due to complex narrow line kinematics, a very small-scale outflow, or an unresolved dual AGN.

Table 4.2: Measured Velocities and Separations for Keck OSIRIS Data

Spectral Line	v_{12diff}[9,10]	v_1[9, 10]	v_2[9,10]	z_1	z_2	F_1/F_2[11]
J0916+0835						
Main Galaxy						
Br10 λ1.73669 μm		19^{+13}_{-12}		$0.14208^{+0.00005}_{-0.00004}$		
Brϵ λ1.81791 μm		23^{+10}_{-12}		$0.14209^{+0.00003}_{-0.00004}$		
H_2 λ1.8355025 μm		99^{+13}_{-14}		$0.14238^{+0.00004}_{-0.00005}$		
Paα λ1.87561 μm	28±4	33^{+0}_{-0}	62^{+4}_{-5}	$0.14213^{+0.00000}_{-0.00000}$	$0.14224^{+0.00002}_{-0.00002}$	0.9±0.0
Brδ λ1.94509 μm		11^{+3}_{-3}		$0.14204^{+0.00001}_{-0.00001}$		
H_2 λ1.9570 μm		114^{+6}_{-6}		$0.14243^{+0.00002}_{-0.00002}$		
[Si VI] λ1.9650 μm		-84^{+11}_{-12}		$0.14168^{+0.00004}_{-0.00004}$		
H_2 λ2.0338 μm		74^{+4}_{-5}		$0.14228^{+0.00002}_{-0.00002}$		
He I λ1.8355025 μm		55^{+8}_{-9}		$0.14221^{+0.00003}_{-0.00003}$		
Extended Flow						
H_2 λ1.8355025 μm		558^{+15}_{-19}		$0.14413^{+0.00005}_{-0.00006}$		
Paα λ1.87561 μm	413±5	28^{+1}_{-1}	441^{+5}_{-4}	$0.14211^{+0.00001}_{-0.00001}$	$0.14368^{+0.00002}_{-0.00002}$	2.0±0.1
SDSS Spectrum						
Hβ	386±8	33^{+1}_{-1}	420^{+8}_{-7}	$0.14213^{+0.00001}_{-0.00001}$	$0.14360^{+0.00003}_{-0.00003}$	6.2±1.2

Continued on next page

Table 4.2 – *Continued from previous page*

Spectral Line	v_{12diff}[9,10]	v_1[9,10]	v_2[9,10]	z_1	z_2	F_1/F_2[11]
[O III] λ4959Å	395±2	40^{+1}_{-1}	435^{+2}_{-2}	$0.14215^{+0.00001}_{-0.00001}$	$0.14366^{+0.00001}_{-0.00001}$	2.2±0.1
[O III] λ5008Å	407±4	30^{+2}_{-2}	438^{+3}_{-3}	$0.14212^{+0.00001}_{-0.00001}$	$0.14367^{+0.00001}_{-0.00001}$	2.4±0.2
J0952+2552						
Main Galaxy						
[S III] λ9073Å		-25±63		0.33797±0.0003		5.7±0.2[12]
[Fe II] λ9188Å		-27±16		0.33786±0.00007		
[S III] λ9534Å		-14±28		0.33792±0.00013		5.3±0.2[12]
[Fe II] λ1.257025 μm		98±38		0.33842±0.00017		2.8±0.3[12]
Paβ λ1.28215884 μm		93±20		0.33840±0.00009		2.3±0.1[12]
Averaged values		25±37		0.33810±0.00017		
Companion Galaxy						
[S III] λ9073Å		413±31		0.33982±0.00014		...[13]
[S III] λ9534Å		391±18		0.33972±0.00008		...[13]
[Fe II] λ1.257025 μm		399±40		0.33973±0.00021		...[13]
Paβ λ1.28215884 μm		382±24		0.33968±0.00011		...[13]
Averaged values		396±30		0.33974±0.00014		
SDSS Spectrum						

Continued on next page

Table 4.2 – *Continued from previous page*

Spectral Line	v_{12diff}[9,10]	v_1[9,10]	v_2[9,10]	z_1	z_2	F_1/F_2[11]
[O III] λ5008Å	422±12	0±9	422±9	0.33798±0.00004	0.33986±0.00004	1.5±0.1
J1108+0659						
Main Galaxy						
[Fe II] λ1.257025 μm		-170^{+12}_{-12}		$0.18133^{+0.00004}_{-0.00004}$		
Paβ λ1.28215884 μm		-259^{+15}_{-18}		$0.18098^{+0.00005}_{-0.00006}$		
Companion Galaxy						
[Fe II] λ1.257025 μm		-90^{+27}_{-24}		$0.18164^{+0.00009}_{-0.00008}$		
Paβ λ1.28215884 μm		-122^{+14}_{-13}		$0.18152^{+0.00005}_{-0.00005}$		
SDSS Spectrum						
Hβ	399±5	-393^{+4}_{-4}	6^{+3}_{-2}	$0.18045^{+0.00002}_{-0.00002}$	$0.18202^{+0.00001}_{-0.00001}$	1.3±0.1
[O III] λ4959Å	224±5	-205^{+4}_{-4}	18^{+1}_{-1}	$0.18119^{+0.00002}_{-0.00002}$	$0.18207^{+0.00001}_{-0.00001}$	0.4±0.0
[O III] λ5008Å	206±2	-192^{+2}_{-2}	13^{+0}_{-0}	$0.18124^{+0.00001}_{-0.00001}$	$0.18205^{+0.00000}_{-0.00000}$	0.4±0.0
J1157+0816						
Main Galaxy						
[Fe II] λ1.257025 μm	459±42	-153^{+36}_{-39}	305^{+18}_{-17}	$0.20038^{+0.00012}_{-0.00013}$	$0.20223^{+0.00006}_{-0.00006}$	1.3±0.5
[Fe II] λ1.27913 μm		86^{+22}_{-25}		$0.20135^{+0.00007}_{-0.00009}$		

Continued on next page

Table 4.2 – *Continued from previous page*

Spectral Line	v_{12diff} [9,10]	v_1 [9,10]	v_2 [9,10]	z_1	z_2	F_1/F_2 [11]
Paβ λ1.28215884 μm	659±43	318^{+25}_{-25}	978^{+40}_{-30}	$0.20228^{+0.00008}_{-0.00009}$	$0.20492^{+0.00014}_{-0.00010}$	0.8±0.3
SDSS Spectrum						
Hβ	387	-122	264	0.20051	0.20206	1.1±0.2
[O III] λ4959Å	384±12	-82^{+10}_{-10}	302^{+7}_{-6}	$0.20067^{+0.00004}_{-0.00004}$	$0.20221^{+0.00003}_{-0.00003}$	0.7±0.1
[O III] λ5008Å	387±6	-122^{+6}_{-4}	264^{+4}_{-4}	$0.20051^{+0.00002}_{-0.00002}$	$0.20206^{+0.00002}_{-0.00002}$	1.7±0.1

[9] Velocities in km s^{-1}, measured with respect to the redshift in the SDSS catalogue.

[10] 1σ measurement errors.

[11] Line flux ratio: main galaxy to companion galaxy.

[12] For J0952+2552 we compare the line flux ratios of the main galaxy to the companion galaxy, instead of blue peak flux to red peak flux.

[13] See flux comparison for the main galaxy.

Chapter 5

Shane Kast Optical Long-Slit Spectroscopy

5.1 Observation Details

We used the Kast Double Spectrograph on the Shane 3-m telescope at Lick Observatory to obtain optical long-slit spectroscopy for 10 targets. The Kast Double Spectrograph offers simultaneous observations in the blue and red with spatial resolutions along the slit of $0\farcs43$ and $0\farcs78$, respectively. Because we resolve the two emission peaks of each double-peaked AGN in velocity space, it is possible to measure their positional centers along the slit to much better than the seeing limit; we are instead limited by the pixel scale of the detectors.

On 2013 April 13 and 14, we observed 10 candidates; their names and observation details are listed in bottom section of Table 5.1. These 10 candidates were selected

to have separations greater than 1.″5, almost double the Kast Spectrograph's red side pixel scale of 0.″78. In summary, we observed each candidate for between 0.5 and 3 hours with the D55 dichroic to split the beam so that we could use both channels of Kast. For all blue-side observations and observations of objects with $z < 0.1$, we used the B600/4310 grism, with a dispersion of 1.02 Å pixel^{-1} and tuned to cover 3300 – 5520 Å. For the red-side observations, we used the R1200/5000 grating (dispersion 1.17 Å pixel^{-1}) or the R830/8460 grating (dispersion 1.70 Å pixel^{-1}). In order to target Hβ and both [O III] emission lines, we used the R1200/5000 grating tuned to cover 5400

Table 5.1: Kast Spectroscopic Observation Details

SDSS Parameters: ID	z	[O III] ΔV (km s^{-1})	NIRC2 Separation ($''$)	(kpc)	Kast Grating / Grism[14]	Exp. Time (hrs)	Slit Width ($''$)	Slit Angle (deg)	UT date (yymmdd)
J072554.42+374436.9*	0.634	250	2.91	19.9	R830/8460	2.0	1.0	160	130413
J080315.67+483603.0*	0.635	280	2.63	18.0	R830/8460	1.0	2.0	173	130414
J094032.25+311328.6	0.170	371	2.45	7.1	R1200/5000	1.0	1.0	107	130413
J105104.54+625159.3*	0.436	360	1.52	8.6	R830/8460	0.5	1.0	68	130413
J114642.47+511029.6	0.130	284	2.84	6.6	R1200/5000	0.5	2.0	214	130414
J115714.97+081632.0	0.201	420	2.61	8.6	R1200/5000	0.5	1.0	207	130413
J130724.08+460400.9*	0.353	580	2.37	11.6	R1200/5000^H	3.0	2.0	156	130414
J133226.34+060627.3	0.207	420	1.58	5.4	R1200/5000	0.5	2.0	192	130413
J161027.41+130806.8*	0.229	290	2.35	8.6	R1200/5000	0.5	1.0	114	130413
J165206.15+310707.6	0.075	310	2.96	4.2	B600/4310	0.5	2.0	93.8	130413

[14] To target Hβ and [O III], a grating was chosen to match the redshift of each object. The B600/4310 grism, tuned to cover 3300 – 5520 Å, covers candidates with $z < 0.1$. The R1200/5000 grating is tuned to cover 5400 – 6800 Å for candidates with $0.1 < z < 0.3$ and is tuned to a higher wavelength range to cover 5800 – 7190 Å for candidates with $0.3 < z < 0.36$ (labeled R1200/5000^H above). The R830/8460 grating is tuned to cover 6311 – 8351 Å for candidates with $z > 0.36$.

– 6800 Å for candidates with $0.1 < z < 0.3$, the R1200/5000 grating tuned to cover 5800 – 7190 Å for candidates with $0.3 < z < 0.36$, and the R830/8460 grating tuned to cover 6311 – 8351 Å for candidates with $z > 0.36$. The seeing for the night varied from $0\farcs8$ up to $1\farcs6$, so we varied our slit width from $1\farcs0$ to $2\farcs0$. The spectra were taken with the slit aligned so that it covered both the main galaxy and the companion; these position angles are known from our near-IR imaging (this work; Rosario et al., 2011; Fu et al., 2012). After each observation before moving the telescope away, we took arc lamp exposures and dome flats to calibrate the flexure of the telescope and instrument.

5.2 Kast Data Reduction and Fitting

We reduced the Kast spectra using the Low-Redux[15] pipeline developed by J. Hennawi, S. Burles, D. Schlegel, and J. X. Prochaska. We used Low-Redux to perform the following tasks: (1) process the flats, (2) use arcs to make a two-dimensional wavelength image, (3) make a slit profile, (4) create a sky model, (5) process the images, and (6) identify objects in the slit and trace them. The standard spectral extraction techniques included in Low-Redux had difficulty with blended objects such as ours. Instead, we binned a 30 pixel region along the spatial direction and determined the central 3 – 7 spatial rows where 95% of the continuum flux was contained (always covering the separation between the main galaxy and the companion galaxy as measured from the NIRC2 imaging), and then extracted a summed spectrum for each object using the Lox-Redux traces and the measured central spatial pixels. To mosaic individual exposures

[15]http://www.ucolick.org/ xavier/LowRedux/index.html

for higher S/N, the Low-Redux traces were used to determine the relative offsets of each subsequent frame to the first, and then to sum the frames by splitting the flux fractionally between the pixels. The reduced long-slit images and extracted spectra are displayed in Figures 5.1–5.10.

After extracting the final spectrum, we used *MPFIT* to independently fit two or three Gaussians and a linear continuum to both the Hβ and [O III] λ5008Å lines using noise estimates derived from the Poisson noise of the raw frames (so that sky lines will have higher noise levels). Errors for the Gaussian peak parameters were estimated using the same techniques described in Section 4.2 for our OSIRIS spectra fitting.

Once we determined the wavelength centers of the two [O III] λ5008Å emission peaks, we measured the spatial centroid of each emission peak individually. For each peak, we summed the flux over a 10 Å rest wavelength window centered on the peak's wavelength center, creating a map of summed flux versus the spatial direction. We then fitted one or two Gaussians to the summed flux to locate its spatial centroid(s); the second Gaussian was used to test if any of the peak flux was coming from the companion galaxy. These positions are shown in Figures 5.1 – 5.10 as white-outlined black diamonds on top of each emission peak. Errors on these positions were estimated by two techniques. The first technique was similar to that used in the spectral fitting: estimate the standard deviation of the best fit subtracted from the summed flux distribution, add 300 iterations of randomly generated noise to the best fit spatial Gaussians, fit new spatial Gaussians, and measure the standard deviations of each parameter as the first error estimation. The second technique created 100 different summed spectra by mov-

ing the center of the 10 Å rest wavelength window around according to the error of the wavelength centers, and then fitted new spatial Gaussians and measured the standard deviations of the parameters as the second error estimation. These two estimations were summed in quadrature to get the final error.

Hβ is not detected in 5 of the 10 galaxies observed with Kast; we can however estimate the maximum flux that could be hidden in the noise of our spectra. These estimates place upper limits on the flux of a single Hβ peak that could be hidden, and thus can be used to conservatively calculate minimum [O III]/Hβ ratios. To calculate these upper limits on Hβ, we measure the standard deviation of the summed spectrum in a 140 Å window centered around the line's expected position and use this as an estimation of the noise of the spectrum. We create 100 unique simulated spectra by randomly generating noise spectra and then injecting a single Gaussian peak into each with heights increasing smoothly from 0.05 to 5 times the noise level. To understand when the injected Gaussian peak becomes noticeable and measurable, we attempt to fit a Gaussian to each simulated spectrum using *MPFIT*, with the parameters of the input Gaussian peak as the initial estimate of the fitting parameters. By taking the difference of the fluxes of the fitted peaks and the fluxes of the injected peaks, we can measure when the fitted parameters begin to match the injected parameters. The final maximum possible flux is determined by constraining the difference between the mean fitted peak fluxes and the injected peak fluxes to be less than the flux error from the fitting procedure.

5.3 Discussion of the 10 Candidates

In the Kast sample we detect two [O III] peaks in 9 of our 10 candidates. In the 10th candidate, J0725+3744, we only detect one peak because the 2nd peak is obliterated by a strong sky line (Figure 5.2). The velocity differences between the Kast-observed [O III] peaks match those of the SDSS [O III] peaks within one sigma in 6 of the 9 candidates (67%) and within three sigma in 2 additional candidates (89%). In J1051+6251, the remaining candidate, the Kast [O III] velocity difference and peak flux ratio (respectively, 317±8 km s^{-1} and 0.3) is quite different from the SDSS [O III] velocity difference and peak flux ratio (421±10 km s^{-1} and 1.0), as shown in Figure 5.4 and Table 5.2; since the 3″ diameter SDSS fiber and our 1″ slit cover different regions of the object, we may be missing additional higher velocity flux with wider separations.

While our measured velocities match most of those measured in the SDSS spectra, the spatial separations measured between the two [O III] peaks (described in Section 5.2) are grouped into three categories, discussed below. We note that our measured separation for J1307+4604, 0.″41, is similar to the 0.″61 separation measured in Comerford et al. (2012).

1. *Spatially Coincident Peaks:* In three of our candidates (J0940+3113 and J1051+-6251 in Figures 5.3–5.4 and J1157+0816 in Figure 5.6), the two emission peaks are spatially coincident down to less than 0.″15 (430 pc, 850 pc, and 490 pc). The observed companions have separations of, respectively, 2.″45, 1.″52, and 2.″61 (7.1 kpc, 8.6 kpc, and 8.6 kpc). Fu et al. (2012) finds the same spatially coincident peaks for J0940+3113 and observes spatially extended peaks for J1051+6251 that

do not appear in our observations. Spatially coincident double emission lines can be caused by several scenarios, all unresolved: dual AGNs, small-scale outflows or jets, rings of star formation, gas disks, or complicated narrow line region kinematics. BPT diagrams can sometimes distinguish between the aforementioned cases. In this case, the BPT diagrams in the Figures show that the three objects with spatially coincident peaks have ambiguous [O III]/Hβ ratios, not distinguishing between any of the scenarios.

2. *Spatially Mismatched Peaks:* Four of our candidates (J0803+4836 in Figure 5.1, J1307+4604 in Figure 5.7, and J1610+1308 and J1652+3107 in Figures 5.9–5.10) show a measurable spatial separation between their emission peaks ($0\farcs20$, $0\farcs41$, $0\farcs43$, and $0\farcs28$; 1.4 kpc, 2.0 kpc, 1.6 kpc, and 0.4 kpc) that is not consistent with the second emission peak originating in the companion galaxy identified from our imaging ($2\farcs63$, $2\farcs37$, $2\farcs35$, and $2\farcs96$; 18.0 kpc, 11.6 kpc, 8.6 kpc, and 4.2 kpc). We also do not measure any continuum emission from either the companion galaxy or the location of the second [O III] peak in any of these cases. This mismatch of separations may mean that the double-peaked lines in these objects originate in kpc-scale outflows driven by an AGN or star formation, jets, rings of star formation, or rotating gas disks. Fu et al. (2012) see spatially extended [O III] emission for J1307+4604, supporting the outflow theory for this object. The BPT diagrams for all four objects, shown in their Figures (5.1, 5.7, 5.9–5.10), have [O III]/Hβ ratios likely caused by AGN because they are too high to be caused by star formation. These high [O III]/Hβ ratios indicate that there is at least one

AGN present in each object; combined with the high ratios, the mismatched but measurable spatial separations of the double emission peaks may indicate that the second emission peak is due to outflows or inflows; integral field spectroscopy is needed to see the full extent of the second emission peaks.

3. *Peaks Spatially Matched to Galaxies:* Finally, in J1146+5110 (Figure 5.5) and J1332+0606 (Figure 5.8) we measure a spatial separation between the two emission peaks that is consistent with the second peak originating in the companion galaxy. For J1146+5110, we see that the red peak of the [O III] line is diffuse and spatially extended out past the measured near-IR separation between the two galaxies, linking the emission of the red peak to the companion. In the BPT diagram in Figure 5.5, the [O III]/Hβ ratios for the two galaxies of J1146+5110 indicates that it is a dual AGN. This conclusion agrees with Liu et al. (2013)'s detection of two AGNs in their X-ray observations. Although Fu et al. (2012) see extended red peak [O III] emission coincident with the companion galaxy of J1146+5110, they classify it as an extended narrow line region. The separation between the [O III] peaks of J1332+0606 matches the near-IR separation exactly, illustrating that the companion is responsible for the blue [O III] peak. However, examining J1332+0606's BPT diagram shows that the [O III]/Hβ ratios for both galaxies are in the star formation and LINERs/composite region, so while J1332+0606 may in fact be a dual AGN with ongoing star formation in both galaxies, our data do not prove the presence of two AGNs. We note that Liu et al. (2013) prove the presence of an AGN in the companion galaxy with their X-ray observations, but get no

counts from the main galaxy. Fu et al. (2012) observe red peak [O III] emission coincident with the companion galaxy and blue peak [O III] emission coincident with the main galaxy, and classify the companion as an extended narrow line region. There is a notable difference in the [O III] λ5008Å profiles for our Kast spectra and the SDSS spectra; this suggests that the SDSS fiber may have missed the bulk of the emission from the companion galaxy.

Many of the extracted spectra in the Kast sample have different flux ratios between the two [O III] λ5008Å peaks than the flux ratios of the same peaks as measured by the SDSS spectra. In our Kast spectra, our 1-2$''$ slits were oriented to cover both galaxies along the spatial direction; our position angle errors from measuring the angle from the NIRC2 images and from orienting the spectrograph are extremely small, $\approx 1^{\circ}$, in order to better measure flux from the companions. In the SDSS spectra, the source of both peaks must be within 1.$''$5 of the fiber's central position on the main galaxy; this radius leaves much of the companion galaxies either partially or entirely uncovered by the fiber, suggesting that the SDSS spectra could be missing flux from the companion galaxies. Indeed, for the two pairs of galaxies with matching separations, the flux ratios between our Kast observations and the SDSS spectra do not match, with the peak of the companion being stronger than observed with SDSS. Conversely, if the emission of the 2nd peak is spatially extended in the direction perpendicular to the orientation of the Kast slit, such as in a randomly-oriented outflow, our Kast spectra would miss flux from the 2nd peak that the circular SDSS fiber might have observed. This seems to be case for 3 of our 7 candidates, with 3-sigma differing [O III] flux ratios in 1 of 3 objects with

spatially coincident peaks and 3 of 4 objects with mismatched peak separations. We suggest that these disagreements result from the fact that SDSS and our Kast spectra are extracted from differing spatial regions.

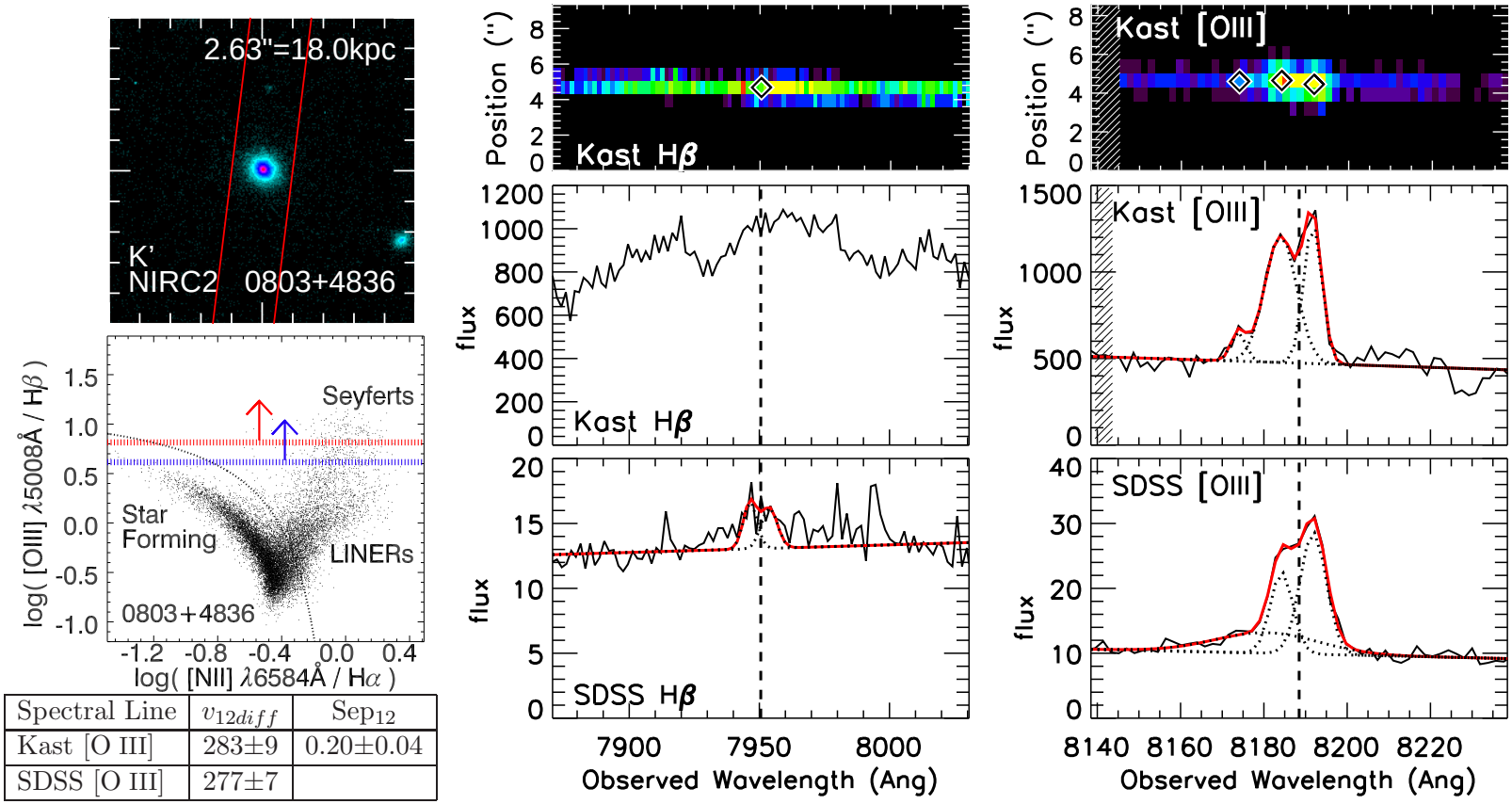

Spectral Line	v_{12diff}	Sep_{12}
Kast [O III]	283±9	0.20±0.04
SDSS [O III]	277±7	

Figure 5.1: Keck LGS AO NIRC2 imaging, Shane Kast long-slit spectroscopy, and SDSS spectroscopy of J0803+4836 (z=0.635). See next page for the caption.

Figure 5.1: (previous page) Keck LGS AO NIRC2 imaging, Shane Kast long-slit spectroscopy, and SDSS spectroscopy of J0803+4836 (z=0.635). Figures 5.2-5.10 follow the same format as this Figure. The **top left** panel shows the NIRC2 camera $10'' \times 10''$ log-scale image, with the outline of the Kast long-slit overplotted in red. North is up and East is left. The **middle left** BPT diagram plots the listed flux ratios. Without measured [N II]/Hα ratios, we plots the measured [O III]/Hβ for the blue (red) emission peaks as blue (red) lines across the diagram. Some objects had measurable Hβ flux; the flux ratios of these objects are plotted as solid lines. The objects with no measurable Hβ peaks have a maximum possible flux estimated; the flux ratios for these objects, plotted as dotted lines with solid arrows, are lower limits on the possible flux ratio. The **bottom left** table contains a comparison of the velocity difference and peak spatial separation for the lines fitted in the spectra displayed. The **center** and **right** columns show the spectra for Hβ and [O III] λ5008Å, respectively. In both columns, the **top** color images plot the flux as it changes in intensity over the position along the slit and over wavelength. A diamond shows the wavelength and spatial centers of each fitted emission line, or their predicted center if no fit was possible. The **middle** and **bottom** rows show, respectively, the Kast long-slit and the SDSS fiber spectra. If a fit to the emission line was possible, the total fit (solid red) and components (dotted black) are plotted. The dashed vertical line illustrates the main SDSS AGN's central wavelength. Greyed out regions indicate the presence of a saturated sky line that could not be subtracted correctly. J0803+4836 shows a measurable separation between its double [O III] peaks ($0\farcs20$ = 1.4 kpc) that does not match the near-IR separation between the two galaxies ($2\farcs63$ = 18.0 kpc). The strong [O III]/Hβ ratios for the two peaks and the spatial separation of the peaks indicate that an AGN-driven outflow may be the source of the second [O III] peak.

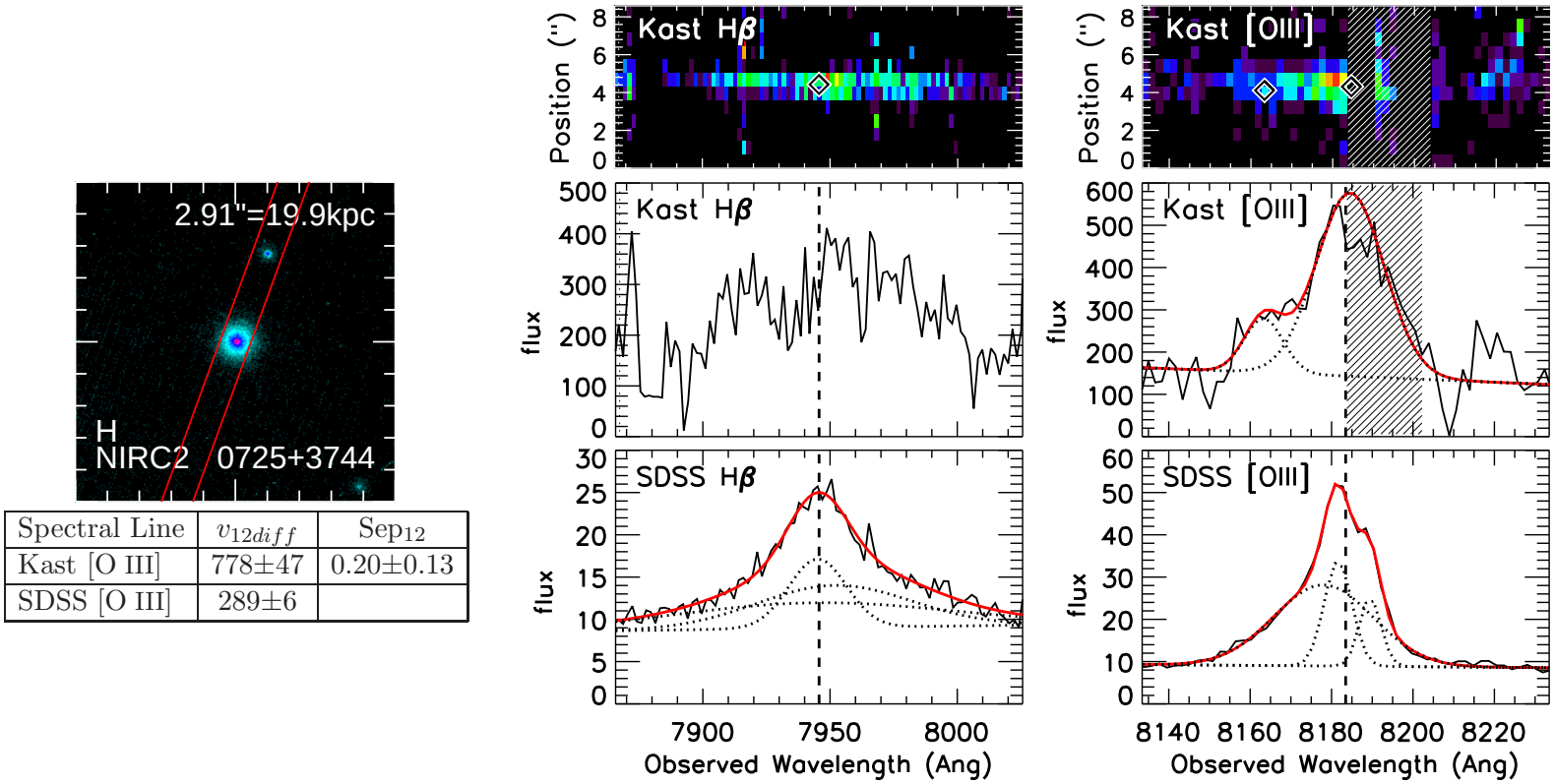

Spectral Line	v_{12diff}	Sep_{12}
Kast [O III]	778±47	0.20±0.13
SDSS [O III]	289±6	

Figure 5.2: Keck LGS AO NIRC2 imaging and Shane Kast long-slit spectroscopy of J0725+3744 (z=0.634). Please see the caption of Figure 5.1 for a full description of each panel. In J0725+3744, the 2nd [O III] emission peak is obliterated by a strong sky line, preventing interpretation.

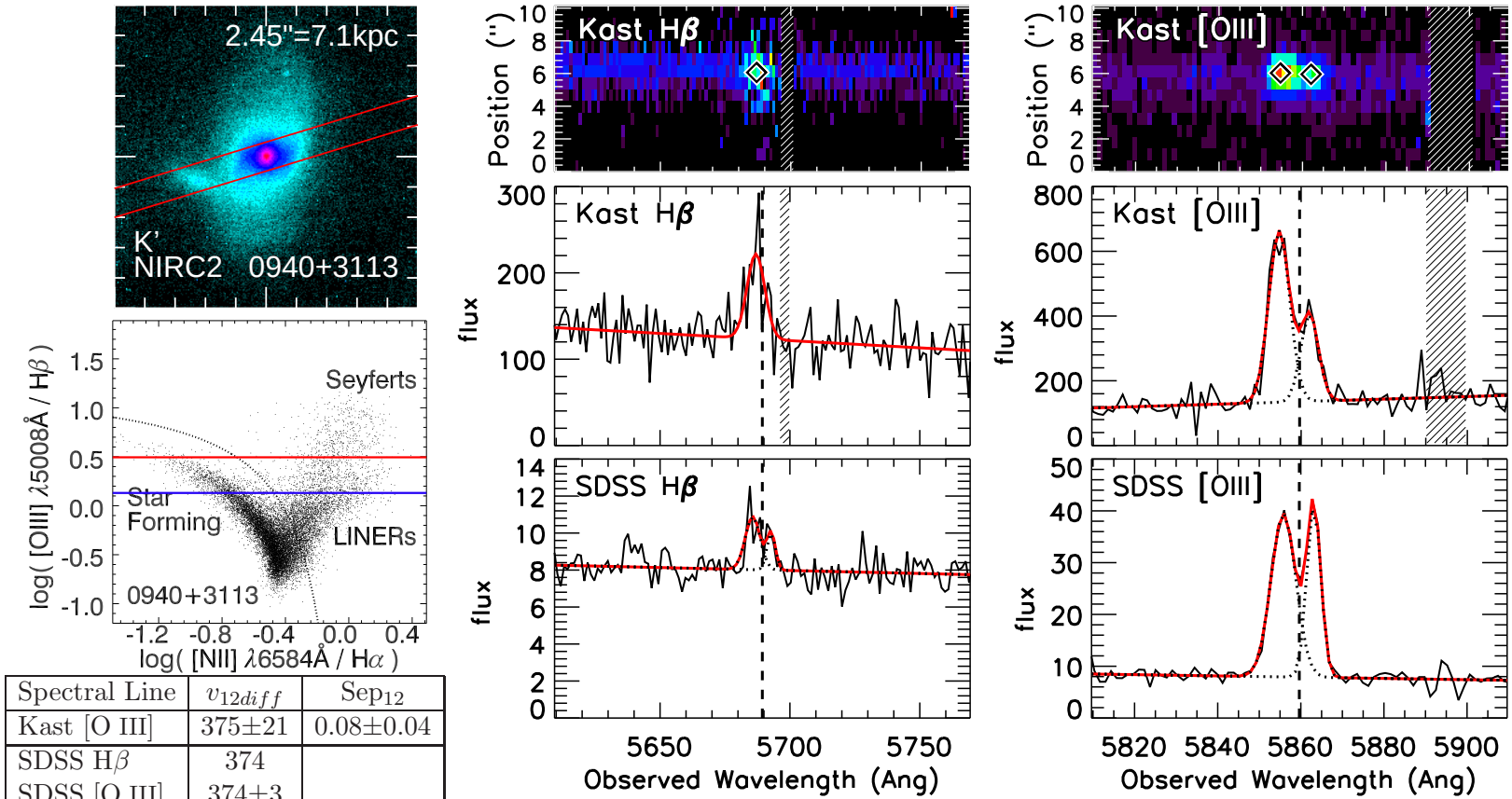

Spectral Line	v_{12diff}	Sep_{12}
Kast [O III]	375±21	0.08±0.04
SDSS Hβ	374	
SDSS [O III]	374±3	

Figure 5.3: Keck LGS AO NIRC2 imaging and Shane Kast long-slit spectroscopy of J0940+3113 (z=0.170). Please see the caption of Figure 5.1 for a full description of each panel. J0940+3113 has double [O III] peaks that are spatially coincident, or separated by a negligible amount. Spatially coincident double emission lines can be caused by several scenarios, all unresolved: binary AGNs, small-scale outflows or jets, rings of star formation, gas disks, or complicated narrow line region kinematics.

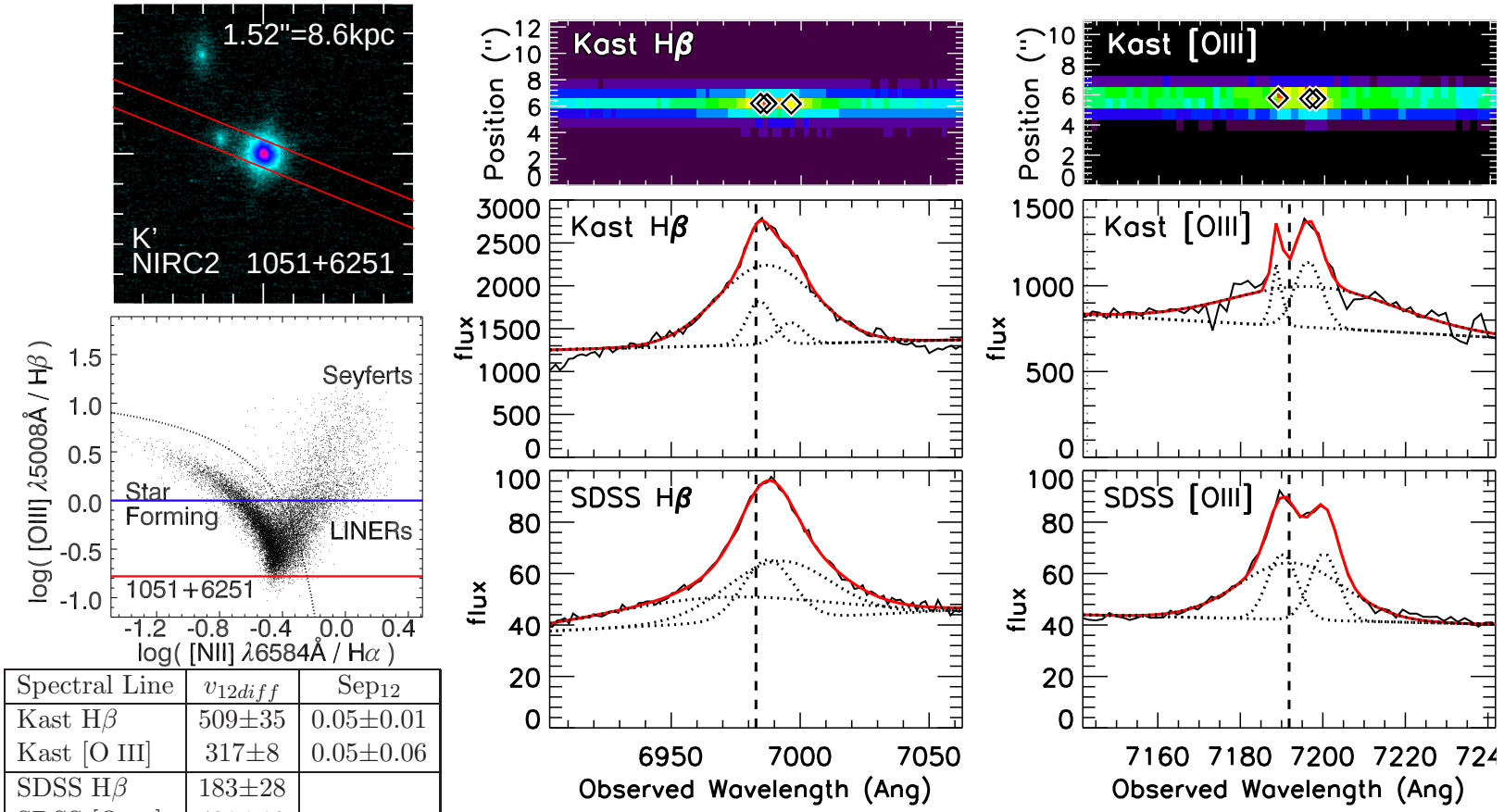

Spectral Line	v_{12diff}	Sep_{12}
Kast Hβ	509±35	0.05±0.01
Kast [O III]	317±8	0.05±0.06
SDSS Hβ	183±28	
SDSS [O III]	421±10	

Figure 5.4: Keck LGS AO NIRC2 imaging and Shane Kast long-slit spectroscopy of J1051+6251 (z=0.436). Please see the caption of Figure 5.1 for a full description of each panel. J1051+6251 has double [O III] peaks that are spatially coincident, or separated by a negligible amount. Spatially coincident double emission lines can be caused by several scenarios, all unresolved: binary AGNs, small-scale outflows or jets, rings of star formation, gas disks, or complicated narrow line region kinematics.

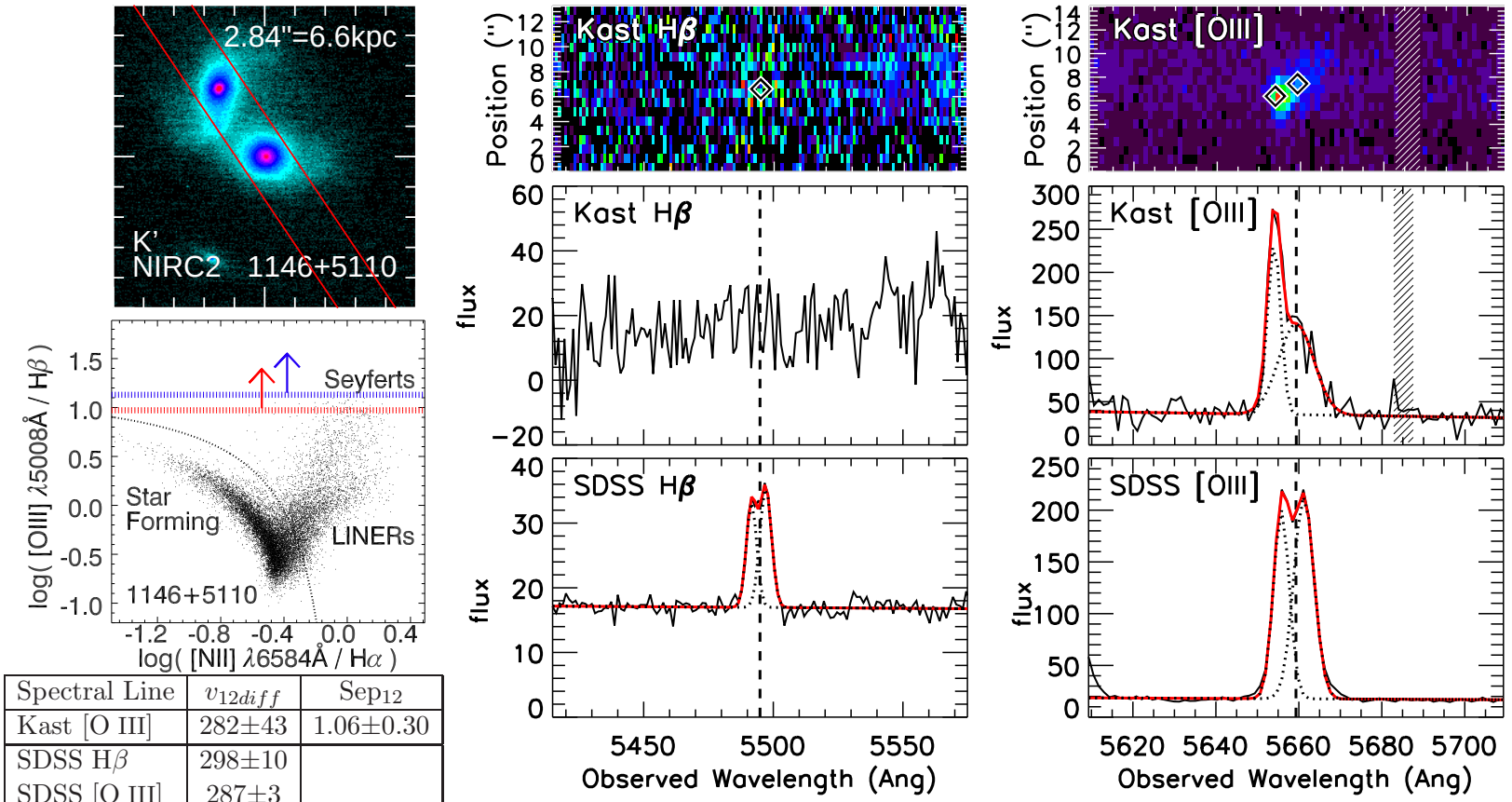

Spectral Line	v_{12diff}	Sep_{12}
Kast [O III]	282±43	1.06±0.30
SDSS Hβ	298±10	
SDSS [O III]	287±3	

Figure 5.5: Keck LGS AO NIRC2 imaging and Shane Kast long-slit spectroscopy of J1146+5110 (z=0.130). Please see the caption of Figure 5.1 for a full description. The separation of the two [O III] peaks is measured to be 1.″1. However, the red peak is quite diffuse, with emission extending beyond the blue peak by more than 2.″84, the near-IR separation between the galaxies. This wide separation firmly links the emission of the red peak to the companion galaxy. The BPT diagram shows that the [O III]/Hβ ratios make J1146+5110 a dual AGN.

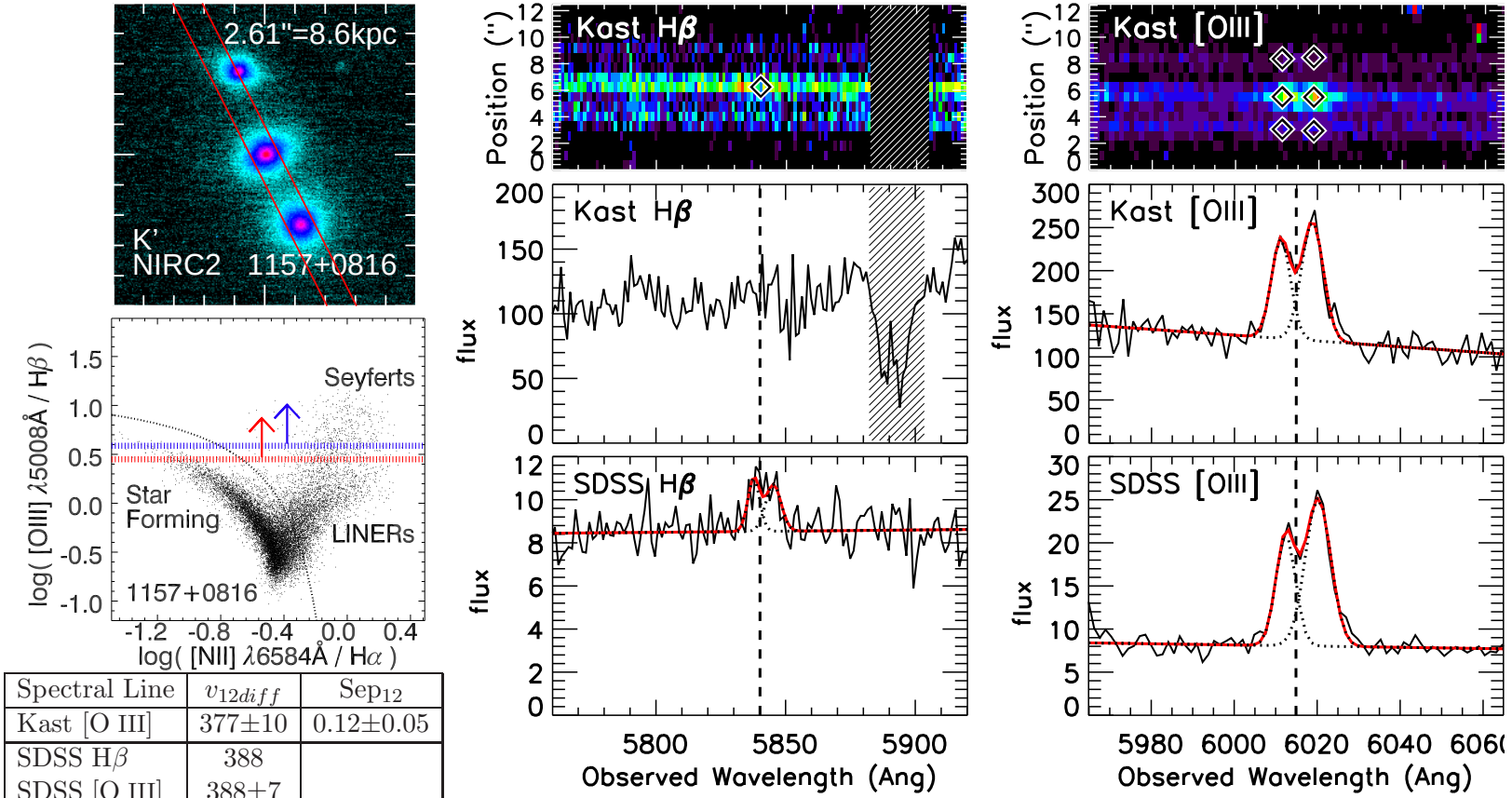

Spectral Line	v_{12diff}	Sep_{12}
Kast [O III]	377±10	0.12±0.05
SDSS Hβ	388	
SDSS [O III]	388±7	

Figure 5.6: Keck LGS AO NIRC2 imaging and Shane Kast long-slit spectroscopy of J1157+0816 (z=0.201). Please see the caption of Figure 5.1 for a full description. Similar to the OSIRIS observations in Figure 4.7 and Subsection 4.3.4, J1157+0816 shows negligible spatial separation between the two peaks, indicating that the companions are not responsible for the 2nd [O III] peak. Spatially coincident double emission lines can be caused by several scenarios, all unresolved: binary AGNs, small-scale outflows or jets, rings of star formation, gas disks, or complicated narrow line region kinematics. Unfortunately, the BPT diagram shows that the [O III]/Hβ ratios could be caused by AGN activity or star formation.

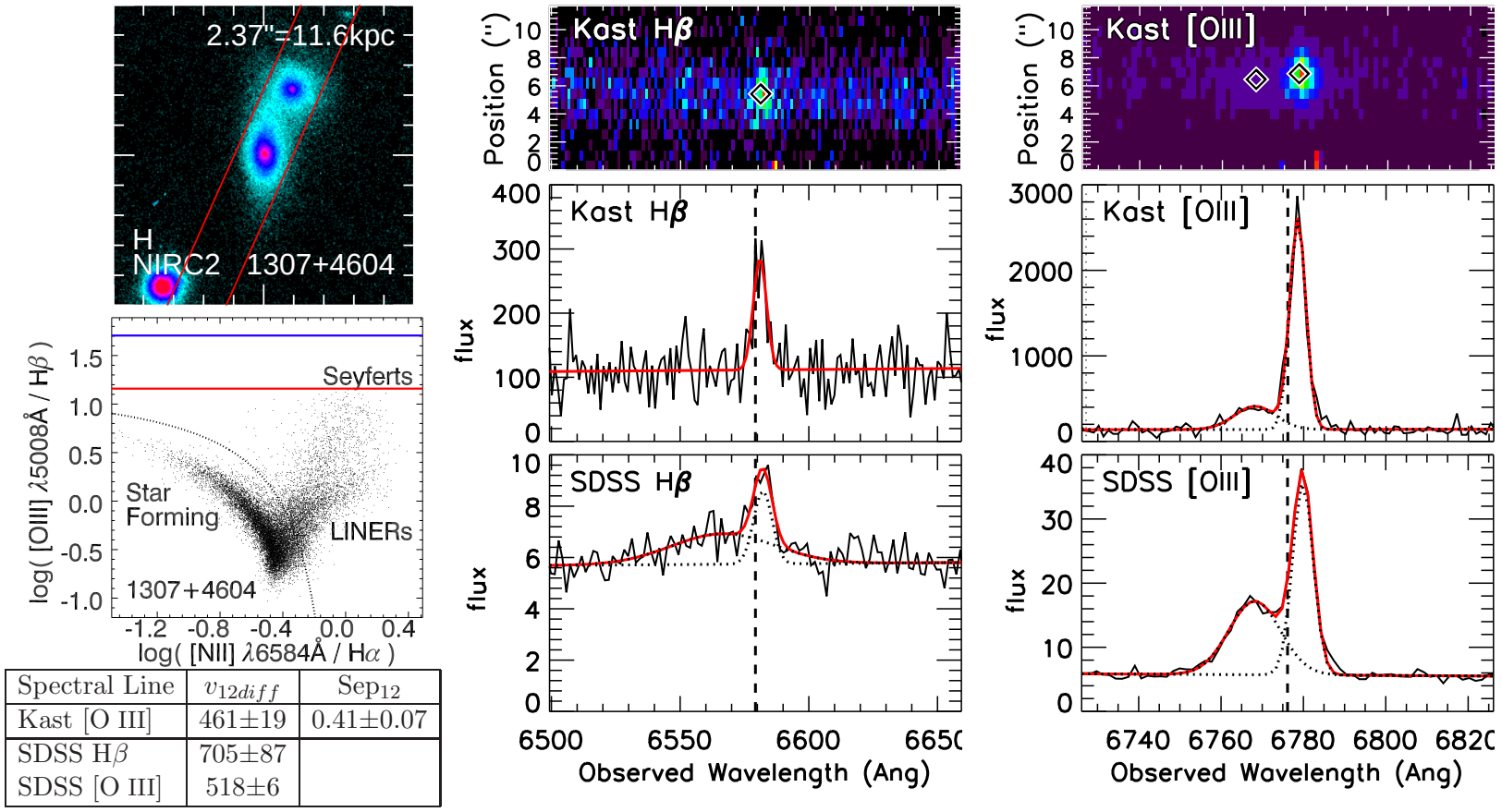

Spectral Line	v_{12diff}	Sep_{12}
Kast [O III]	461±19	0.41±0.07
SDSS Hβ	705±87	
SDSS [O III]	518±6	

Figure 5.7: Keck LGS AO NIRC2 imaging and Shane Kast long-slit spectroscopy of J1307+4604 (z=0.353). Please see the caption of Figure 5.1 for a full description of each panel. J1307+4604 shows 0.″41 (2.0 kpc) separation between its [O III] peaks, which falls short of the 2.″37 (11.6 kpc) separation between the two galaxies. The strength of the [O III]/Hβ ratios for both peaks and the spatial separation between the peaks indicate that an AGN-driven outflow may be the source of the second [O III] peak.

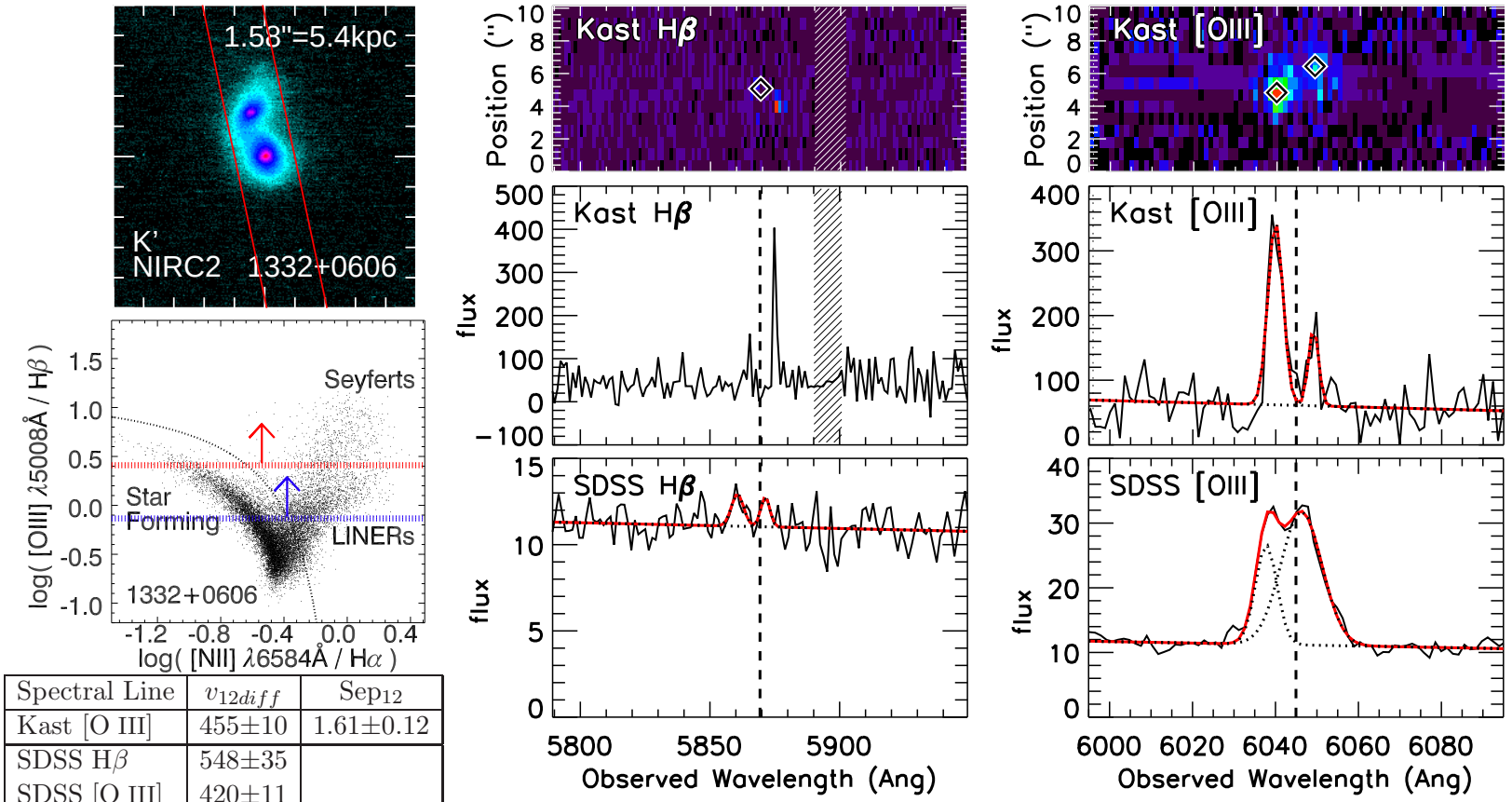

Spectral Line	v_{12diff}	Sep$_{12}$
Kast [O III]	455±10	1.61±0.12
SDSS Hβ	548±35	
SDSS [O III]	420±11	

Figure 5.8: Keck LGS AO NIRC2 imaging and Shane Kast long-slit spectroscopy of J1332+0606 (z=0.207). Please see the caption of Figure 5.1 for a full description of each panel. J1332+0606 has a separation between the two [O III] peaks (1.″61) that matches the 1.″58 near-IR separation between the two galaxies. The BPT diagram shows that the lower limits for both galaxies fall in the Composite/LINER region, leaving the object's status as a dual AGN unknown. The disparity between the [O III] peak fluxes in the Kast and SDSS observations argue that the fiber missed part of the companion's blue [O III] emission.

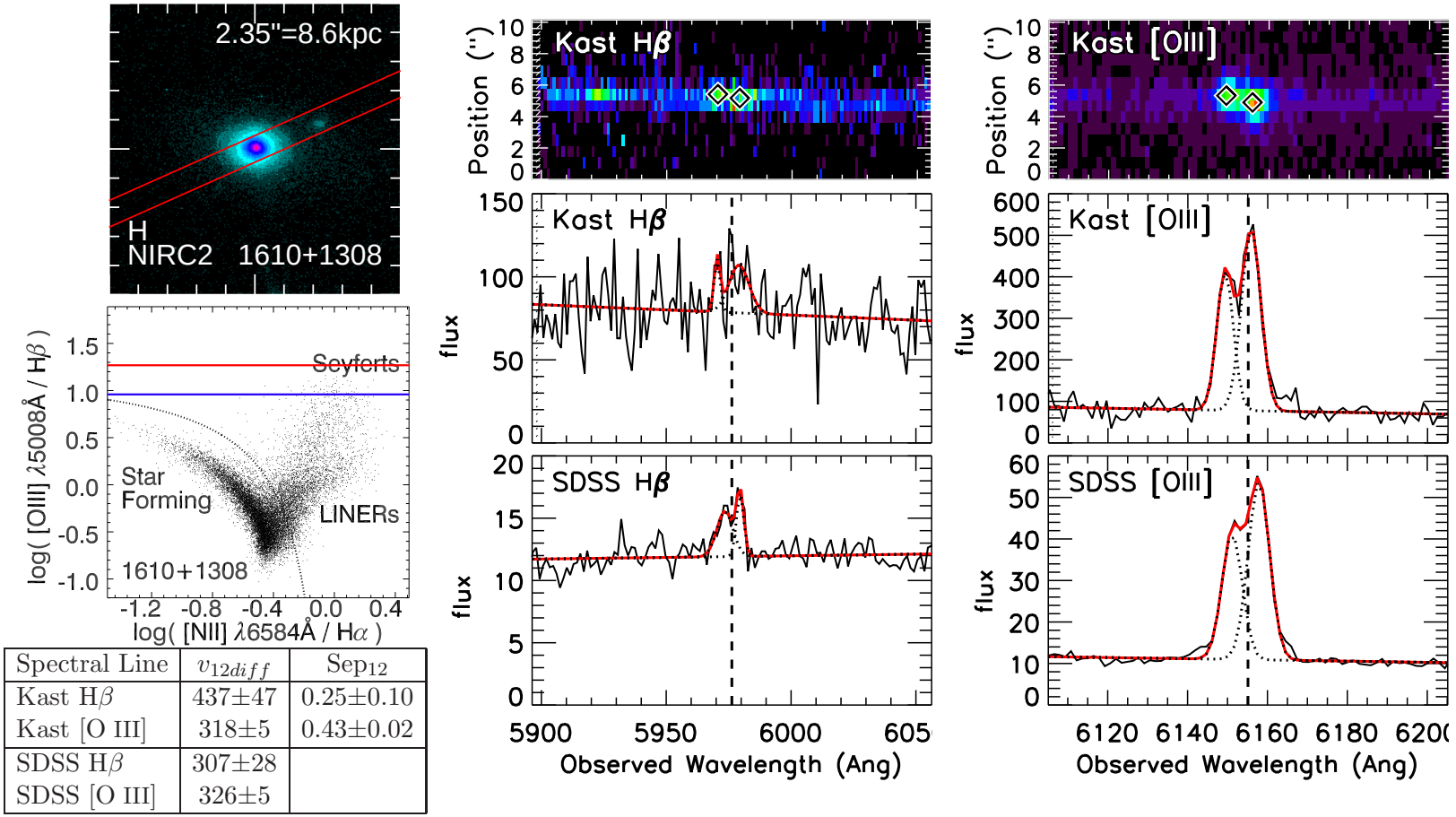

Spectral Line	v_{12diff}	Sep_{12}
Kast Hβ	437±47	0.25±0.10
Kast [O III]	318±5	0.43±0.02
SDSS Hβ	307±28	
SDSS [O III]	326±5	

Figure 5.9: Keck LGS AO NIRC2 imaging and Shane Kast long-slit spectroscopy of J1610+1308 (z=0.229). Please see the caption of Figure 5.1 for a full description. J1610+1308 shows measurable spatial separation between its double [O III] peaks ($0\farcs43 = 1.6$ kpc) that does not match the near-IR separation between the two galaxies ($2\farcs35 = 8.6$ kpc). The [O III]/Hβ ratios and the spatial separation between both peaks indicate that AGN-driven outflows may be the source of the second [O III] peak.

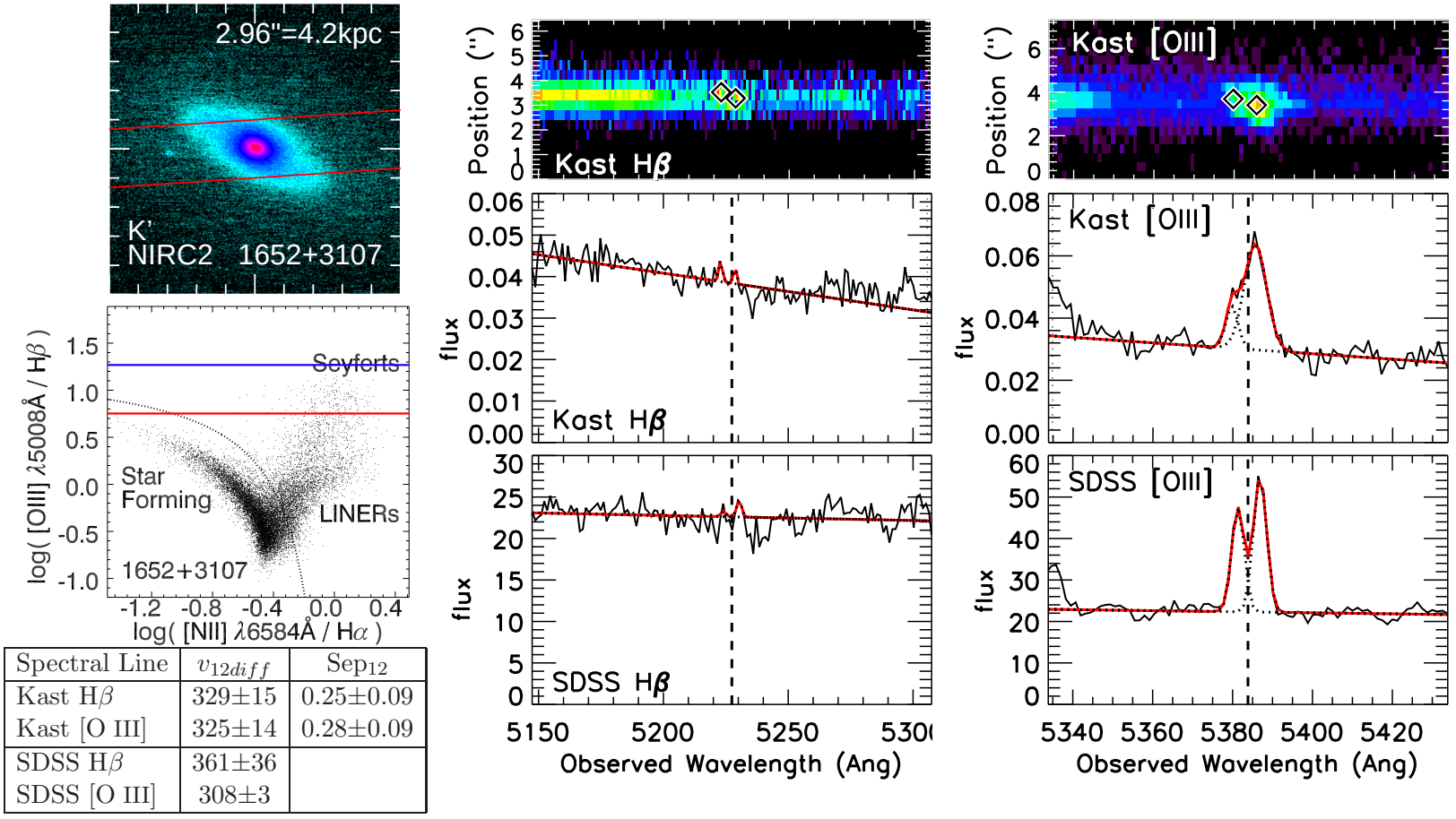

Spectral Line	v_{12diff}	Sep_{12}
Kast Hβ	329±15	0.25±0.09
Kast [O III]	325±14	0.28±0.09
SDSS Hβ	361±36	
SDSS [O III]	308±3	

Figure 5.10: Keck LGS AO NIRC2 imaging and Shane Kast long-slit spectroscopy of J1652+3107 (z=0.075). Please see the caption of Figure 5.1 for a full description. J1652+3107 shows measurable spatial separation between its double [O III] peaks ($0''.28 = 0.4$ kpc) that does not match the near-IR separation between the two galaxies ($2''.96 = 4.2$ kpc). The [O III]/Hβ ratios and the spatial separation between both peaks indicate that AGN-driven outflows may be the source of the second [O III] peak.

Table 5.2: Measured Velocities and Separations for Shane Kast Long-Slit Spectra

Spectral Line	v_{12diff}[16,17]	v_1[16,17]	v_2[16,17]	v_3[16,17]	Sep$_1$ ($''$)	Sep$_2$ ($''$)	Sep$_3$ ($''$)	F_1/F_2[18]	F_1/F_3[18]
J0725+3744									
Kast [O III] λ5008Å	778±47	-738^{+42}_{-44}	40^{+22}_{-15}		0.00±0.12	0.20±0.04		0.2±0.1	
SDSS Hβ	253±221	-21^{+16}_{-25}	231^{+240}_{-199}	-83^{+365}_{-124}				0.6±0.2	0.6±0.2
SDSS [O III] λ4959Å	280±13	-46^{+8}_{-8}	234^{+10}_{-10}	-227^{+26}_{-23}				2.1±0.3	0.4±0.6
SDSS [O III] λ5008Å	289±6	-68^{+4}_{-3}	220^{+5}_{-4}	-199^{+6}_{-8}				2.0±0.1	0.4±0.3
J0803+4836									
Kast [O III] λ5008Å	283±9	-163^{+8}_{-8}	120^{+4}_{-6}	-533^{+16}_{-13}	0.20±0.03	0.00±0.03	0.15±0.03	1.6±0.2	9.5±2.8
SDSS Hβ	277	-154	123					1.0±0.2	
SDSS [O III] λ4959Å	302±15	-222^{+13}_{-10}	80^{+11}_{-8}	-474^{+216}_{-129}				0.5±0.1	1.9±2.7
SDSS [O III] λ5008Å	277±7	-154^{+6}_{-6}	123^{+4}_{-5}	-284^{+46}_{-54}				0.6±0.0	0.9±0.7
J0940+3113									
Kast Hβ		-131^{+13}_{-17}			0.00±0.12				
Kast [O III] λ5008Å	375±21	-251^{+9}_{-10}	123^{+18}_{-18}		0.08±0.03	0.00±0.03		2.3±0.5	
SDSS Hβ	374	-195	178					2.5±0.3	
SDSS [O III] λ4959Å	346±10	-165^{+9}_{-9}	181^{+5}_{-6}					1.7±0.2	

Continued on next page

Table 5.2 – *Continued from previous page*

Spectral Line	v_{12diff}[16,17]	v_1[16,17]	v_2[16,17]	v_3[16,17]	Sep$_1$ ($''$)	Sep$_2$ ($''$)	Sep$_3$ ($''$)	F_1/F_2[18]	F_1/F_3[18]
SDSS [O III] λ5008Å	374±3	-195$^{+3}_{-3}$	178$^{+2}_{-2}$					1.7±0.1	
J1051+6251									
Kast Hβ	509±35	63$^{+8}_{-20}$	572$^{+19}_{-43}$	167$^{+8}_{-9}$	0.05±0.01	0.00±0.01	0.03±0.01	2.0±0.3	0.1±0.0
Kast [O III] λ5008Å	317±8	-126$^{+5}_{-4}$	191$^{+8}_{-6}$	253$^{+33}_{-35}$	0.05±0.01	0.01±0.06	0.00±0.06	0.3±0.0	0.1±0.0
SDSS Hβ	183±28	195$^{+5}_{-10}$	378$^{+26}_{-28}$	-671$^{167}_{62}$				0.5±0.0	0.5±0.2
SDSS [O III] λ4959Å	423±16	-119$^{+12}_{-12}$	304$^{+12}_{-11}$					0.9±0.1	
SDSS [O III] λ5008Å	421±10	-68$^{+8}_{-7}$	353$^{+6}_{-7}$	20$^{+13}_{-16}$				1.0±0.1	0.3±0.7
J1146+5110									
Kast [O III] λ5008Å	282±43	-283$^{+8}_{-5}$	-1$^{+51}_{-34}$		0.00±0.03	1.06±0.30		0.7±0.2	
SDSS Hβ	298±10	-178$^{+7}_{-8}$	120$^{+7}_{-7}$					0.8±0.1	
SDSS [O III] λ4959Å	288±7	-188$^{+5}_{-4}$	99$^{+6}_{-5}$					0.7±0.0	
SDSS [O III] λ5008Å	287±3	-186$^{+2}_{-2}$	101$^{+2}_{-2}$					0.7±0.0	
J1157+0816									
Kast [O III] λ5008Å	377±10	-183$^{+8}_{-7}$	194$^{+7}_{-6}$		0.12±0.04	0.00±0.02		0.7±0.1	
SDSS Hβ	388	-123	265					0.9±0.1	
SDSS [O III] λ4959Å	384±13	-82$^{+11}_{-11}$	302$^{+7}_{-7}$					1.4±0.2	

Continued on next page

Table 5.2 – *Continued from previous page*

Spectral Line	v_{12diff}[16,17]	v_1[16,17]	v_2[16,17]	v_3[16,17]	Sep$_1$ ($''$)	Sep$_2$ ($''$)	Sep$_3$ ($''$)	F_1/F_2[18]	F_1/F_3[18]
SDSS [O III] λ5008Å	388±7	-123$^{+6}_{-4}$	265$^{+5}_{-4}$					0.6±0.0	
J1307+4604									
Kast Hβ		79$^{+8}_{-9}$			0.00±0.07				
Kast [O III] λ5008Å	461±19	-353$^{+17}_{-21}$	107$^{+1}_{-1}$		0.00±0.07	0.41±0.01		0.3±0.0	
SDSS Hβ	705±87	-574$^{+84}_{-87}$	131$^{+12}_{-10}$					2.3±0.3	
SDSS [O III] λ4959Å	479±18	-299$^{+18}_{-19}$	180$^{+2}_{-3}$					1.3±0.1	
SDSS [O III] λ5008Å	518±6	-353$^{+6}_{-7}$	165$^{+1}_{-1}$					1.0±0.0	
J1332+0606									
Kast [O III] λ5008Å	455±10	-249$^{+5}_{-4}$	207$^{+8}_{-9}$		0.00±0.04	1.61±0.12		3.5±0.7	
SDSS Hβ	548±35	-444$^{+28}_{-27}$	105$^{+24}_{-20}$					1.4±0.7	
SDSS [O III] λ4959Å	405±10	-368$^{+4}_{-5}$	37$^{+8}_{-9}$					0.3±0.0	
SDSS [O III] λ5008Å	420±11	-355$^{+6}_{-5}$	65$^{+11}_{-8}$					0.4±0.0	
J1610+1308									
Kast Hβ	437±47	-294$^{+19}_{-18}$	143$^{+45}_{-38}$		0.25±0.05	0.00±0.08		0.3±0.4	
Kast [O III] λ5008Å	318±5	-282$^{+4}_{-4}$	36$^{+4}_{-3}$		0.43±0.02	0.00±0.02		0.7±0.0	
SDSS Hβ	307±28	-140$^{+22}_{-30}$	167$^{+9}_{-9}$					1.6±0.4	

Continued on next page

Table 5.2 – *Continued from previous page*

Spectral Line	v_{12diff}[16,17]	v_1[16,17]	v_2[16,17]	v_3[16,17]	Sep$_1$ ($''$)	Sep$_2$ ($''$)	Sep$_3$ ($''$)	F_1/F_2[18]	F_1/F_3[18]
SDSS [O III] λ4959Å	321±12	-153$^{+11}_{-10}$	167$^{+6}_{-6}$					1.2±0.1	
SDSS [O III] λ5008Å	326±5	-193$^{+4}_{-4}$	133$^{+3}_{-3}$					0.7±0.0	
J1652+3107									
Kast Hβ	329±15	-259$^{+18}_{-8}$	69$^{+7}_{-8}$		0.25±0.06	0.00±0.07		0.7±1.9	
Kast [O III] λ5008Å	325±14	-226$^{+13}_{-12}$	99$^{+9}_{-6}$		0.28±0.09	0.00±0.03		0.2±0.0	
SDSS Hβ	361±36	-194$^{+25}_{-31}$	167$^{+21}_{-23}$					0.3±0.3	
SDSS [O III] λ4959Å	324±10	-166$^{+7}_{-8}$	158$^{+7}_{-6}$					0.6±0.1	
SDSS [O III] λ5008Å	308±3	-139$^{+2}_{-2}$	168$^{+2}_{-2}$					0.7±0.0	

[16] Velocities in km s^{-1}, measured with respect to the main galaxy's [O III] blue component.

[17] 1σ measurement errors.

[18] Line flux ratio: main galaxy to companion galaxy.

Chapter 6

Spectroscopic Conclusions

To confirm candidate dual AGNs selected via double-peaked [O III] emission lines or multiple bright cores imaged in a single galaxy, spatially resolved spectroscopy is required. We presented spatially resolved integral field and long-slit spectroscopy of 13 candidate dual AGNs to compare the spatial separations of the main and companion galaxies to the spatial separations of the two [O III] peaks. Overall, we found:

- *Two dual AGNs.* J0952+2552 has two tight [O III] peaks matching the location of the main and companion galaxies. The main galaxy hosts a Type 1 AGN; both optical and near-IR diagnostics ([O III]/Hβ and [Fe II]/Paβ, respectively) indicate that the companion galaxy also contains an AGN. J1146+5110 has a spatially diffuse second [O III] peak encompassing the location of the companion galaxy and [O III]/Hβ ratios that identify both peaks as AGN. This is consistent with Liu et al. (2013)'s detection of two X-ray AGNs at these locations.

- *Five systems with outflows.* In J0916+2835 we map the spatially extended out-

flow in Paα and H_2 λ1.835μm, stretching from 1-2 kpc from the main AGN, with a velocity difference matching the velocity difference observed by SDSS. In J0803+4836, J1307+4604, J1610+1308, and J1652+3107, we measure a noticeable spatial separation between the two [O III] peaks that does not match the spatial separation between the main galaxy and its near-IR companion, indicating that the second [O III] does not originate in the companion. Both emission peaks have high [O III]/Hβ likely from AGN, indicating that these objects may be outflows driven by AGN activity.

- *Three cases of unresolved small-scale structure.* J0940+3113, J1051+6251, and J1157+ 0816 have spatially coincident [O III] peaks within 0.″15. These unresolved peaks can be caused by complicated narrow line region kinematics, very close dual AGN or binary black holes, small-scale outflows or jets, rings of star formation, or gas disks. Higher resolution observations are needed to distinguish between these scenarios.

- *Two pairs of galaxies.* In J1108+0659, the spatial separations between the emission lines measured with integral field spectroscopy match the spatial separation of the two near-IR galaxies. The [Fe II]/Hβ ratios suggest that both galaxies are more likely dominated by star formation than AGN activity, although the SDSS spectra indicate there is at least one AGN in the system and Liu et al. (2013) find two X-ray AGNs. The spatial separation of the [O III] peaks in J1332+0606 match the separation between the main and companion galaxies; the [O III]/Hβ ratios indicate that both peaks could be due to AGN activity or star formation, so we

cannot prove the presence of two AGNs. At least one AGN is present in the galaxy pair (Liu et al., 2013).

- *One indeterminate candidate.* The second [O III] emission peak of J0725+3744 is unobservable due to sky line interference, excluding the measurement of a reliable peak separation for this object.

These results illustrate the importance of spatial resolution in determining the origins of the double [O III] emission lines. We conclude that double-peaked [O III] emission plus double spatial structure can be indicative of dual AGN, but also seems to occur in a number of other interesting scenarios. Although it may not be as effective at increasing our sample of dual AGN, studying double-peaked [O III] emitters with higher spatial resolution presents an excellent opportunity to study the complexity of gas kinematics around accreting black holes. Further observations, either with reoriented long-slits or with integral field spectrographs, are required to distinguish between the possible outflow and spatially unresolved emission peak cases.

Part III

X-ray Confirmation

Chapter 7

Chandra ACIS-S Confirmation of Candidate Dual AGNs

7.1 Introduction to X-Ray Confirmation

To confirm a potential dual AGN, either *Chandra* imaging, radio interferometry, or high spatial-resolution spectroscopy is needed to prove that each resolved source is independently an AGN. While spatially resolved spectroscopy has been used to confirm single objects as dual AGNs (described in Part II and McGurk et al., 2011, , among many others), there is still some doubt in the community that spatially resolved spectroscopy alone can confirm true dual AGNs (Comerford et al., 2015). Skeptics point out that even cases where two optical AGN emission components are observed to be coincident with two stellar bulges can be explained by a single AGN in one galaxy, or located between both galaxies, that has extended emission covering both (Moran et al.,

1992). X-ray observations are the gold standard of AGN confirmation, since high X-ray luminosities ($>10^{42}$ ergs s^{-1}) must originate from an actively accreting supermassive black hole.

The goal of X-ray confirmation is to prove that each spatially resolved component has a matching bright X-ray resolved nucleus. Breaking that down, we are looking for two spatially resolved X-ray nuclei that match the optical or near-IR components. This is clearly illustrated in Figure 7.1 for NGC 6240; the two nuclei present in the near-IR and optical imaging are matched by two X-ray nuclei. Furthermore, to unambiguously be AGNs, each nucleus must either have a 2-10 keV luminosity $>10^{42}$ ergs s^{-1}or, if under-luminous, limits must be placed on the contribution to the X-ray luminosity by star formation. Followup data, such as HST U-band images (Hopkins et al., 2003; Liu et al., 2013) or mid-infrared colors from the *Wide-Field Infrared Survey Explorer* (*WISE*; conversion described in Comerford et al., 2015), is needed to measure star formation rates and/or locations, to prove that the AGN dominates the measured X-ray luminosity.

The *Chandra X-ray Observatory* (Weisskopf et al., 1996) is the only X-ray telescope with the spatial resolution necessary to confirm true dual AGNs with separations of 1–3″. The Advanced CCD Imaging Spectrometer (ACIS; Garmire et al., 2003) has a plate scale of 0.″492 $pixel^{-1}$ and is sensitive to 0.5-10 keV, perfect for following up the double-peaked [O III] AGNs that have a possible companion AGN nearby.

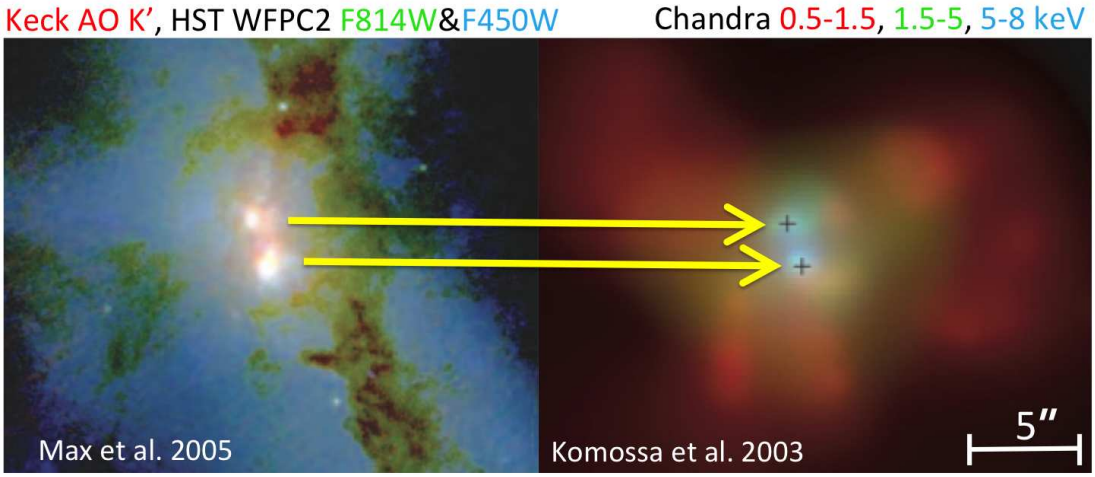

Figure 7.1: Imaging of the two AGNs in NGC 6240. North is up and east is left. The 5″ (2.35 kpc) scale bar applies to both images; the nuclei are separated by 1.″5 (700 pc). (**left**) Multiwavelength image from Max et al. (2005) displayed on a logarithmic scale. Red represents K'-band from Keck AO, green is the F814W filter from WFPC2 on *HST*, and blue is the F450W filter from WFPC2 on *HST*. The two nuclei are obvious next to the dust lanes. (**right**) Adaptively smoothed multicolor Chandra image, with red as 0.5–1.5 keV, green as 1.5–8 keV, and blue as 5–8 keV. The two nuclei are visible as two blue (hard) components.

7.2 Sample Selection for our Candidates

Of our 43 spatially double candidate dual AGNs, 9 have separations between the main galaxy and the companion of $\leq 0.7''$, too small for even *Chandra* to resolve. We constructed a sample of 34 candidate dual AGNs observable by *Chandra*. Of these 34 candidates, 8 candidates already had archival *Chandra* observations by various PIs. This left 26 well-separated candidates unobserved. In order to narrow down the list of candidates to observe, we measured the luminosity of each double [O III] peak from the candidates' SDSS spectroscopy. We then used the $L_{[OIII]}$ to $L_{2-10keV}$ relationship measured in Heckman et al. (2005) to convert the [O III] peak luminosities into X-ray luminosities.

Finally we used WebPIMMS, an online X-ray flux modeling tool, to convert our predicted hard 2-10 keV fluxes into 0.2-10 keV count rates; this helped predict which objects would be observable with *Chandra* ACIS-S. Each target was modeled as a point source with a power law spectrum with a photon index Γ of 1.8 and an absorbed average N_H of 10^{22} cm^{-2} (appropriate for a mildly obscured Type 2 AGN). We use the luminosity of the weaker peak for our count rate conversion and exposure calculations to ensure the detection of the faintest of both possible sources.

Around 50 counts are needed to measure a hardness ratio; our calculated observation times got 50 counts over 0.5–10 keV for each object based on their estimated count rates. Additionally, in case the estimated count rates are too high, our chosen observation times allowed a 10 count detection of a 10^{43} ergs s^{-1} AGN at all of the targets' various redshifts, providing a sample with a uniform depth. Exposure times ranged from 5 to 30 kilo seconds (1.4 to 8.3 hours). We were awarded 215 kiloseconds to observe the 12 brightest candidate dual AGNs with *Chandra* ACIS-S in *Chandra* Cycle 14 Proposal Number 14700787, Program GO3-14119X. Combining our observations with the 8 objects already observed gives us a total sample of 20 spatially double candidate dual AGNs. Observation details can be found in Table 7.1.

Of the 97 double-peaked [O III] AGNs that were spatially single in our near-IR imaging, 7 candidates have archival *Chandra* observations by various PIs. We can cautiously use these candidates as a comparison sample. Details of these observations can be found in Table 7.2.

In Section 7.3 we present imaging of the 27 double-peaked [O III] AGNs ob-

served with *Chandra*. As an example, in Section 7.4 we describe the quantitative analysis of one particular candidate, J1307+4604, that has obvious double spatial structure present in its X-ray observations. This analysis will repeated in full for the rest of the candidates over Summer 2015; as discussed in Section 7.5, a portion of the analysis is already completed.

Table 7.1: Chandra Observations of **Spatially Double** Double-peaked [O III] SDSS AGNs

SDSS Coordinates:	z	AGN Type	Companion Separation (″)	Companion Separation (kpc)	PA (°)	Exp. Time (ksec)	UT Observed (yymmdd)	Chandra Sequence Number	Chandra Obs. ID	Data Mode	PI Name
020011.52−093126.1	0.361	1	1.17	5.8	101	9.66	2012-11-01	702843	15036	VF	Max
						19.27	2012-11-04	702843	15577	VF	Max
081507.41+430427.0	0.510	1	1.95	12.0	252	8.17	2004-12-25	701118	5696	F	Vignali
091646.03+283526.7	0.142	2	1.23	3.1	358	5.00	2013-05-12	702833	15026	VF	Max
094032.25+311328.6	0.170	2	2.45	7.1	107	19.81	2013-01-13	702838	15031	VF	Max
095207.62+255257.2	0.339	1	1.00	4.8	182	19.81	2012-10-02	702674	13952	F	Comerford
105104.54+625159.3	0.436	1	1.52	8.6	68	9.95	2013-07-07	702834	15027	VF	Max
110851.04+065901.4	0.182	2	0.73	2.2	312	19.27	2011-02-10	702385	12749	F	Shen
114642.47+511029.6	0.130	2	2.84	6.6	34	15.43	2011-04-23	702387	12751	F	Shen
115106.69+471157.7	0.318	1	1.29	6.0	320	5.01	2013-05-20	702832	15025	VF	Max
115714.97+081632.0	0.201	2	2.61	8.6	207	29.67	2013-02-15	702842	15035	VF	Max
123915.40+531414.6	0.202	1	1.26	4.2	35	19.80	2013-01-13	702675	13953	F	Comerford
130128.76−005804.3	0.246	2	1.40	5.4	243	10.05	2006-05-28	701222	6804	F	Strauss
130724.08+460400.9	0.353	1	2.37	11.6	336	19.09	2013-08-08	702839	15032	VF	Max

Continued on next page

Table 7.1 – *Continued from previous page*

SDSS Coordinates:	z	AGN Type	Companion Separation (″)	Companion Separation (kpc)	PA (°)	Exp. Time (ksec)	UT Observed (yymmdd)	Chandra Sequence Number	Chandra Obs. ID	Data Mode	PI Name
133226.34+060627.3	0.207	2	1.58	5.4	12	23.95	2011-11-28	702388	12752	F	Shen
135024.66+240251.3	0.557	1	1.80	11.6	82	24.74	2013-05-01	702841	15034	VF	Max
135646.10+102609.0	0.123	2	1.32	2.9	185	19.80	2012-03-31	702673	13951	F	Comerford
150243.09+111557.3	0.390	1	1.47	7.8	107	9.66	2013-04-27	702835	15028	VF	Max
154107.81+203608.8	0.508	1	2.00	12.2	331	24.73	2012-12-15	702840	15033	VF	Max
161027.41+130806.8	0.229	1	2.35	8.6	294	14.87	2013-08-12	702836	15029	VF	Max
165206.15+310707.6	0.075	2	2.96	4.2	93	18.96	2012-12-18	702837	15030	VF	Max

Table 7.2: Chandra Observations of **Spatially Single** Double-peaked [O III] SDSS AGNs

SDSS Coordinates:	z	AGN Type	Exp. Time (ksec)	UT Observed (yymmdd)	Chandra Sequence Number	Chandra Obs. ID	Data Mode	PI Name
014209.01−005050.0	0.133	2	19.80	2012-09-16	702681	13959	F	Comerford
094124.02+394441.8	0.108	2	7.93	2008-01-16	701748	9308	VF	Harris
100654.20+464717.2	0.123	2	19.78	2013-01-14	702679	13957	F	Comerford
112659.54+294442.8	0.102	2	19.80	2012-02-17	702677	13955	F	Comerford
144804.17+182537.9	0.038	2	19.81	2012-12-05	702676	13954	F	Comerford
160436.21+500958.1	0.146	2	29.58	2011-12-02	702462	12827	F	Gerke
171544.02+600835.4	0.157	2	29.67	2011-03-17	702460	12825	F	Gerke

7.3 Data Reduction

All of our targets were observed on-axis with the ACIS S3 chip, 9 – 13″ away from the telescope aimpoint. We used the "timed exposure" mode and telemetered the data to the ground in "very faint" mode. We reprocessed the data using the standard *Chandra* Interactive Analysis of Observations (`CIAO`) software (Fruscione et al., 2006) with version 4.7. We ran the *Chandra* reprocessing script "`chandra_repro`" on the data files (called Level 2 event files) to apply the latest calibration files (CALDB 4.6.5) to correct for change transfer inefficiency and time-dependent gain. We also applied the energy-dependent sub pixel event repositioning (EDSER) algorithm (Li et al., 2004) to improve the image quality of ACIS-S data for sources near the optical axis of the telescope, where the point spread function (PSF) is undersampled by the 0.″5 ACIS pixels. Finally, our targets have low count rates (< 0.015 cts s^{-1} pix^{-1}), so pileup effects were insignificant (Ballet, 1999).

Figures 7.2–7.4 show the unsmoothed ACIS images of our 12 targets in the full (0.5–10 keV) X-ray band. Given the low count numbers (Table 7.4), we do not apply any smoothing to avoid artifacts. Overlaid on the X-ray images are the Keck NIRC2 *H* or *K'*-band images taken with LGS AO, custom scaled to best emphasize the substructure. Currently, the images are aligned by eye so that the center of the X-ray counts matches the center of the near-IR imaging; we will recalibrate the astrometric solutions for all the objects as described in Subsection 7.4.1 over the summer.

We detect the main AGN in 11 of our 12 objects. J0940+3113 has approximately 2 counts, so it does not count as a detection. J0200-0931, J1151+4711,

J1307+4604, and J1502+1115 have flux where the companion is located but also have flux scattered around the central AGN at other angles. For now, we presume that this flux at the companion's location originates from the companion; however, we need to perform full two-dimensional (2D) modeling of each component to separate the potential flux contribution from the companion. If a one component 2D model fits just as well as a two component 2D model, we will conclude that no X-ray companion is present.

Finally, we present the unsmoothed full band ACIS images of the 8 archival spatially double candidate dual AGNs in Figures 7.5–7.6 and the 7 archival spatially single candidate dual AGNs in Figures 7.7–7.8. The X-ray images are overlaid with custom-scaled contours either from the Keck NIRC2 *H* or *K'*-band images taken with LGS AO or from *HST* WFPC2 images. Again, these images are currently aligned by eye; the astrometric solutions will be recalculated over the summer. This realignment will allow us to investigate Comerford et al. (2015)'s conclusion that some of the X-ray sources are offset from their stellar bulges.

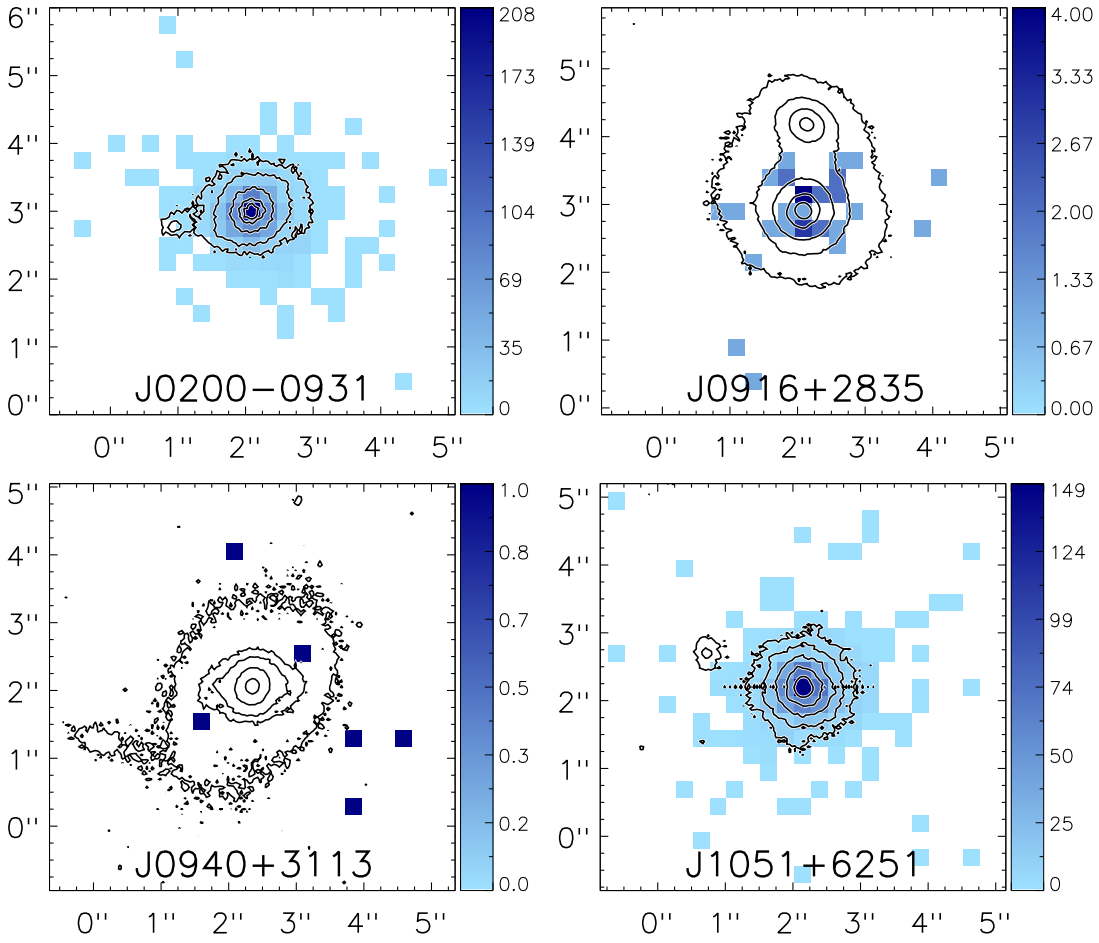

Figure 7.2: Chandra ACIS-S X-ray images (0.″25 pixel^{-1} binning, unsmoothed) of our 12 double-peaked [O III] **spatially double** candidate dual AGNs in this Figure and Figures 7.3–7.4. Each 6″×6″ image displays the 0.5-10 keV total counts with maximum values indicated on the right scale bars. The contours are Keck NIRC2 H and K′ images taken with Laser Guide Star Adaptive Optics and custom scaled to best display the substructure. North is up and East is left. J0200-0931 has X-ray flux where the near-IR companion is located, but also has X-ray flux scattered around the central AGN at other angles. 2D modeling is needed to determine if a second AGN is present in the system and responsible for the local X-ray flux.

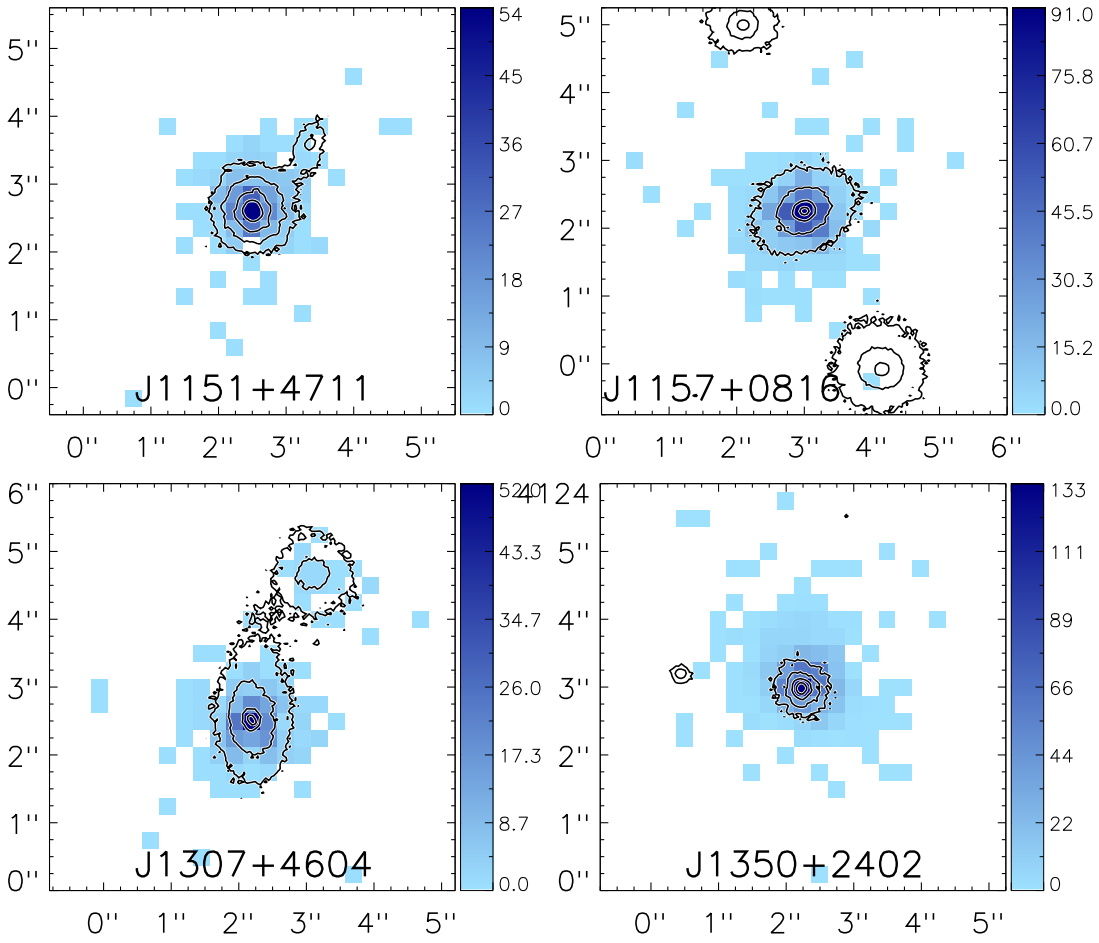

Figure 7.3: Continued. Chandra ACIS-S X-ray images (0.″25 pixel^{-1} binning, unsmoothed) of our 12 double-peaked [O III] **spatially double** candidate dual AGNs in this Figure and Figures 7.3–7.4. Each 6″×6″ image displays the 0.5-10 keV total counts with maximum values indicated on the right scale bars. The contours are Keck NIRC2 H and K′ images taken with Laser Guide Star Adaptive Optics and custom scaled to best display the substructure. North is up and East is left. J1151+4711 and J1307+4604 have X-ray flux where the near-IR companion is located, but also have flux scattered around the central AGN at other angles. 2D modeling is needed to determine if a second AGN is present in the systems and responsible for the local X-ray flux.

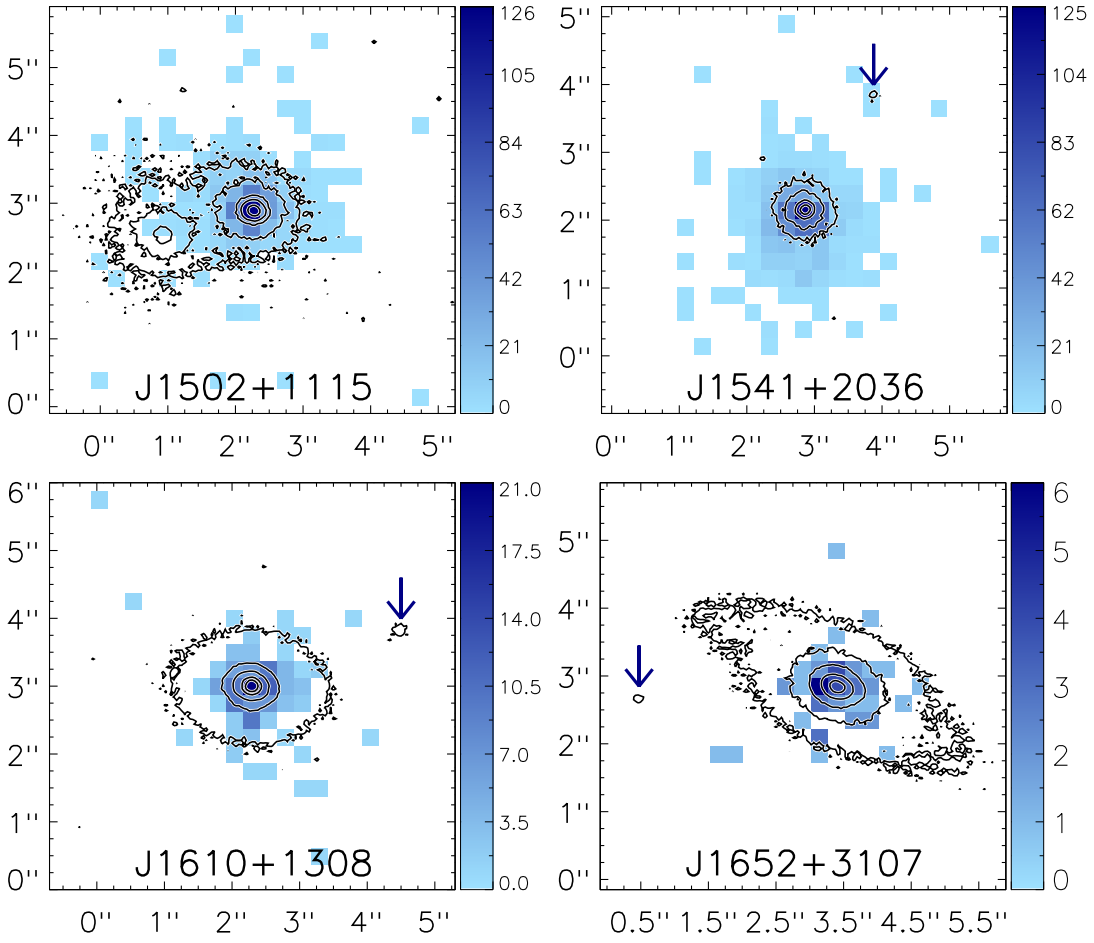

Figure 7.4: Continued. Chandra ACIS-S X-ray images (0.″25 pixel^{-1} binning, unsmoothed) of our 12 double-peaked [O III] **spatially double** candidate dual AGNs in this Figure and Figures 7.2–7.3. Each 6″×6″ image displays the 0.5-10 keV total counts with maximum values indicated on the right scale bars. The contours are Keck NIRC2 H and K′ images taken with Laser Guide Star Adaptive Optics and custom scaled to best display the substructure. The blue arrow indicates the near-IR companion if it is very faint and easily overlooked. North is up and East is left. J1502+1115 has X-ray flux where the near-IR companion is located, but also have flux scattered around the central AGN at other angles. 2D modeling is needed to determine if a second AGN is present in the system and responsible for the local X-ray flux.

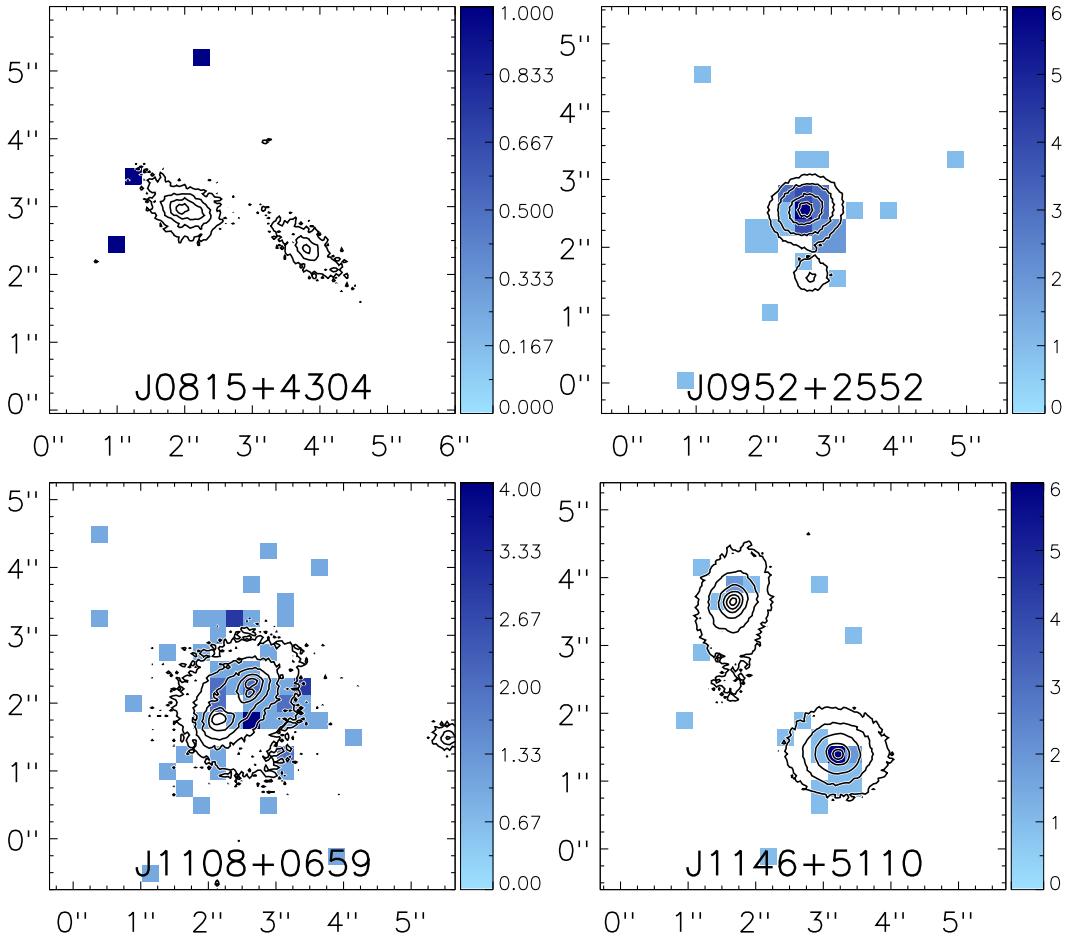

Figure 7.5: **Archival** Chandra ACIS-S X-ray images (0.″25 pixel^{-1} binning, unsmoothed) of 8 double-peaked [O III] **spatially double** candidate dual AGNs in this Figure and Figure 7.6. Each 6″×6″ image displays the 0.5-10 keV total counts with maximum values indicated on the right scale bars. The contours are Keck NIRC2 H and K′ images taken with Laser Guide Star Adaptive Optics or HST WFPC2 and custom scaled to best display the substructure. North is up and East is left. J0952+2552, J1108+0659, J1146+5110, and J1239+5314 have X-ray flux where the near-IR companion is located, but also have flux scattered around the central AGN at other angles. 2D modeling is needed to determine if a second AGN is present in the systems and responsible for the local X-ray flux.

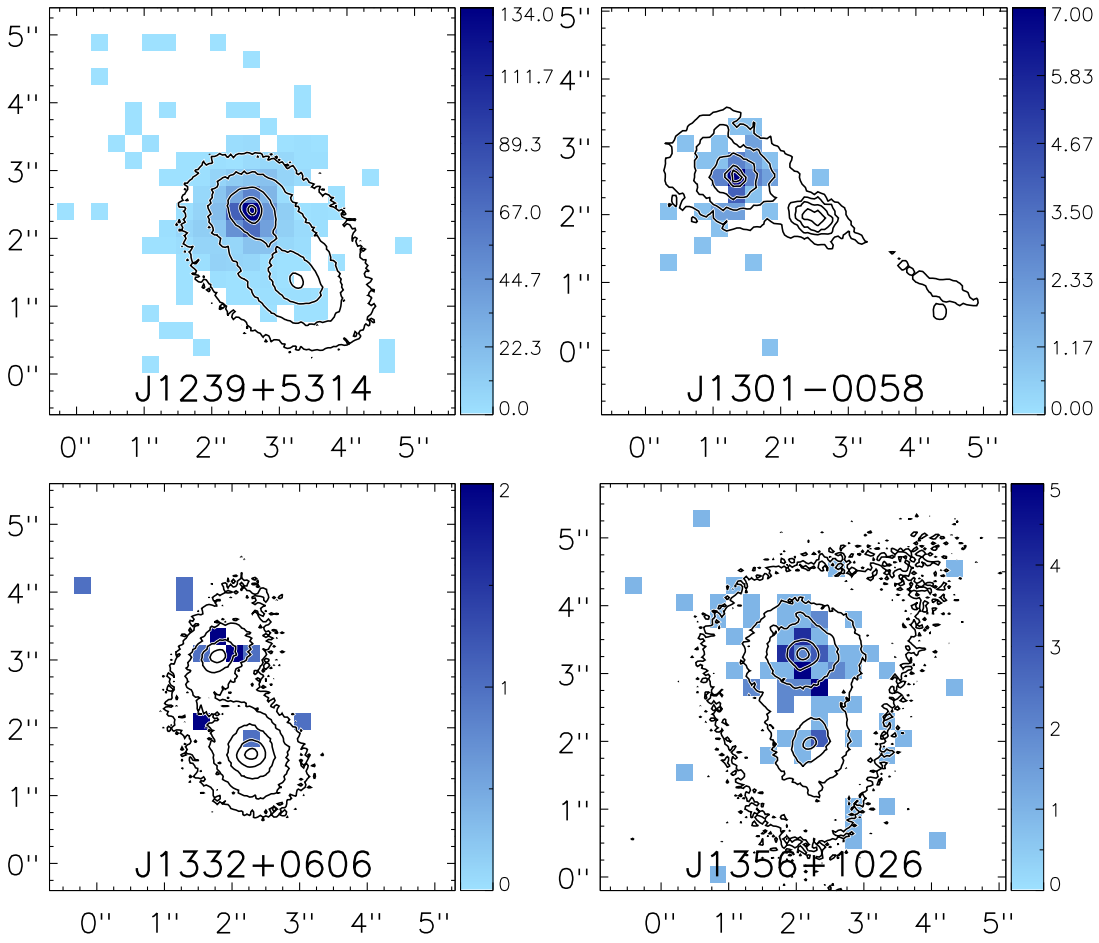

Figure 7.6: Continued. **Archival** Chandra ACIS-S X-ray images ($0\farcs25$ pixel^{-1} binning, unsmoothed) of 8 double-peaked [O III] **spatially double** candidate dual AGNs in this Figure and Figure 7.5. Each $6''\times6''$ image displays the 0.5-10 keV total counts with maximum values indicated on the right scale bars. The contours are Keck NIRC2 H and K′ images taken with Laser Guide Star Adaptive Optics or HST WFPC2 and custom scaled to best display the substructure. North is up and East is left. J1356+1026 has X-ray flux where the near-IR companion is located, but also have flux scattered around the central AGN at other angles. 2D modeling is needed to determine if a second AGN is present in this system and responsible for the local X-ray flux.

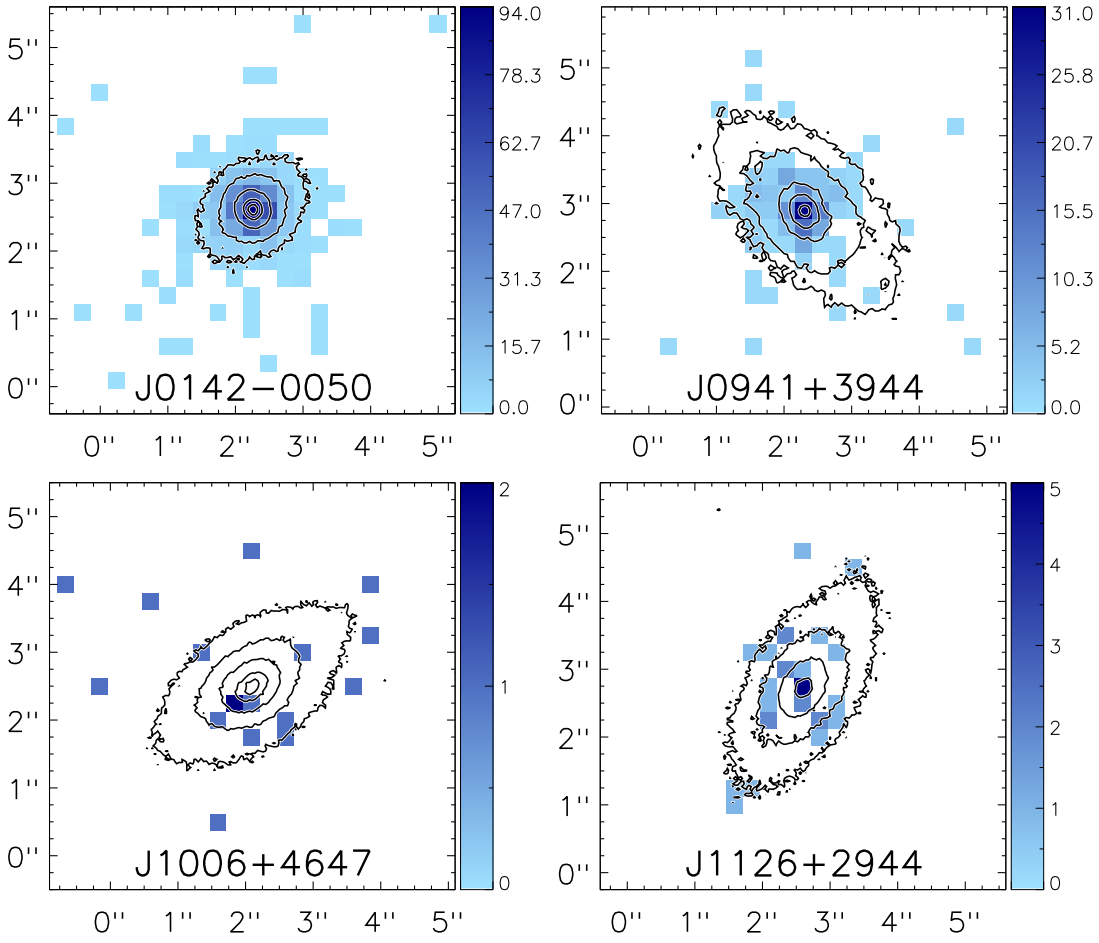

Figure 7.7: **Archival** Chandra ACIS-S X-ray images ($0\farcs25$ pixel^{-1} binning, unsmoothed) of 7 double-peaked [O III] **spatially single** candidate dual AGNs in this Figure and Figure 7.8. Each $6''\times6''$ image displays the 0.5-10 keV total counts with maximum values indicated on the right scale bars. The contours are Keck NIRC2 H and K′ images taken with Laser Guide Star Adaptive Optics or HST WFPC2 images and custom scaled to best display the substructure. North is up and East is left.

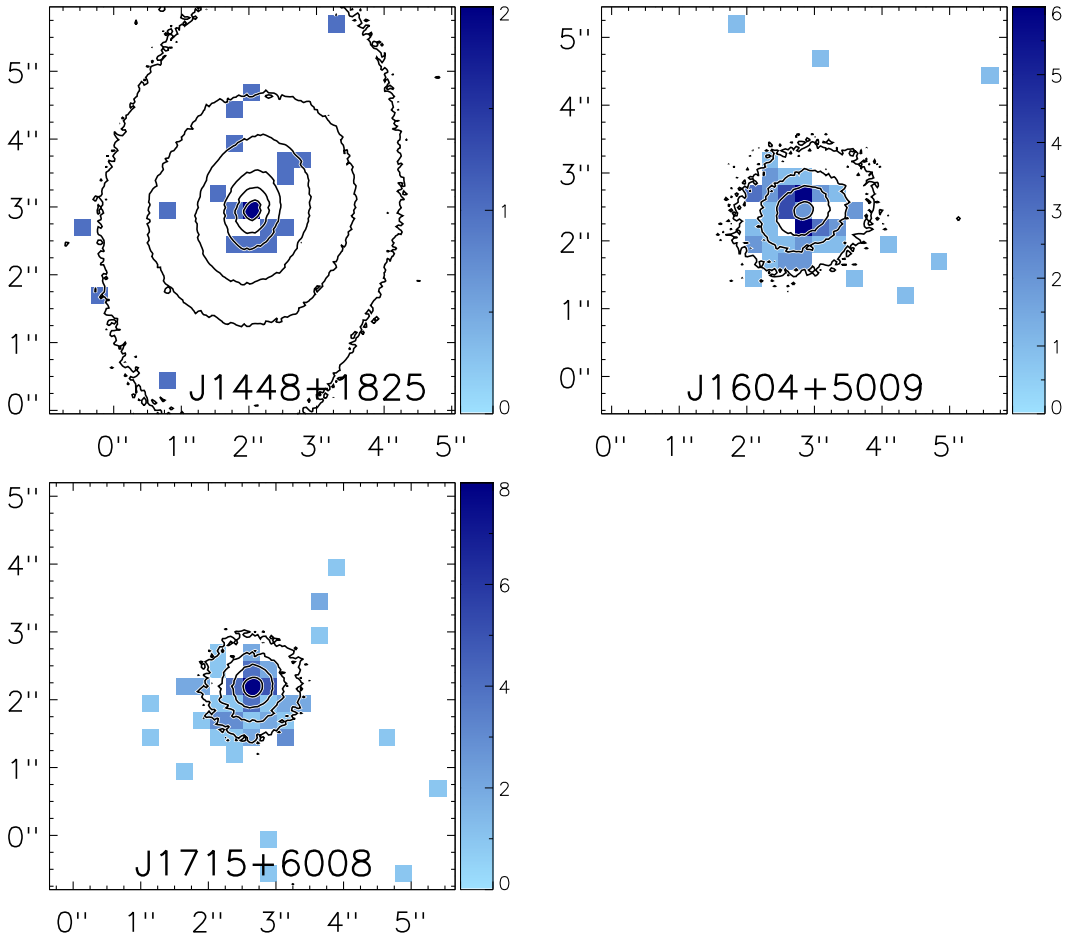

Figure 7.8: Continued. **Archival** Chandra ACIS-S X-ray images ($0\farcs25$ pixel^{-1} binning, unsmoothed) of 7 double-peaked [O III] **spatially single** candidate dual AGNs in this Figure and Figure 7.7. Each $6''\times6''$ image displays the 0.5-10 keV total counts with maximum values indicated on the right scale bars. The contours are Keck NIRC2 H and K$'$ images taken with Laser Guide Star Adaptive Optics or HST WFPC2 images and custom scaled to best display the substructure. North is up and East is left.

7.4 Analysis and Modeling

In this Section we describe the analysis and modeling of one particular candidate, SDSS J130724.08+460400.9 (hereafter abbreviated J1307+4604). This particular candidate dual AGN has obvious spatial structure present in its X-ray observations.

The goals of the analysis and modeling are to measure:

1. **$L_{2-10keV}$ of each AGN** — We will measure the 2-10 keV luminosity for each spatially-separated point-like component of our targets. By detecting spatially separated components that have luminosities $> 10^{42}$ ergs s^{-1}, we will determine if each component is an AGN or a clump of either star formation or X-ray binaries.

2. **Spatial concentration of the X-rays similar to NIRC2 imaging** — Many previously confirmed dual AGNs, such as NGC 6240 (Komossa et al., 2003) and Mrk 739 (Koss et al., 2011b), show distinct X-ray point sources matching the observed optical or infrared spatial double structure, such as SDSS J1307+4604 in Figure 7.9. We plan to compare our X-ray data to a model of two point sources convolved with *Chandra*'s PSF and with their positions constrained by the existing high-resolution NIRC2 data.

3. **Hardness Ratio and Column Density** — From their $L_{2-10keV}$ and hardness ratio, the objects will be classified as AGNs or star-forming galaxies via Figure 7.13. The hardness ratio is essentially an estimate of the target's spectral slope using the soft (0.2-2 keV) and hard (2-10 keV) X-ray bands. If an object is very hard, it is either an AGN emitting more strongly in hard X-rays or an obscured

AGN with a spectrum that was originally more powerful in the soft band but is preferentially extincted in the soft bands, leaving a harder spectrum behind. The hardness ratio will help us determine if the target is an AGN. Additionally, using the AGNs' hardness ratios and by assuming a spectrum with a simple power law with a range of slopes, we will estimate the N_H column densities.

7.4.1 Astrometric Uncertainty of ACIS Images

For the Liu et al. (2013) and Comerford et al. (2015) studies that have both *HST* and *Chandra* observations, refined astrometry of the *Chandra* observations is extremely important to successfully compare with their *HST* observations. While we will polish the astrometric solutions of our *Chandra* observations, it is often impossible to fit WCS coordinates to our Keck NIRC2 images due to the paucity of sources in our extremely small field of view (40-50″ on a side). To compound this challenge, often the main SDSS object cannot be used as an astrometric calibrator since the SDSS coordinates could be centered on either spatial component or in between them. Regardless, if there are three or more sources surrounding our target, we will use `IRAF` to fit WCS coordinates to the NIRC2 images to aid in our comparisons. Astrometric calibrations are necessary to place realistic error constraints on the positions of both the X-ray and near-IR sources detected.

The typical absolute ACIS-S astrometric accuracy within 3 arcmin of the aimpoint is $\lesssim 0\farcs8$ (radius of the 99% uncertainty circle of ACIS-S absolute position[19];

[19] `http://cxc.harvard.edu/cal/ASPECT/celmon/`

Chandra Proposers' Observatory Guide,[20] hereafter POG). The 90%-limit relative astrometric accuracy is $0\farcs15$ for on-axis sources such as ours. Astrometric calibrations are applied as part of the normal *Chandra* ACIS image processing pipeline. Regardless, we will verify the astrometric accuracy using CIAO's `wavdetect` (Freeman et al., 2002); this algorithm performs wavelet-based spatial analysis of Poisson data to detect sources as references for fine astrometric alignment. We will input observation-specific PSF map files, created with `mkpsfmap`, instead of using the general PSF table. Additionally, we will adopt a high-significance threshold (`sigthresh`$= 10^{-8}$, meaning one false detection in a $10^4 \times 10^4$ pixel map) to ensure the detection of real sources. We will use Source Extractor (Bertin & Arnouts, 1996) with a 3σ detection threshold on SDSS images of the *Chandra* field of view to detect possible matches to our X-ray detected sources. Once the matched sources are identified and offsets are measured, we will get the final astrometric correction by taking the error-weighted average of the offsets measured.

7.4.2 2-Dimensional Modeling to Detect Companions

As shown in Figure 7.9, J1307+4604 has X-ray counts where the near-IR companion is located. We need to determine that this flux originates from the companion, and not from the broad wings of the main AGN. Two-dimensional (2D) modeling of the system with one and two components will help to separate the potential flux contribution from the companion. If a two component 2D model fits better than a one component 2D model, we will conclude that an X-ray companion is present. Modeling will also give us the flux of both spatial components.

[20] `http://cxc.harvard.edu/proposer/POG/`

We measured the X-ray positions of the various components by performing 2D image fitting using `Sherpa` version 4.4, `CIAO`'s modeling and fitting package (Freeman et al., 2001). `Sherpa` enables us to construct complex models with simple parameters and to fit those models to data. We rebin our J1307+4604 data so that our pixels are $0\farcs296$ in size (half the size of the detector pixels) and exclude photons outside of the 0.2–10 keV energy range as they are likely to be background. We set the "`fit`" routine to use the Nelder & Mead (1965) optimization method ("`simplex`") and modified Cash (1979) statistics ("`cstat`"), since these techniques are best suited to handling low numbers of counts. The initial parameters for each 2D X-ray model contain two or three components with separations and orientations on the sky to match the spatial components observed in our NIRC2 images, as well as a constant background value.

There are several types of models that can be used in our 2D fitting:

1. Most simple is a 2D beta model (`beta2d`), which is a 2D Lorentzian profile with a varying power law of the form $I(r) = A(1 + (r/r_0)^2)^{-\alpha}$. In general, beta models are a good match to the Chandra PSF. While Comerford et al. (2015) tied the power law index α to the r_0 parameter and required the two fit components to have the same r_0, these constraints did not work for our tests on J1307+4604. We allowed the components positions, amplitudes, r_0, and power law index α to be free parameters. Figure 7.10 shows our data, fitted model, and residuals for our best fit of J1307+4604. Out of the models tested on J1307+4604, the 2D beta models achieved the best fit to our data.

2. We can use PSF images as convolution kernels to fit the sources. PSF images can

be created through a complex process with the `MARX` software[21] using the PSF-ray table generated by the *Chandra* Ray Tracer (ChaRT; Carter et al. 2003), which simulates the PSF at any off-axis angle and for any energy or spectrum. In our test case, we created and used a 1.0 keV PSF at the position of the main AGN in J1307+4604. However, since the *Chandra* PSF is energy dependent, we will need to extract the spectrum from each AGN and weight a range of PSFs created at different energies based on the spectra of our objects to create a more realistic PSF to convolve. We also have choices for the model to convolve with our PSF:

(i) We can convolve our PSF with a Gaussian model (`gauss2d`). This reduces the number of fit parameters and simplifies the fit. Unfortunately, this model does not fit well for J1307+4604, as shown in Figure 7.11. The 1.0 keV PSF convolved with the Gaussian models fails to fit the central peak value.

(ii) We can also conceptually convolve our PSF with a delta function model (`delta2d`), which might be a more physically motivated scenario. This would simplify our fitting further, as the only free parameters would be the components' positions and amplitudes. However, this model crashed as we tested it, so a final fit was not achieved; the *Chandra* Helpdesk is being consulted.

While the PSF model was expected better fit the data, the 2D beta models perform much better in fitting our J1307+4604 data (PSF models in Figure 7.11 vs. 2D beta models in Figure 7.10), so we will be using 2D beta models for the rest of our 2D modeling unless using an energy weighted PSF improves the fit for J1307+4604.

[21] `http://space.mit.edu/ASC/MARX/index.html`

During our fitting of J1307+4604, we noticed that the final fitted model was extremely dependent on the input parameters. To properly sample the fit parameter space, we will use a Monte Carlo optimization method to further explore the parameter space; both techniques are supported in `Sherpa` and will be tested in the Summer of 2015.

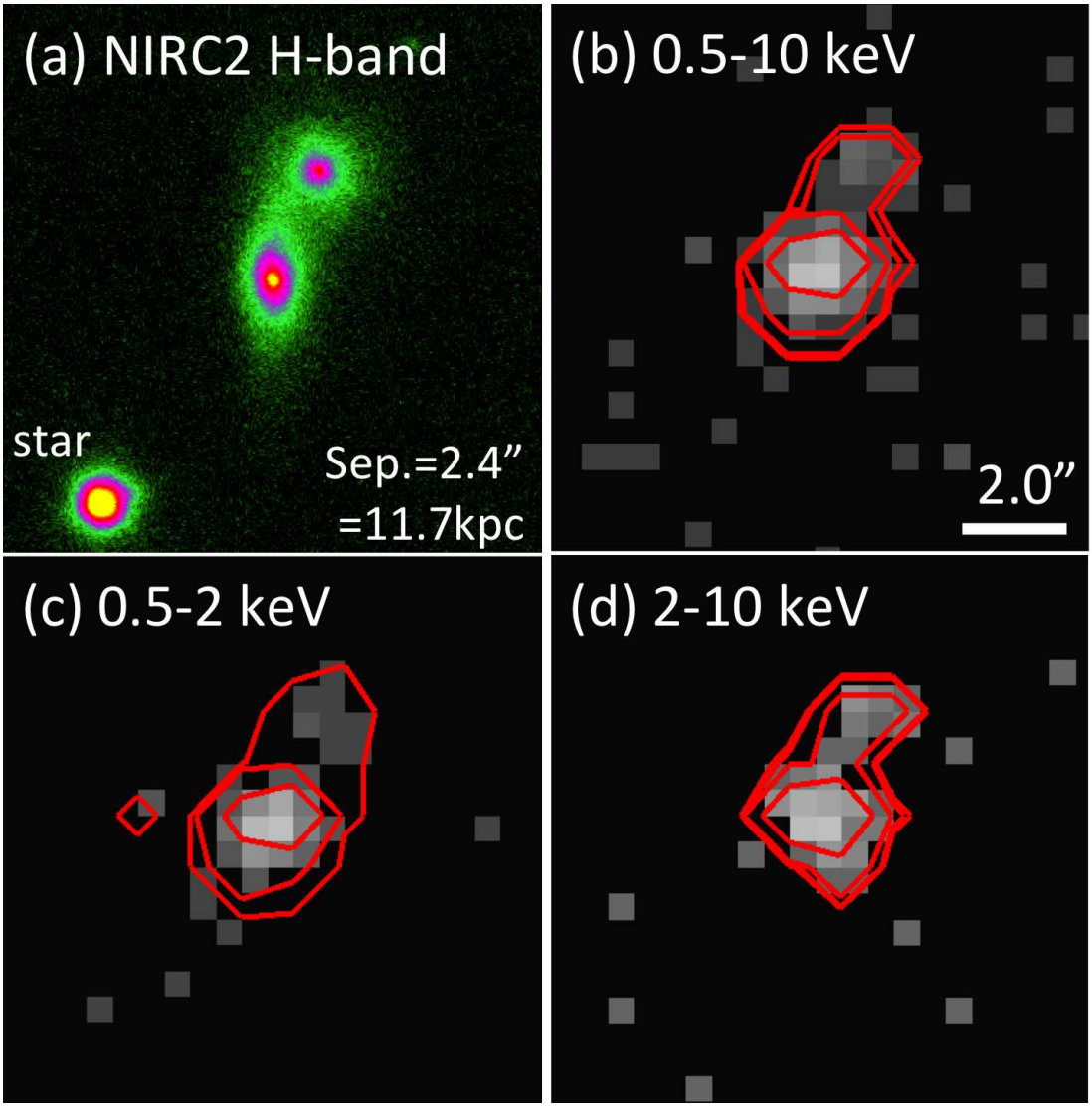

Figure 7.9: Comparison of our Keck II LGS AO H-band image (**a**) with our Chandra ACIS-S images (**b-d**) of SDSS J1307+4604. All images are $10'' \times 10''$, displayed with a log scale. (**a**) Keck LGS AO NIRC2 H-band image. We note the NW Chandra object **(b)** is in the direction and at the separation of the companion seen in this image. The three Chandra images are displayed on the same color scale, and show the following energy ranges: (**b**) 0.5-10keV; (**c**) 0.5-2keV, or soft; and (**d**) 2-10keV, or hard. Linear red contours created from the 0.5-10keV image are overplotted on (**b**)-(**d**). Note that the NW Chandra object contains more hard X-ray flux than soft. The flux from both galaxies is greater than 10^{42} ergs s^{-1}, proving that this object is a dual AGN.

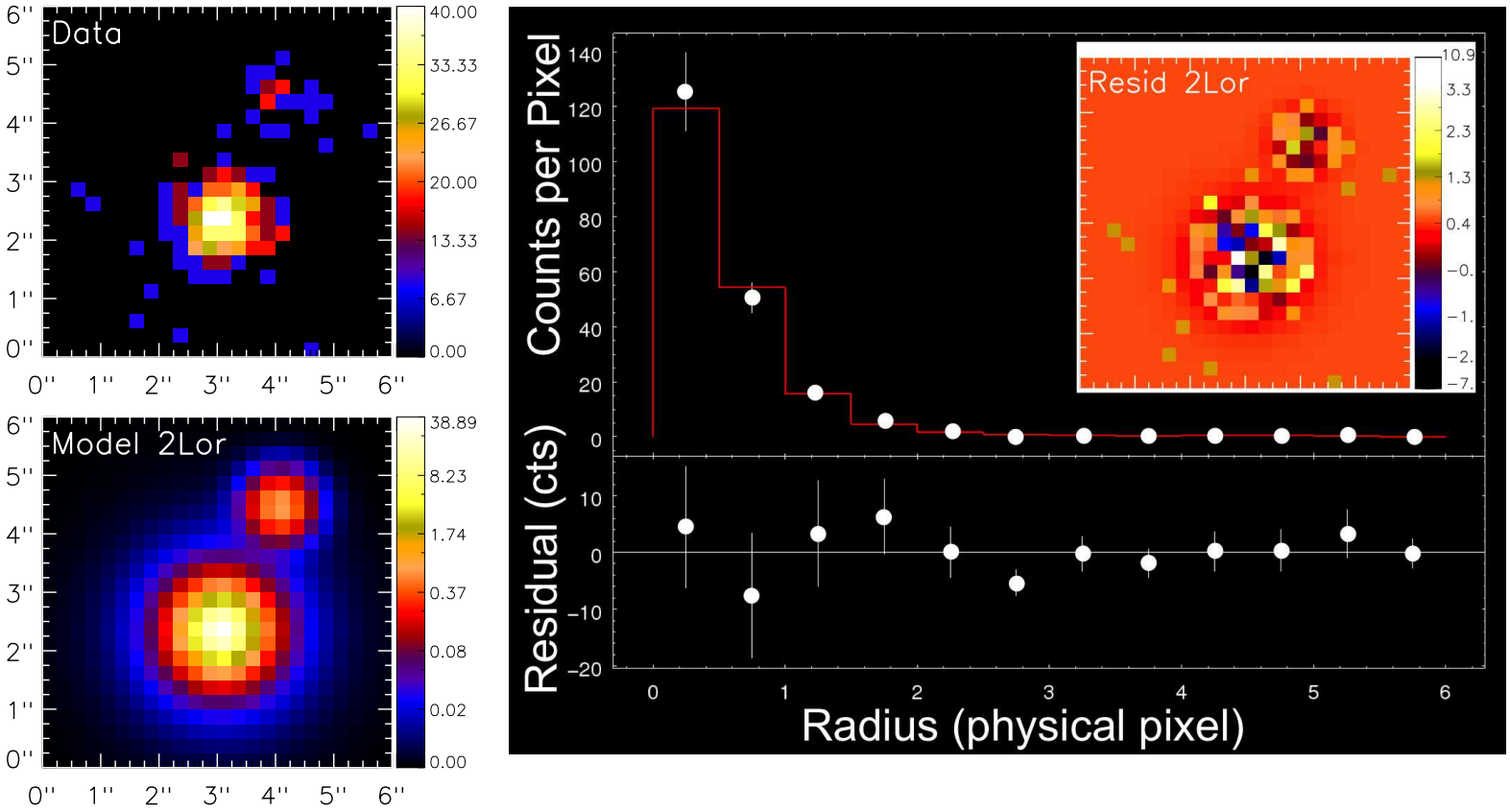

Figure 7.10: First model and residuals of the Chandra ACIS-S X-ray observation of J1307+4604 using two Beta (Lorentzian) profiles. Log-scaled images of the data (**top left**), 2-D model (**bottom left**) and the residual (data – model) (**upper right inset**) are shown with 0.″25 pixel^{-1} binning. Each 6″×6″ image displays the 0.5-10 keV total counts with maximum values indicated on the right scale bars. The **top right** panel plots the radial profile of the data (white circles) and the fitted model (red line), and the **bottom right** panel plots the residuals as white points around the zero line. The Lorentzian profiles seem to well fit our on-axis Chandra data.

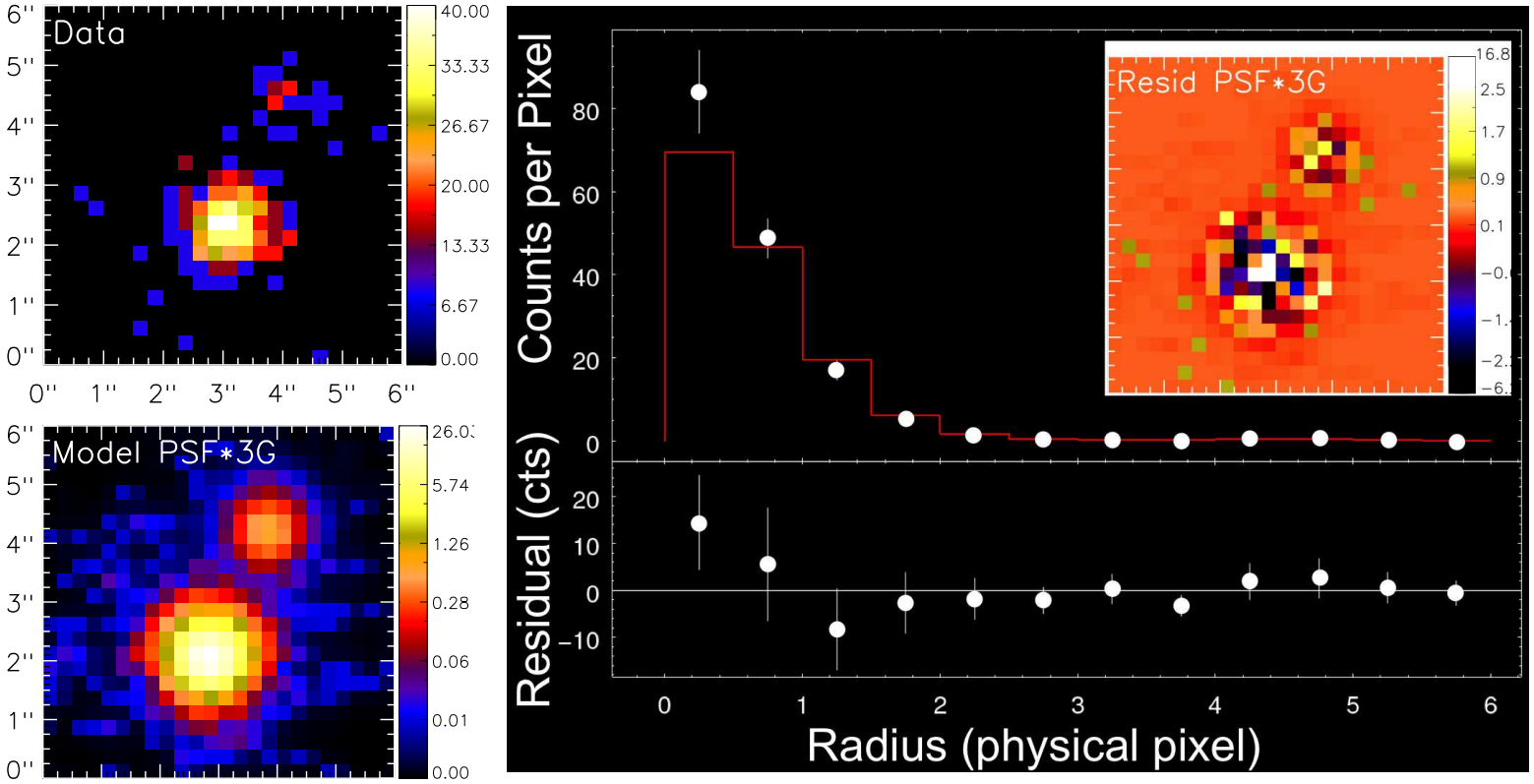

Figure 7.11: Second model and residuals of the Chandra ACIS-S X-ray observation of J1307+4604 using three Gaussian profiles convolved with the 1 keV Chandra ACIS-s Point Spread Function (PSF) generated using ChaRT and MARX. As described in Figure 7.10, log-scaled images of the data (**top led**), 2-D model (**bottom left**) and the residual (**upper right inset**) are shown. The **top right** panel plots the radial profile of the data (white circles) and the model (red line), and the **bottom right** plot shows the residuals. Convolving the Gaussians with the 1 keV PSF does not seem to fit as well as the Lorentzian fits. This suggests that further modeling should be done with PSFs of different energies and/or a different underlying model (e.g. a delta function).

7.4.3 Source Extraction to Measure Total Counts, Fluxes, and Luminosities

We run "`srcflux`" to extract X-ray net counts, photon fluxes, and energy fluxes for both nuclei. We use the positions from the 2D modeling as priors for the source extraction. The background counts were extracted from source-free regions around the target regions. We extracted the flux in separate soft (0.5–2 keV) and hard (2–10 keV) bands as well as the full band (0.5–10 keV). The radii of the source regions were chosen to be half the predicted separation of the objects, to ensure no overlap and double counting. To ensure that no flux was missed, we used "`quick`" PSF method, which applies an aperture correction to the count rate and flux estimates. Using a distance of 1900 Mpc (from the NASA/IPAC Extragalactic Database), we convert the fluxes into soft, hard, and total luminosities. All of these measured quantities are shown in Table 7.3. We plan to compare the fluxes calculated from our 2D modeling to the "`srcflux`" fluxes extracted over the Summer.

Table 7.3: X-ray Count Rates, Fluxes, and Luminosities

	Total Counts		Flux			Luminosity		
	Soft	Hard	Soft	Hard		Soft	Hard	Total
Obj. Component	cts		10^{-16} erg/s/cm^2		HR	10^{42} erg/s		
1307+4604 main	231^{+13}_{-13}	84^{+8}_{-8}	566^{+33}_{-33}	697^{+70}_{-70}	0.10	24.5	30	55
1307+4604 comp	<5	7^{+4}_{-3}	<12.3	$57.2^{+28.9}_{-20.7}$	>0.65	<0.53	2.5	<3.0

7.4.4 X-Ray Hardness Ratio and Spectral Analysis

We can estimate parameters of X-ray spectral models using the hardness ratio (HR) as a proxy for more complex spectral fitting. The hardness ratio is defined as

$$\mathrm{HR} = \frac{H - S}{H + S} \tag{7.1}$$

where H and S are the number of counts in the hard (2–10 keV) and soft (0.5–2.0 keV) bands, respectively. We estimate our hardness ratios and their uncertainties using the Bayesian techniques developed by Park et al. (2006). Figure 7.12 plots the HR and $L_{0.5-10keV}$ for both components of J1307+4604. Luminosities above 10^{42} ergs s^{-1} and hardness ratios above -0.2 indicate that both the main galaxy and the companion galaxy are AGN, confirming J1307+4604 as a dual AGN.

The photon index Γ can be estimated by assuming a simple power-law model $n(E) \propto E^{-\Gamma}$; for this simple model, we will include absorption by the Galactic column density calculated using the `CIAO` observing toolkit[22] based on the neural hydrogen data set of Dickey & Lockman (1990). We can also estimate the object's intrinsic galactic column density by fixing the photon index Γ to 1.8, a typical value for low redshift unobscured Seyferts (e.g., Nandra & Pounds, 1994; Green et al., 2009). We want to measure the column density in order to measure how much gas each nucleus contains. Obvious caveats for this method are that it is unlikely that the single absorbed power-law model will fully describe obscured AGNs with thermal emission from starburst components and scattered nuclear emission, nor will our estimates of intrinsic column

[22] `http://asc.harvard.edu/toolkit/colden.jsp`

density reflect the real values in cases of patchily obscured or Compton thick ($N_H \sim 10^{24}$ cm^{-1} or larger) AGNs. Unfortunately the low counts of our detections prevent the testing of more realistic models.

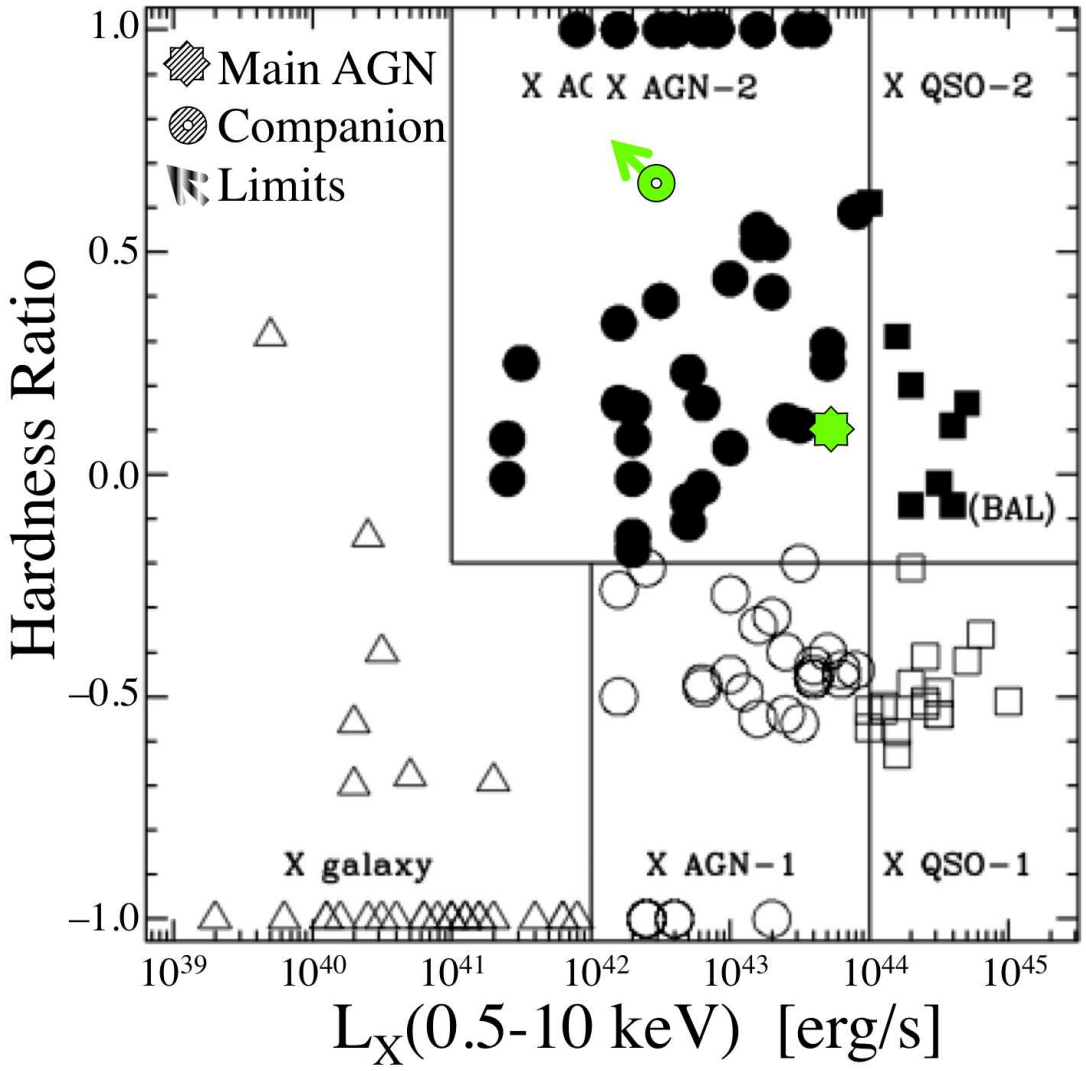

Figure 7.12: Hardness ratio vs. observed X-ray luminosity in the 0.5-10 keV band (Szokoly et al., 2004) with our main and companion AGNs observed by *Chandra* overplotted as green points. The main AGN is represented as a solid spiky circle and the companion is represented as an annulus. The arrow on the companion indicates that the companion's soft X-ray luminosity was an 90% confidence upper limit measurement. Luminosities above 10^{42} ergs s^{-1} and hardness ratios above -0.2 indicate that both the main galaxy and the companion galaxy are AGN, confirming J1307+4604 as a dual AGN.

7.5 Modeling Techniques and Incomplete Analysis of Additional Candidates

The steps above describe our analysis of one particular object that has strong X-ray double spatial structure to match the near-IR companion. We will perform a similar analysis for all 27 candidates over the Summer of 2015, with some variations to the analysis steps based on the X-ray flux of possible companions.

We will perform astrometric corrections and 2D modeling as described for J1307+4604. We plan to use primarily 2D beta functions (2D Lorentzians), although we will test energy-weighted PSFs convolved with both 2D Gaussians and 2D delta functions for two or three objects.

7.5.1 Source Extraction for Counts, Fluxes, and Luminosities

Our primary technique for extracting X-ray counts and fluxes will be the same routine as described for J1307+4604 in Section 7.4.3. We have preliminary extractions completed for our 12 original objects; all of these measured quantities are shown in Table 7.4, with luminosities calculated from the distance of each object reported in the NASA/IPAC Extragalactic Database. For this fast extraction we applied the "`quick`" PSF method for the aperture correction. For future extractions of all 27 objects, we plan to use the energy-weighted PSFs created during the 2D modeling as the inputs to calculate the appropriate aperture corrections.

For sources with truly marginal detections of the companion, there is a technique that may boost our signal-to-noise. Following the methods of Civano et al. (2012)

and Liu et al. (2013), we can bin the data along the axis of separation and perform one-dimensional (1D) fits of the components. There are too few counts to do 1D analysis in J0940+3113 and J1131−0204. We can project a grid of $0\farcs5 \times 2\farcs0$ regions along the line linking the main galaxy and companion nuclei. While there could be emission from an extended source, such as in J1108+0659 and J1356+1056 (Liu et al. 2013 and Comerford et al. 2015, respectively), we will assume that the emission originates from a combination of point sources and fit accordingly. We will project the same region grid over the appropriate 2D Lorentzian or PSF models and compare the extracted 1D model profiles with the 1D source profiles. We will perform fitting in `Sherpa` using modified Cash statistics to test one-component and two-component PSF models to test if there is a companion. This 1D extraction and fitting can also be done with the soft and hard bands if there are enough source photons. If the two sources have different spectral properties, this will lend further support to the two-component scenario.

Table 7.4: X-ray Counts, Fluxes, and Luminosities

SDSS Coordinates	Component	Total Counts Soft (cts)	Total Counts Hard (cts)	Flux Soft (10^{-16} erg/s/cm^2)	Flux Hard (10^{-16} erg/s/cm^2)	HR	Luminosity Soft (10^{42} erg/s)	Luminosity Hard (10^{42} erg/s)	Luminosity Total (10^{42} erg/s)
020011.52−093126.1	main	890^{+26}_{-26}	349^{+17}_{-16}	2140^{+65}_{-60}	3350^{+160}_{-165}	0.22	97	153	250
020011.52−093126.1	comp	41^{+8}_{-7}	25^{+6}_{-5}	95.5^{+20}_{-17}	232^{+59}_{-49}	0.42	4.3	11	15
091646.03+283526.7	main	18^{+4}_{-3}	13^{+4}_{-3}	148^{+35}_{-27}	586^{+178}_{-128}	0.60	0.82	3.2	4.1
091646.03+283526.7	comp	0^{+2}_{-0}	<3	7.25^{+47}_{-4}	<112	<0.88	0.040	<0.62	<0.7
094032.25+311328.6	main	$1^{+2}_{-0.5}$	<3	$3.30^{+5.70}_{-1.65}$	<28.2	<0.79	0.027	<0.23	<0.26
094032.25+311328.6	comp	<3	<3	<6.19	<28.2		<0.051	<0.23	<0.28
105104.54+625159.3	main	679^{+23}_{-23}	247^{+14}_{-14}	3360^{+115}_{-110}	5020^{+290}_{-290}	0.20	239	357	597
105104.54+625159.3	comp	305^{+16}_{-16}	113^{+10}_{-10}	1530^{+80}_{-80}	2640^{+235}_{-230}	0.27	109	188	297

Continued on next page

Table 7.4 – *Continued from previous page*

SDSS Coordinates	Component	Total Counts Soft (cts)	Total Counts Hard (cts)	Flux Soft (10^{-16} erg/s/cm^2)	Flux Hard (10^{-16} erg/s/cm^2)	HR	Luminosity Soft (10^{42} erg/s)	Luminosity Hard (10^{42} erg/s)	Luminosity Total (10^{42} erg/s)
115106.69+471157.7	main	233^{+13}_{-13}	113^{+10}_{-10}	2270^{+130}_{-130}	5230^{+445}_{-445}	0.39	77	177	254
115106.69+471157.7	comp	26^{+6}_{-5}	19^{+5}_{-4}	222^{+49}_{-40}	491^{+130}_{-102}	0.38	7.5	17	24
115714.97+081632.0	main	504^{+21}_{-19}	184^{+12}_{-12}	814^{+32}_{-32}	1220^{+80}_{-80}	0.20	9.7	15	24
115714.97+081632.0	c1	<3	<3	<4.33	<18.9		<0.052	<0.22	<0.28
115714.97+081632.0	c2	<259	<3	<4.15	<21.1		<0.052	<0.22	<0.28
130724.08+460400.9	main	231^{+13}_{-13}	84^{+8}_{-8}	566^{+33}_{-33}	697^{+70}_{-70}	0.10	24.5	30	55
130724.08+460400.9	comp	<5	7^{+4}_{-3}	<12.3	$57.2^{+28.9}_{-20.7}$	>0.65	<0.53	2.5	<3.0
135024.66+240251.3	main	599^{+21}_{-21}	270^{+16}_{-14}	1140^{+40}_{-40}	2760^{+150}_{-155}	0.42	146	354	500
135024.66+240251.3	comp	<4	<3	<7.19	<27		<0.92	<3.5	<4.4

Continued on next page

Table 7.4 – *Continued from previous page*

SDSS Coordinates	Component	Total Counts Soft (cts)	Total Counts Hard (cts)	Flux Soft (10^{-16} erg/s/cm^2)	Flux Hard (10^{-16} erg/s/cm^2)	HR	Luminosity Soft (10^{42} erg/s)	Luminosity Hard (10^{42} erg/s)	Luminosity Total (10^{42} erg/s)
150243.09+111557.3	main	469^{+19}_{-19}	264^{+15}_{-14}	2210^{+90}_{-90}	7370^{+415}_{-410}	0.54	121	403	523
150243.09+111557.3	comp	<8	<7	<39.2	<150		<2.1	<8.2	<10
154107.81+203608.8	main	653^{+23}_{-22}	201^{+13}_{-13}	1250^{+40}_{-45}	1680^{+110}_{-105}	0.15	128	173	301
154107.81+203608.8	comp	<3	<3	<5.52	<25.1		<0.57	<2.6	<3.1
161027.41+130806.8	main	52^{+6}_{-6}	116^{+10}_{-10}	162^{+20}_{-20}	1870^{+160}_{-155}	0.84	2.6	30	32
161027.41+130806.8	comp	<3	<3	<8.43	<44.3		<0.13	<0.71	<0.84
165206.15+310707.6	main	1^{+2}_{-1}	51^{+7}_{-6}	$2.76^{+4.37}_{-1.36}$	1420^{+180}_{-180}	1.00	0.004	2.0	2.0
165206.15+310707.6	comp	<3	<3	<6.44	<29.5		<0.009	<0.042	<0.05

7.5.2 X-Ray Hardness Ratio and Spectral Analysis

Since the possible two X-ray sources in each object have such small separations and low X-ray counts, it will be difficult to reliably extract spectra and perform fitting for each component independently. We will instead extract a spectrum that combines both sources. Depending on the number of counts available, we will perform one or both of the following fitting methods.

With few counts available, we can estimate parameters of X-ray spectral models using the hardness ratio (HR) as a proxy for more complex spectral fitting. This process is defined in Subsection 7.4.4. We show the HRs and $L_{0.5-10keV}$ for our 12 original candidates in Figure 7.13. Luminosities above 10^{42} ergs s^{-1} and hardness ratios above zero indicate that **all** of our main objects with detectable X-ray counts are AGN. The luminosities and HRs of the five companions suggest that all five could be AGN. However, the main AGNs of all five systems have flux scattered around themselves at multiple angles/locations. For our initial estimates, we have presumed that the flux at the companion's location is from companion. 2D modeling is needed to determine if a second AGN is causing the flux at the companion's location.

For objects with somewhat higher count levels (>50), we will attempt to fit the unbinned spectrum in `Sherpa` using `cstat` statistics and the `simplex` optimization method. The initial model will be an absorbed power law (`powlaw1d`); the absorption (`xsphabs`) will include both a fixed column density component set to the Galactic value (Dickey & Lockman, 1990) and a varying column density component with the redshift of the SDSS AGN. We will also try adding an additional component for objects that

appear double from our 2D fitting. If the object is borderline faint, we can also more simply estimate the object's intrinsic galactic column density by fixing the photon index Γ to 1.8, a typical value for low redshift unobscured Seyferts (e.g., Nandra & Pounds, 1994; Green et al., 2009). Measuring the column density of our objects will allow us to test if double-peaked AGNs have higher-than-average column densities.

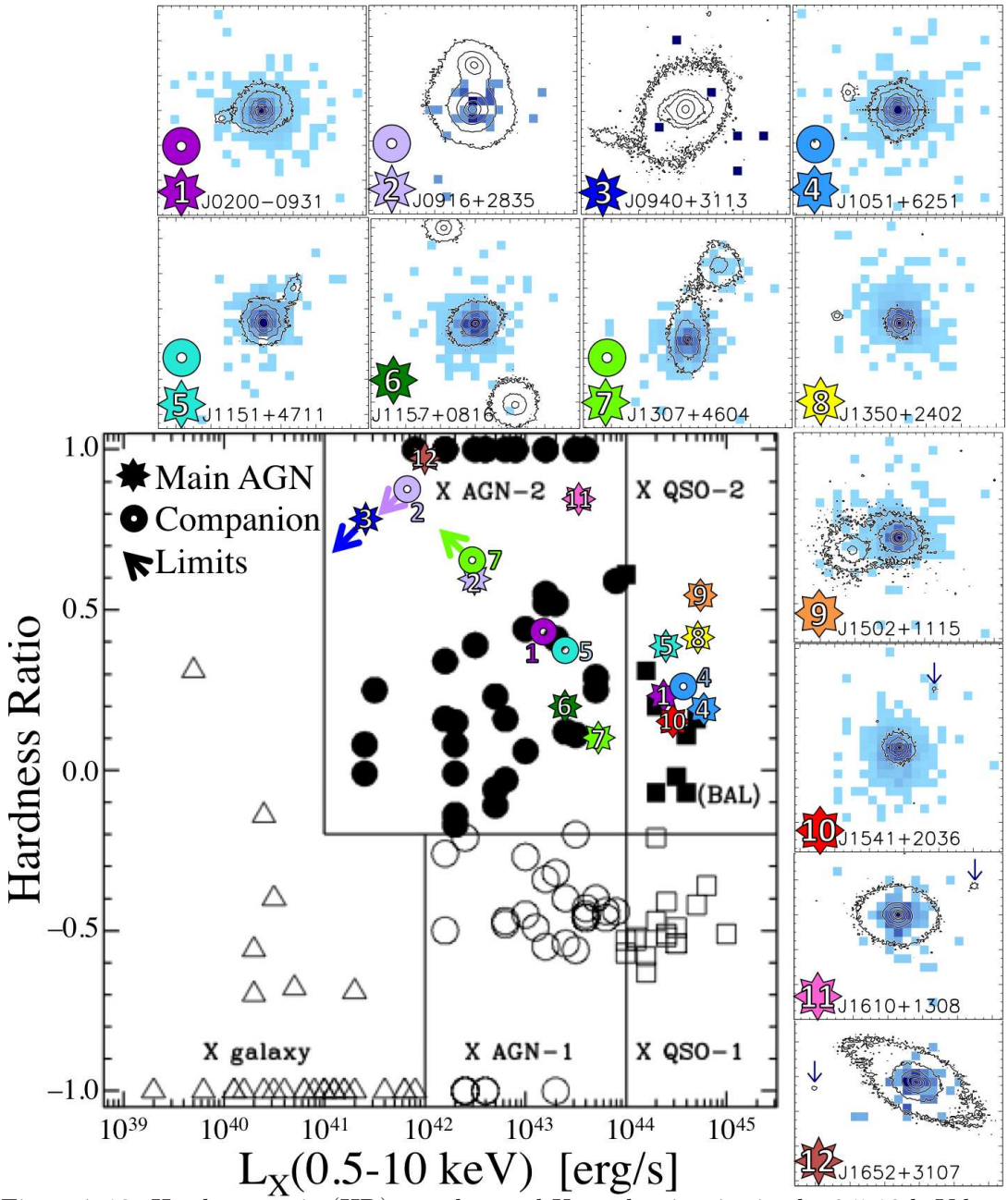

Figure 7.13: Hardness ratio (HR) vs. observed X-ray luminosity in the 0.5-10 keV band (Szokoly et al., 2004) with our 12 *Chandra* observed candidates over-plotted. Each candidate dual AGN object is denoted by a specific color matched to the surrounding X-ray images with near-IR contours. Upward-pointing (downward-pointing) arrows indicate objects with an 90% confidence upper limit measurement for the soft (hard) X-ray luminosity. Luminosities above 10^{42} ergs s^{-1} indicate that **all** of our main objects with detectable X-ray counts are AGN. The luminosities and HRs of the five companions suggest that all five could be AGN. However, 2D modeling is needed to determine if a second AGN is responsible for the X-ray flux near the near-IR companion.

7.6 Conclusion

Out of the 20 spatially double candidate dual AGNs observed, 12 objects were observed through our *Chandra* proposal and 8 objects have observations in the archives. 7 objects that are spatially single in our near-IR imaging also have archival *Chandra* observations. We present a comparison of our X-ray and near-IR images for all 27 candidate dual AGNs.

We have fully analyzed one candidate dual AGN, J1307+4604, as described above. We find that both the main galaxy and the companion galaxy contain independent X-ray sources with 0.5–10 keV luminosities greater than 10^{42} ergs s^{-1}, proving that both sources contain an AGN. Their hardness ratios suggest that the objects are hard, or obscured.

Work is needed to complete our X-ray analysis for all 27 double-peaked [O III] AGNs observed with *Chandra*. Of our 11 remaining original candidates, we have 3-5 that have X-ray flux distributed over the location of the near-IR companion. Further analysis is needed to determine if these candidates are dual AGNs. For the archival objects, Liu et al. (2013) determine that 2 of their 3 shared candidates are dual AGNs, and Comerford et al. (2015) finds 1 dual AGN and 3 possible dual/offset AGNs. Performing a uniform analysis of all 27 candidates will help us to determine if double-peaked [O III] is a useful technique for selecting dual AGNs. If our analysis agrees with those of Liu et al. and Comerford et al., this suggests that we have 4 already confirmed dual AGNs in our sample of 20. At minimum, using near-IR spatially double SDSS AGNs with double-peaked [O III] gives a 20%±4% success rate of finding dual AGNs. This coincidently

agrees quite well with the rate found from spectroscopic confirmation.

Part IV

Instrumentation

Chapter 8

Constructing and Commissioning ShARCS: the Shane Adaptive optics infraRed Camera-Spectrograph for the Lick Observatory 3-m Telescope

Some of the questions that have arisen while studying these double-peaked [O III] AGNs can only be answered by getting many adaptive optics-assisted observations. For example, imaging a redshift and mass-matched control sample of SDSS AGNs with single [O III] peaks would have addressed whether double-peaked AGNs were more or less likely to be in late-stage mergers. Acquiring AO-assisted near-IR spectroscopy

of all 140 double-peaked [O III] AGNs, or even just the 42 double-peaked AGNs with a nearby companion, would conclusively confirm or disprove them as dual AGNs and building a larger sample would increase the strength of the results found and allow us to study how the results change with companion separation. However, getting enough AO-assisted observational time on 8-10 m telescopes to increase sample sizes remains a challenge. Placing new AO systems and high spatial resolution instruments on 2-6 m telescopes is a fantastic method to revitalize these telescopes. Since observational time is more abundantly available, multi-object imaging surveys or deep spectroscopy campaigns become possible.

The following Chapter is about the construction and commissioning of the **Sh**ane **A**daptive optics infra**R**ed **C**amera-**S**pectrograph (ShARCS). We had hoped to use ShARCS and its accompanying new AO system to carry out at least one of the observing campaigns described above; however, the AO system and instrument were not completed in time to fit this work in a six year thesis. Regardless, the construction, testing, and commissioning of ShARCS was a valuable experience and created a useful instrument for future science.

8.1 General Specifications

Several near-infrared cameras have taken images corrected using the original laser guide star adaptive optics (AO) system that was installed on the Shane 3-m telescope at Lick Observatory in 1994 (Gilmore et al., 1995; Bauman et al., 1999). Prior to November 1998, the Lick InfraRed Camera (LIRC-2) was used as an interim science

camera (Gilmore et al., 1995); however, LIRC-2 was designed as a seeing-limited instrument, not optimized for AO performance. In 1998, LIRC-2 was replaced by the InfraRed Camera for Adaptive optics at Lick Observatory (IRCAL) (Hanson, 2000). IRCAL was a 1.0-2.5 μm camera and polarimeter optimized for use with the Lick laser guide star AO system. The Lick adaptive optics system was mounted at the f/17 Cassegrain focus of the Shane 3-m telescope, and delivered a corrected f/28.5 beam to IRCAL. Using diamond-turned gold-coated aluminum optics, IRCAL provided diffraction-limited imaging in the near-infrared (IR). IRCAL's detector was an anti-reflection coated Rockwell 256 $\times$ 256 PICNIC array with 40 μm pixels. IRCAL was Nyqusit-sampled for a corrected K-band beam, and offered a field of view of $20''$. The Lick AO system generally produced Strehl ratios of 0.3 in K-band with laser guide star observing.

The new ShaneAO adaptive optics system is designed to produce diffraction-limited images in the J, H, and K-bands (Gavel, 2011; Kupke et al., 2012; Gavel et al., 2014). ShaneAO has two deformable mirrors in a woofer-tweeter wavefront correction system. The first mirror, the "woofer," is a high stroke, voice-coil actuated ALPAO deformable mirror; it provides tip-tilt and low-order wavefront correction. The second mirror, the "tweeter," is a high temporal and spatial bandwidth, low stroke Boston-Micromachines 32x32 MEMs deformable mirror, and provides high order corrections. A high-sensitivity, high-bandwidth wavefront sensor camera with several Shack-Hartmann sampling modes is located after the second deformable mirror. The current dye laser, in operation since 1996, will be replaced in the coming year with a fiber laser developed at Lawrence Livermore National Laboratories.

Table 8.1: ShARCS Observing Modes and Details

Observing Mode	Filters	Details
Imaging:	various narrow-band filters, J, H, K, Ks band filters	• Occulting finger diameter = 0.8″ • 2, 3, 4, 4 pixels per lambda/D sampling, respectively
Spectroscopy:[23]	H and K grisms	• R∼300, Dispersion=1000 km s^{-1}, slit size 0.15″×6.9″
Polarimetry:[24]	Wollaston prism	• Half Field aperture = 31.4″×8.4″ • Used with the externally mounted wave plate

The **Sh**ane **A**daptive optics infra**R**ed **C**amera-**S**pectrograph (ShARCS) is designed to work behind the ShaneAO system. ShARCS provides diffraction-limited and Nyquist-sampled images for J, H, and K-band beams over a 20″ field of view. Additionally, ShARCS is equipped for low resolution (R∼300) long-slit spectroscopy and linear polarimetry. Table 8.1 summarizes the various operational modes of ShARCS. ShARCS and ShaneAO are made possible through an National Science Foundation Major Research Instrumentation grant, #0923585. Section 8.2 discusses details of ShARCS's construction and testing. Section 8.3 summarizes early science taken during commissioning.

8.2 Instrument

Much of the existing hardware from the IRCAL dewar was reused for ShARCS. The original liquid nitrogen cooled dewar, with a vapor-cooled radiation shield, houses ShARCS. The addition of an ion pump has increased the hold time to at least 36 hours under normal conditions. IRCAL's aperture wheel and two filter wheels are reused in

[23]Spectroscopy mode is available, but not yet fully commissioned.
[24]Polarimetry mode is in progress and not yet available

Table 8.2: Contents of ShARCS Aperture and Filter Wheels

Aperture Masks in Aperture Wheel	**Filters in Filter Wheel #1**	**Filters in Filter Wheel #2**
Vertical slit, $0.15'' \times 6.9''$ (for spectroscopy)	K grism with R$\sim$300, Dispersion = 4.3 μm = 600 km s^{-1}	H grism with R$\sim$300, Dispersion = 3.3 μm = 600 km s^{-1}
Half-field (for polarimetry)	Pupil Viewer	Dark position
Open (for imaging)	BrGamma narrow	Open
Horizontal slit, $6.9'' \times 0.15''$	H_2 1-0 S(1) narrow	J CH_4 narrow
Occulting Finger, $0.8''$ wide	Ks continuum	K CH_4 medium
Pinhole $0.15''$diam	H continuum	K continuum
	J continuum	Wollaston Prism
	Open	[Fe II] narrow

ShARCS; located inside the cooled dewar, the three wheels are driven with new external servo motors via mechanical feedthroughs. The contents of the aperture and filter wheels are summarized in Table 8.2. The aperture wheel contains two slits, a pinhole, an occulting finger, a half field used for polarimetry, and an open position, as well as two filter wheels. The filter wheels contain a variety of narrow and broad bandpass near-IR filters (see Table 8.3), two low-resolution (R$\sim$300) grisms for spectroscopy, a pupil viewer to aid in alignment, and a Wollaston prism, used with a deployable waveplate in the adaptive optics relay, for polarimetry. Table 8.1 contains a summary of the various observing modes that are supported.

The upgraded cryogenic and mechanical components of the instrument were manufactured by the University of Calfiornia Observatories technical shops in Santa Cruz, California. The original IRCAL components were made by IR Labs, Inc.

8.2.1 Optics

The new optics used in ShARCS are an optimized pair of off-axis parabolas and two fold mirrors; all four optics are diamond-turned gold-coated aluminum. As shown in Figure 8.1, light from the AO system enters the dewar window and comes to a focus at the aperture wheel, deflects off the first fold mirror, is collimated by the first off-axis parabola, forms an image of the pupil at the cold stop (described below), passes through the two filter wheels, is focused by the second off-axis parabola, deflects off the fold mirror, and encounters the detector.

The Telescope Utilization Bin (TUB) is the rotatable mounting point for instruments using the Shane Telescopes's Cassegrain focus. Unlike the previous Lick adaptive optics system, ShaneAO is mounted to the TUB in a way that enables TUB rotation; this will allow the strategic orientation of the science object on the slit or occulting finger. As the TUB rotates, the secondary support spiders will also appear to rotate as viewed in the pupil image at the science camera's cold stop and in the varying point spread function at the science detector. Since the previous AO system did not rotate, the cold stop included masking spiders to block the emission from the secondary support spiders. ShaneAO does not mask the spiders since it is impractical to co-rotate the mask inside the dewar. Estimates of the thermal emissivity of the secondary support spiders indicated that they would not contribute significantly to the background seen at the science detector. This was confirmed by analysis of ShARCS commissioning images.

The ShARCS pupil image at the cold stop is 3.85 mm in diameter. To prevent

[25] Vacuum wavelengths
[26] Specified, not measured
[27] Unblocked, needs to be crossed with the J filter for blocking

Table 8.3: ShARCS Filter Specifications

Filter Name	λ_{den} (μm)[25]	FWHM (μm)[25]	Peak Transmission (%)	Normally Available
J	1.238	0.271	82	Y
H	1.656	0.296	85	Y
K_{short}	2.150	0.320	_[26]	Y
K	2.195	0.411	75	Y
H continuum	1.570	0.020	_[26]	N
[Fe II]	1.644	0.016	_[26]	Y
H_2 1-0 S(1)	2.125	0.020	80	Y
BrGamma H I (n=7-4)	2.167	0.020	78	Y
2.2/0.04	2.192	0.047	79	N
K continuum	2.270	0.020	_[26]	N
K CH_4	2.356	0.130	80	Y
J CH_4	1.183	0.040	86[27]	Y

the leakage of thermal background, the outer diameter of the new cold stop has been undersized by 100 μm, or 2.6%, and the mask for the secondary obscuration has been oversized by 100 μm, or 2.6%. The new cold stop is make from photomasked chrome with an optical density of 5 on a quartz substrate. The quartz has an anti-reflection coating on both sides. Additionally, the cold stop has been relocated from downstream of the filter wheels to directly in front of the filter wheels, as seen in Figure 8.1. This will create a consistent point spread function for the entire spectrum diffracted by the grisms and both beams created by the Wollaston prism.

The aperture wheel in ShARCS contains a 100 μm pinhole, a 100 μm vertical slit for grism spectroscopy, a half-field mask for polarimetry, an open slot, a 100 μm horizontal slit, and an occulting finger for coronagraphy. The positioning accuracy in the aperture wheel has been improved in ShARCS so that the finger and slit now land within 2-3 pixels of their set positions. Similar to IRCAL, ShARCS has a standard set

of filters mounted, which can be swapped out by request. The available filters are listed in Table 8.3. Filter wheel #1, closest to the detector, contains a CaF K-band grism (R∼300), an H-band Pupil Viewer, an open slot, and the following filters: Br Gamma, H_2 1-0 S(1), K_{short}, H, and J. Filter wheel #2, furthest from the detector and closest to the cold stop, contains a H-band grism (R∼300), a solid blank for darks, an open slot, the Wollaston Prism, and the following filters: J CH_4, K CH_4, K, and [Fe II].

8.2.2 Detector Description

The heart of the upgrade from IRCAL to ShARCS is replacing the science detector. IRCAL used an anti-reflection coated Rockwell 256 × 256 PICNIC array with 40 μm pixels; it was sensitive from 0.85 – 2.5 μm with quantum efficiencies between 60 – 65%, and had a field of view of 19.5″. The plate scale was 0.0780″ pixel^{-1} in the Right Ascension direction and 0.0754″ pixel^{-1} in the Declination direction. IRCAL was diffraction-limited and Nyquist sampled in K-band.

ShARCS uses a Teledyne HAWAII-2RG (H2RG) HgCdTe engineering-grade near-infrared detector. Out of the detector's 2048 × 2048 square pixels, 1976 × 1453 pixels (69.0%) are operable and light sensitive, with 4 rows and columns of reference pixels along the sides of the detector. We are using 600 × 600 square pixels to cover the same ∼20″ field of view as IRCAL. If a higher resolution grism is installed in the future, the off-axis parabolic mirror that forms the final image of the science detector is over-sized to allow more of the detector's operable region to be illuminated for wider wavelength coverage. The decreased plate scale of 0.033″ pixel^{-1} makes ShARCS diffraction-limited and Nyquist-sampled through the J, H, and K-bands. The detector

Table 8.4: ShARCS Detector Characteristics

Detector:	Teledyne HAWAII-2RG
Pixel size:	18 μm
Image plate scale:	0.033 arcsec/pixel
Unvignetted Square Field:	$20'' \times 20''$
Illuminated Circular Field:	Circular region, diameter 840 pixels = $27.7''$
Operational area:	1976 $\times$ 1453 pixels (69.0%)
Minimum full frame readout time:	1.45 seconds
Windowing mode readout time:	0.11 seconds with 100$\times$100 square pixel region
Quantum efficiency:	85% over wavelength range 1.0 –2.5μm
Read noise:	21 e^- with CDS
	6 e^- with 16 Fowler reads
	5 e^- with 32 Fowler reads
Gain:	2.35 e^-/DN
Linearity:	$\sim$30,000 DN, or $\sim$70,500 e^-

has a quantum efficiency of 82% over the wavelength range 0.6 – 1.0 μm and a quantum efficiency of 85% over the wavelength range 1.0 – 2.5 μm.

We chose to drive the H2RG with the SIDECAR application specific integrated circuit (ASIC) from Teledyne Imaging Sensors. The ASIC provides clocks and bias voltages to the detector and digitizes the detector outputs. As shown on the right in Figure 8.1, the cryogenic ASIC is a small circuit board located inside the ShARCS dewar above the detector. A ribbon cable is potted through the dewar wall to connect the cryogenic ASIC to the Jade2 board, mounted on the outside dewar wall. The Jade2 provides the interface between the ASIC and USB 2.0.

8.2.3 Detector Characterization

The detector can read out using 1, 4, or 32 output channels; 32 outputs gives the shortest base read time of 1.45 seconds, so this is the mode we generally use. As shown in Figure 8.2, the detector system is linear to approximately 35,000 DN. The

slope is related to the gain using: slope= $\sqrt{2}$/gain. From our measured slope of 0.626, we calculate the gain to be 2.25 e^- DN^{-1}; using the gain, we calculate that the detector system is linear up to about 82,000 e^-.

Figure 8.3 plots the measured total noise as a function of the number of Fowler reads using exposures of different durations, each just long enough to accommodate the set of multiple reads. The total noise, plotted as black diamonds connected by a black line, is measured from the variance in the difference of two frames with identical exposure times and numbers of reads, over the full functional detector area. The measured charge accumulated in each frame increases as the number of reads, and thus minimum exposure time, increases. This charge comes from dark current and additional background due to the incomplete baffling of the detector when these test data were taken. The Poisson noise contribution to the total measured noise in each difference frame is plotted as the blue dashed curve. The read noise is calculated as $\sqrt{(\text{total noise})^2 - (\text{Poisson noise})^2}$, the square root of the squared Poisson noise subtracted from the squared total noise, and is plotted as the red dot-dashed curve.

IRCAL's PICNIC array had 30 e^- of read noise with 1 read per pair (Correlated Double Sampling, CDS) and 12 e^- of read noise with 16 reads per pair (Multi-Correlated Double Sampling, MCDS). We find that our data on the ShARCS's H2RG and SIDECAR ASIC detector system in the final dewar is consistent with having 22 e^- of read noise with 1 read per pair and 5 e^- of read noise with 16 reads per pair.

8.2.4 Software

A goal of the ShARCS software design was to use and build upon existing code created to run the H2RG in Keck Observatory's MOSFIRE instrument (McLean et al., 2010, 2012). This existing code was created at the University of California at Los Angeles Infrared Lab. The ShARCS computer architecture consists of two main computers: a detector control computer and an instrument host computer. The detector control computer's responsibility is to run the ShARCS ASIC Server and SIDECAR ASIC control software; this provides the low-level software interface to the Teledyne controller. This computer runs Microsoft's Windows XP Professional and is mounted in the instrument and ShaneAO electronics cabinet. The instrument host computer interfaces with the detector control server and connects to the data storage archive. This system runs CentOS Linux 6.3 and lives in the Shane 3-m dome computer room. Additional top-level software controlled by observers uses the interface provided by the Linux computer to configure the instrument and take data.

ShARCS detector software employs a client-server architecture which facilitates distributed processing and remote observing. The MOSFIRE Detector Server (MDS) was implemented as a shareable library driven by the Keck Observatory standard application *rpc_server* which used Sun remote procedure calls (RPC) to implement the standard Keck Task Library (KTL) communications (Kwok & Cohen, 2002). When we received the software, *rpc_server* had Solaris dependencies that prevented it from running on our Linux platform, and we therefore created a substitute application, *mr_server*, that would run the MDS library without modification, but without using

RPC-based communications. Other software was unaffected by the server-side change, and did not require any modification. Like the Keck standard, simple client commands, such as "show" and "modify", facilitate easy access to and the scripting of the server's keywords. By using existing KTL interfaces to other popular languages such as Java, IDL, Python, and Tcl, a diverse range of user interfaces can be implemented.

From the observer's top-level view, the ShARCS software is broken into several different sub-units. *sharcs_fe* is the graphical user interface (GUI) written in Java that interfaces with *mr_server*, configures the detector, takes exposures, and manages scripts that nod the telescope, take exposures, and control the Adaptive Optics Loops. *sharcswheels_gui* is a Python GUI that allows observers to move the filter and aperture wheels. *sharcsdisplay* is an Tcl and IDL-based imaged display widget that allows the observer to manipulated the image using either the GUI or regular IDL commands. *eventsounds* is a program that allows the observer to pick which sounds signal different events in *sharcs_fe*, such as the end of exposures and the end of a script.

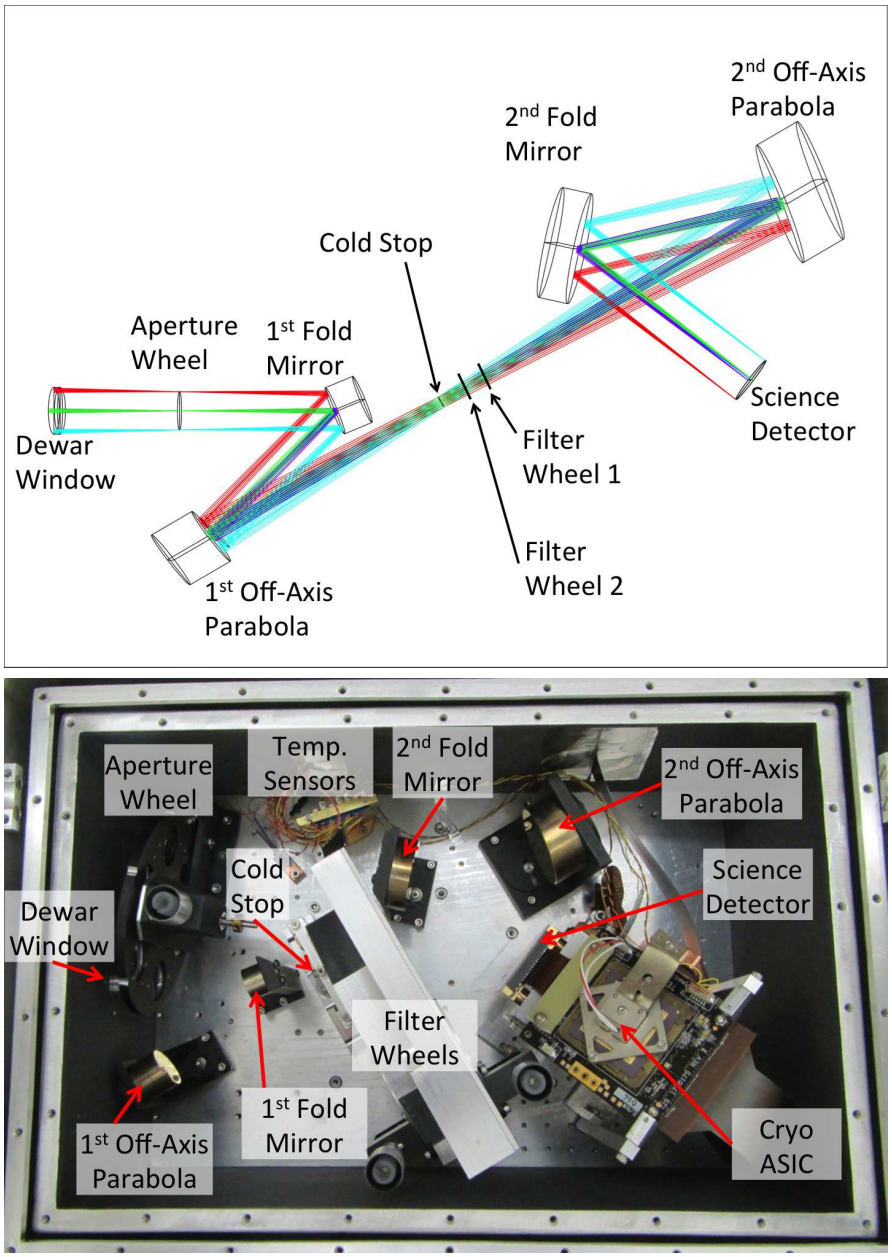

Figure 8.1: ShARCS Optical Design (top) and Optical Bench Simulation (bottom). In both images, the light from the AO system enters on the left through a 0.85 inch diameter CaF_2 window. The converging f/28.5 beam forms a focal plane at the aperture wheel, is folded to the first off-axis parabola, and forms an image of the pupil on the 2.6 % undersized cold stop. The collimated beam passes through the two filter wheels, is focused by the second off-axis parabola, and folds onto the 5^o tilted Teledyne H2RG detector read out by a cryogenic ASIC board. Before taking this bottom photograph, the baffling around the beam both before and after the filter wheels has been temporarily removed for clarity.

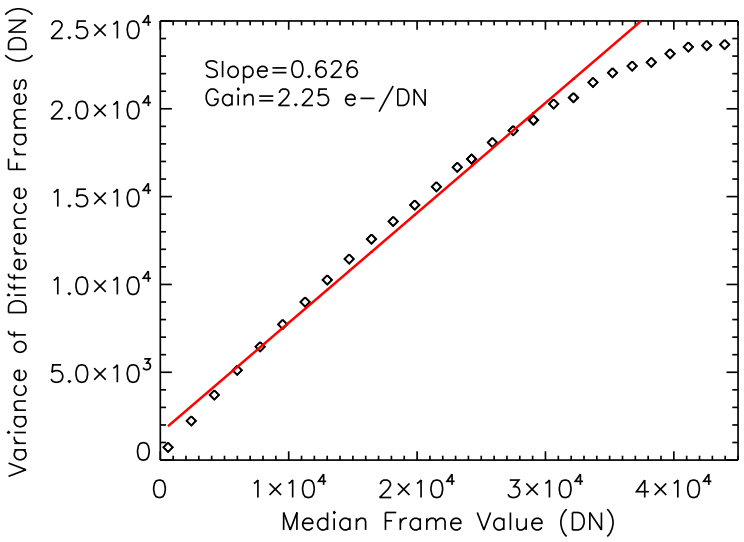

Figure 8.2: Linearity plot. We took a series of image pairs of an evenly illuminated area of the dome with increasing exposure times. For this test, we select a 300 × 300 square pixel box from which to measure our statistics (similar answers are found with a variety of box sizes and region choices) and remove the known bad pixels. The x-axis shows the 5-sigma clipped median value in DN for each frame, and the y-axis shows the 5-sigma clipped variance in the difference of the two frames in each image pair in DN. The overplotted line shows the fit to the linear portion of the data; the detector system is linear to about 35,000 DN, or about 82,000 e^-. From our measured slope of 0.626, we calculate the gain to be 2.25 e^- DN^{-1}.

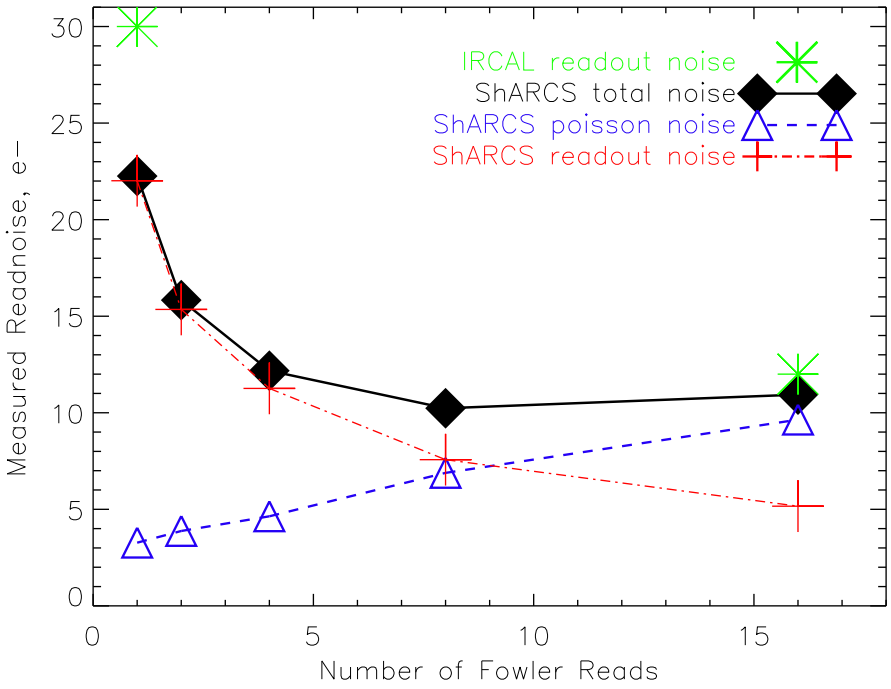

Figure 8.3: Fowler Pairs plot. We took a series of dark images at the minimum exposure times possible for 1, 2, 4, 8, and 16 read pairs. The total noise averaged over the detector's full functional region is measured and plotted as filled black diamond points connected by a solid black line. The poisson noise from the measured charge accumulation during these increasing exposure times increases as shown in the blue dashed curve. The readout noise is calculated from the square root of the squared Poisson noise subtracted from the squared total noise; the readout noise is plotted as the red dot-dashed curve. We calculate that ShARCS's H2RG and SIDECAR ASIC detector system has read noises of 22 e^{-1} at Nreads=1 and 5 e^{-1} at Nreads=16. The two known points for IRCAL, Nreads=1 with a noise of 30 e^{-} and Nreads=16 with a noise of 12 e^{-}, are overplotted as green asterisks for comparison.

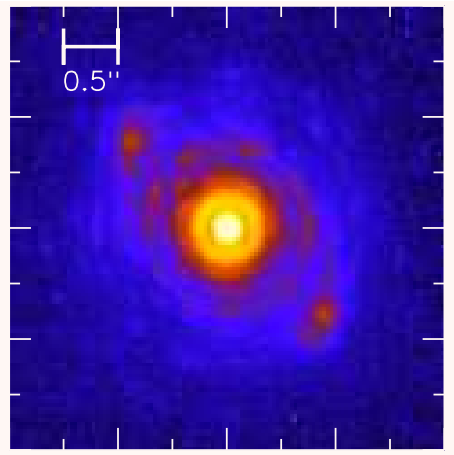

Figure 8.4: First light image of Phi Gem, taken in the first hour on-sky. The narrow Brγ filter with λ_{cen}=2.167 μm is used. Image is displayed on a logarithmic scale. Up to 7 Airy rings are visible; using the *sharcsstrehl* IDL tool, we measure a Strehl of 0.52. We measure a FWHM of 0.188$''$, while the diffraction limit in Brγ is 0.149$''$.

8.3 Performance

First light occurred on 2014 April 12 during the first commissioning run. An hour after we got ShaneAO on-sky, we took our first light image of Phi Gem, a V=5.0 star, in narrow Brγ filter with λ_{cen}=2.167 μm. The first light image is shown in Figure 8.4, and, taken after tuning the AO system, a comparison pair of images with the AO system off and on are shown in Figure 8.5. Up to 7 Airy rings are visible. Using the *sharcsstrehl* IDL tool, we measure a Strehl of 0.52. We measure a FWHM of 0.188″, while the diffraction limit in Brγ is 0.149″. Srinath et al. (2014) compare measured results to predicted signal-to-noise ratio and magnitude limits from modeling the emissivity and throughput of ShaneAO and ShARCS.

Figure 8.6 shows a 20″×20″ portion of the globular cluster M92. This image shows the spatial resolution of the new ShaneAO system. The frame on the left shows the data with no AO correction. The panel on the right shows the same field, over the same exposure time, with the new AO system turned on. The three stars in the circle are 0.42″ and 0.58″ apart. For reference, the width of the stars in the "AO off" image is 1″. This image was taken the second good night on sky. ShaneAO can do better: image sharpening can remove static aberrations from the AO system and telescope. M92 is a famous and well-studied cluster, which is why we observed it for commissioning. But the reference star used to compute the AO correction is faint, and we can optimize for better correction with faint reference stars.

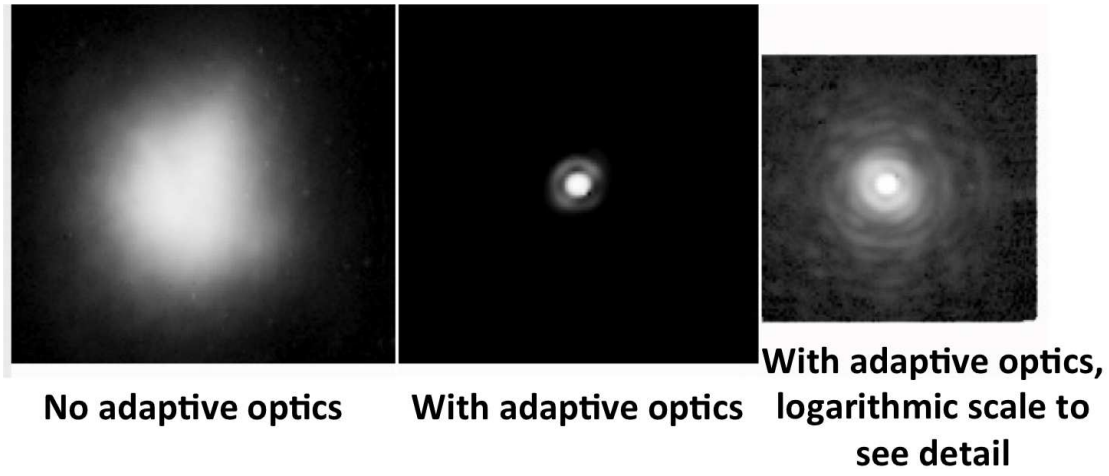

Figure 8.5: ShARCS images of Phi Gem, taken in the narrow Brγ filter with λ_{cen}=2.167 μm. *(left)* Image with the adaptive optics not correcting the atmosphere's turbulence. *(middle)* Image linearly scaled with the adaptive optics system on. *(right)* Image logarithmically scaled with the adaptive optics system on. The Airy rings can be seen very clearly; approximately four full rings and two more partial rings can be seen.

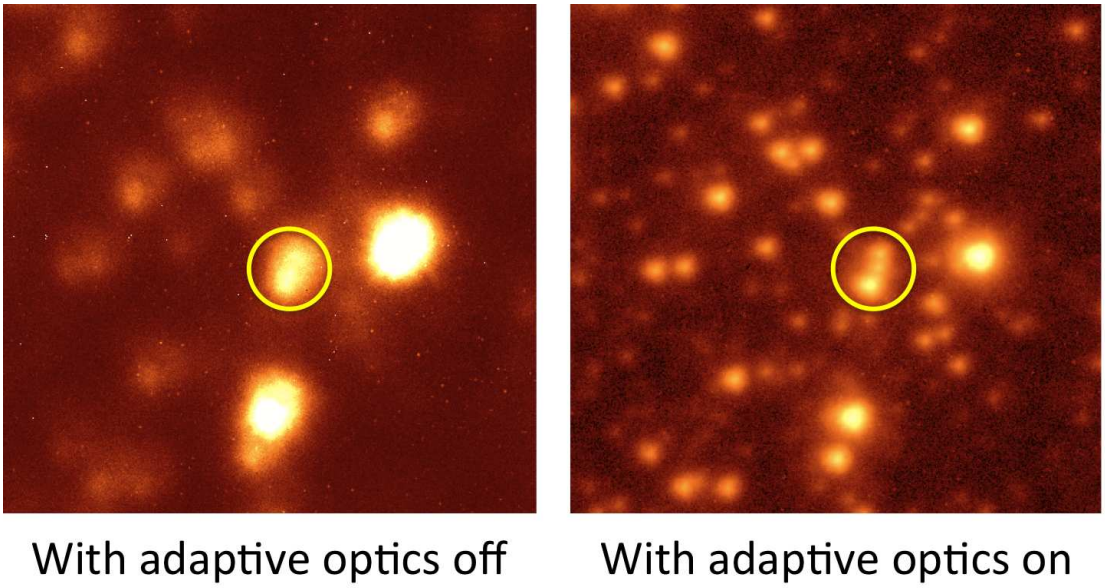

Figure 8.6: ShARCS image of M92, taken in the broad Ks filter with λ_{cen}=2.150 μm. *(left)* Image with the adaptive optics not correcting the atmosphere's turbulence. *(right)* Image with the adaptive optics system on. The three stars in the overplotted yellow circle are 0.42″ and 0.58″ apart. For reference, the width of the stars in the "AO off" image is 1″.

8.3.1 First Spectroscopy

IRCAL was able to perform spectroscopy only by using an extremely convoluted and laborious process of flipping between the open and slit modes of the aperture wheel, due to the unrepeatable positioning of the aperture wheel. While the positioning mechanism of the aperture wheel has been improved in ShARCS, it will need further improvement if spectroscopy will be a main operational mode.

That being said, we present our first attempts at spectroscopy. We use images of the argon arc lamp taken 2015 January 29 to begin our calibrations. After scaling and fitting, we realized that the spectrum needed to be reversed to fit any of the canonical lines and rescaled fluxes taken from Rao et al. (1966). The calibrated arc lamp spectrum is shown in Figure 8.7, with the Rao et al. Argon lines shown in red. A linear wavelength solution was attempted, but met with poor fitting results. A second order polynomial was a more realistic fit, although not perfect; the approximate wavelength solution, starting from column 700 and running to column 1230, is:

$$\lambda(\mu m) = 0.1((\text{pixel\#} - 700)/1010.)^2 + (\text{pixel\#} - 700)/1010. + 1.966 \tag{8.1}$$

Measuring the separation of two lines at the center of spectrum gives us the approximate dispersion of 1 nm pixel^{-1}, or 1010 pixels μm^{-1}. Conceptually, arc lamps emit extremely narrow lines, which are degraded and widened to reflect the resolution of the grism used to observe them. We measure a FWHM of 7 pixels, or 7 nm, for the central line with

$\lambda = 2.20832$ μm. This gives us a spectral resolution R of 315, as calculated below.

$$R = \frac{\lambda_{cen}}{\Delta\lambda} = \frac{2.20832\mu m}{0.007\mu m} = 315 \tag{8.2}$$

This is equivalent to a velocity resolution of 950 km s^{-1}.

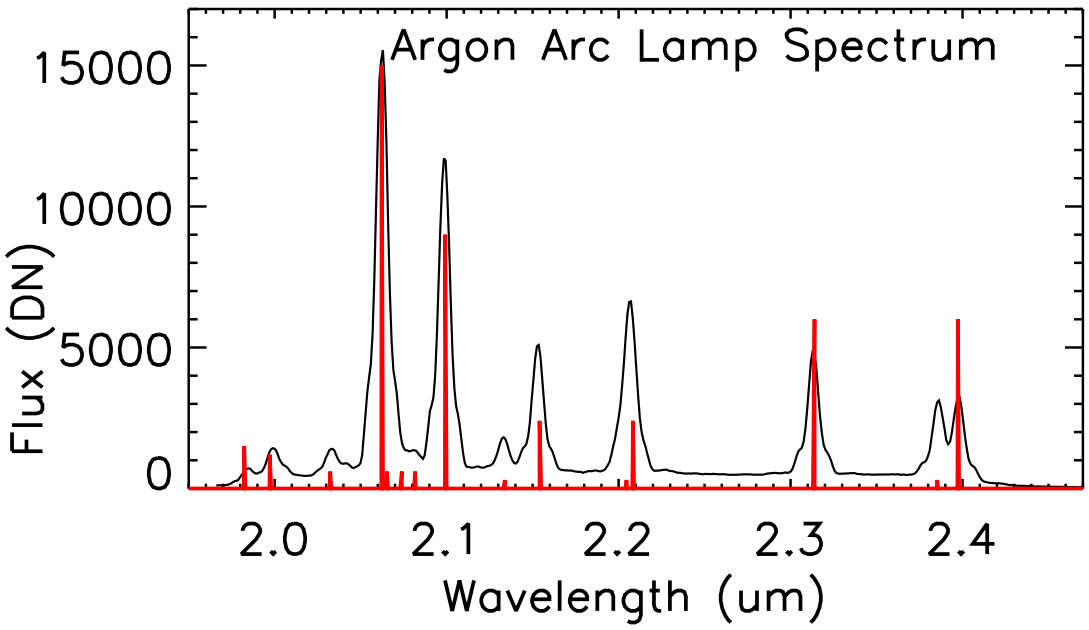

Figure 8.7: ShARCS K-grism Argon Arc Lamp Spectrum. We extracted the median spectrum from 15 rows to prevent blurring as the spectrum is slightly tilted with respect to the rows of the detector. After reversing the spectrum, we are able to fit the canonical Argon lines and rescaled fluxes taken from Rao et al. (1966), shown as thick red lines.

We can use this approximate wavelength solution to observe Markarian 231 (Mrk 231), a local (z=0.042) Ultra Luminous InfraRed Galaxy (ULIRG). This object has $K_{2MASS} = 8.9$ (Cutri et al., 2003). PI Rudy observed Mrk 231 on 2015 March 4 for a total of one hour using the K-grism and K-band blocking filter. He took three 600 second exposures, dithered the object along the slit, and took his second three

600 second exposures. Interestingly, we can see either the AO correction getting worse or the object drifting off the slit at each dither position; the flux is high in the first frame and drops in the following two frames. After performing sky subtractions and extracting the spectra of the 6 exposures, we notice that the spectrum shifts in the wavelength direction by 6 pixels or 6nm between the two dithers. This is unsurprising for two reasons: first, the spectrum is slightly tilted with respect to the rows, since we did not rectify the frames; and second, our slit is not repeatable, which would cause the wavelength calibration to change between respective exposures.

When we combine the six extracted spectra, after shifting the 2nd three spectra by 6 pixels, we create a composite spectrum for Mrk 231, as shown in the top panel of Figure 8.8. This raw spectrum shows two large telluric (atmospheric) absorption bands on the left side of the spectrum, and multiple small telluric absorption bands throughout. We can correct for these features by extracting the spectrum of HD 56386, an A0V star. We note that the observations of HD 56386 were taken on 2015 January 29 (different from the observation of Mrk 231) and at a different airmass, so the telluric absorption bands could be very different. Regardless, we divided the extracted stellar spectrum by a 9480 K blackbody, filled in the Brγ 2.166μm absorption line intrinsic to the star, and normalized the spectrum. Finally, we divide the spectrum of Mrk 231 by the telluric spectrum, getting the bottom panel of Figure 8.8; this correction also effectively corrects for the transmission function of the K-band blocking filter and K grism. The corrected spectrum is quite flat until 2.4 μm; while unfortunately no emission lines are observed in this spectrum, we prove that spectroscopic observations

of bright targets are well within the capabilities of ShARCS.

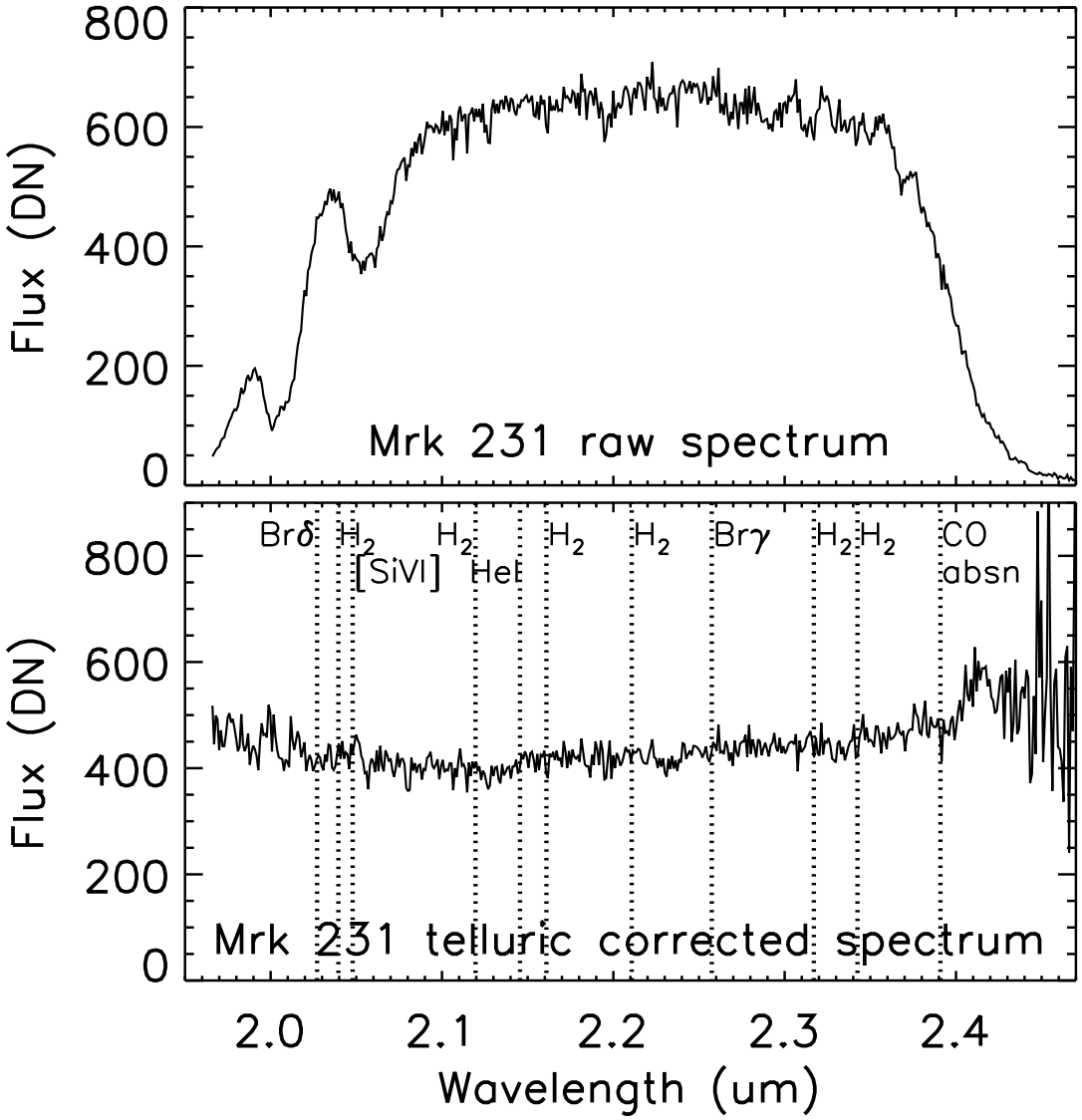

Figure 8.8: ShARCS K-grism spectroscopy of Markarian 231 (Mrk 231). The raw spectrum (**top**) is created from median combining the sky-subtracted spectra of six 600 second exposures. The raw spectrum showcases two large telluric absorption bands at low wavelengths, as well as multiple small telluric absorption bands throughout the spectrum. We correct these features by dividing by the modified spectrum of an A0V star. The corrected spectrum (**bottom**) is remarkably flat until 2.4 μm, where the transmissivity of the K-band begins to drop off. This proves that spectroscopic observations are bright targets are well within the capability of ShARCS.

8.4 Conclusion

We have described the design and first-light early science performance of the **Sh**ane **A**daptive optics infra**R**ed **C**amera-**S**pectrograph (ShARCS) on Lick Observatory's 3-m Shane telescope. Designed to work with the new ShaneAO adaptive optics system, ShARCS is capable of high-efficiency, diffraction-limited imaging in J, H, and K-bands and low-dispersion (R$\sim$300) grism spectroscopy in H and K-bands. ShARCS uses a HAWAII-2RG infrared detector, giving high quantum efficiency (>80%) and Nyquist sampling the diffraction limit in all three wavelength bands.

As shown in the Performance Section (8.3), ShARCS and ShaneAO perform well when bright objects (R $<$ 12) are used as guide stars. Unfortunately, the system still struggles when using faint guide stars (R $>$ 14). This makes the extragalactic science goals proposed at the beginning of this Section (imaging large samples of SDSS AGNs, spectroscopic observations of moderate sample sizes) impossible to achieve with the system's current performance. The new brighter fiber laser developed at Lawrence Livermore National Laboratories and reformatted in the Laboratory for Adaptive Optics will open the door to performing extragalactic science with ShARCS and ShaneAO.

Chapter 9

Conclusions and Future Work

9.1 Conclusions

The goal of this work is to use double-peaked [O III] to build a uniformly-selected sample of dual AGNs with separations of <15 kpc between the two AGN. In Part I, using Keck NIRC2 imaging enhanced with laser guide star adaptive optics, we identify double spatial structure in 43 AGNs of the 140 imaged (31%±3%). Our basic statistics suggest that Type 1 AGNs are approximately twice as likely to be spatially double as Type 2 AGNs, suggesting that selecting Type 1 AGNs for future dual AGN searches may improve the chances of finding spatially double dual AGN candidates.

Unfortunately, the imaging mentioned above does not show whether, or how, the double [O III] emission line structure relates to the presence of a companion. Each candidate dual AGN must be followed up with various techniques to confirm or disprove them as dual AGNs.

In Part II we present the results of spectroscopic confirmation for 13 candidate

dual AGNs. We find: two dual AGNs; five AGNs with outflows; three AGNs with complex narrow line kinematics, spatially unresolved binary AGNs, small scale outflows or jets, rings of star formation, or gas disks; two pairs of an AGN interacting with a star forming galaxy; and one indeterminate candidate in need of further observations. This is a rate of 17% dual AGNs, 42% outflows, 25% unresolved substructure, and 17% AGN/galaxy pairs (all ±6%). We conclude that double-peaked [O III] emission plus double spatial structure can be indicative of dual AGN, but also seems to occur in a number of other interesting scenarios.

In Part III we present a comparison of the X-ray and near-IR images for 20 spatially double candidate dual AGNs and for 7 spatially single candidate dual AGNs observed with *Chandra* and Keck AO NIRC2 and *HST*. We have fully analyzed one candidate dual AGN and found through our modeling that the main galaxy and the companion galaxy contain independent X-ray sources bright enough that they both are AGN. Previously published results of 8 spatially double candidates find 3 additional confirmed dual AGNs (Liu et al., 2013; Comerford et al., 2015). This suggests that there are at least 4 confirmed dual AGNs in our sample of 20, so at minimum using near-IR spatially double SDSS AGNs with double-peaked [O III] give a 20%±4% success rate of finding dual AGNs. This rate agrees within 1σ with the spectroscopic confirmation rate.

We note several biases that enter into the interpretation and analysis of this work. We chose our OSIRIS candidates to have strong companions with moderate ($0\farcs7$–$1\farcs6$) separations, while, due to the limitations of our instrument, we chose our

Kast candidates to have wide ($\geq 1\farcs5$) separations without regard to the strength of the companion. Finally, we chose our 12 *Chandra* candidates both to have a companion separation larger than $1\farcs0$ and to have strong [O III] peaks (to guarantee an X-ray detection); these requirements chose at least 3 AGNs with companions that fall well below a 100:1 merger ratio based on flux, and maybe 3 more candidates with companions that fall below a 10:1 merger ratio based on flux. At least 3 of the 4 detected *Chandra*-confirmed dual AGNs are in more major ($<$ 10:1) mergers, perhaps suggesting that it takes a major merger to disturb enough gas to trigger both AGNs simultaneously. More analysis and objects are needed to confirm this tentative suggestion.

9.2 Short-Term Future Work

9.2.1 Completing *Chandra* Confirmations

First and foremost, work is needed to complete our X-ray analysis for all 27 double-peaked [O III] AGNs observed with *Chandra*; further analysis is needed to determine if these candidates are dual AGNs.

9.2.2 Additional Spectroscopic Confirmation

We have Kast observations of 5 additional wide separation ($>1\farcs5$) spatially double candidate dual AGNs. Data reduction and analysis of these objects should be straight forward, as we will be using the methods and code described in Chapter 5.

9.3 Long-Term Future Thoughts

This work has shown that double-peaked emission lines are not most efficient technique to find dual AGNs. The overall selection of our sample leads to 3 statements: 1) 1% of SDSS AGNs are double peaked (Smith et al., 2010); 2) 31% of these double-peaked AGNs are spatially double in our near-IR imaging; and 3) 17–20% of the spatially double double-peaked AGNs are confirmed to be dual AGNs. From this, we can say that 0.05–0.06% of SDSS AGNs are dual AGNs within $3''$. While this rate is very low, this is still 5 more dual AGNs, and 2 more double-peaked dual AGNs confirmed in Fu et al. (2011b), Peng et al. (2011), and Frey et al. (2012), than we had before this study. At the time this study began seriously, the literature had 10 confirmed dual AGNs; we are now at 25 confirmed dual AGNs in the literature, with 7, or almost one third, coming from double-peaked AGN studies. While the rate is not as high as we had hoped, studies of double-peaked AGNs have contributed significantly to this field. The odds could be stacked more highly in the favor of dual AGNs by only following up the spatially double objects with more major companions (e.g. merger ratios more even than 10:1).

If double-peaked [O III] emission lines are not efficient enough, what are other options for finding dual AGNs? As mentioned in the Introduction, radio interferometry is an efficient technique to confirm small separation dual AGNs (Rodriguez et al., 2006; Owen et al., 1985; Hudson et al., 2006; Wrobel & Laor, 2009; Fu et al., 2011b, to list a few). High resolution radio surveys covering wide areas of the sky would be an effective method to find large samples of dual AGNs. In fact, Fu et al. (2015) have already

searched the 92 deg^2 of the SDSS Strip 82 field covered by a high resolution Very Large Array survey (Hodge et al., 2011); they find 52 candidates with pairs of optical sources enclosed by and associated with discrete radio sources. These moderate separation (1.″5–5.″0) candidate dual AGNs can easily be followed up with spatially resolved spectroscopy and/or X-ray observations to confirm if both galaxies contain AGNs.

X-ray confirmations of AGNs carry significant weight among the various confirmation techniques discussed here, since an X-ray luminous source cannot be mistaken for anything but an AGN. This is especially true at higher energy ranges that better cut through obscuration. However, our objects are currently on the edge of the capabilities of *Chandra* in both spatial resolution and sensitivity. While *NuSTAR* has wider energy coverage (3–79 keV) and sensitivity, its FWHM of 18″ and half power diameter of 58″ likely prevents it from spatially confirming dual AGNs. Without plans for a high resolution X-ray telescope in the immediate future, we will be limited to the capabilities of *Chandra* for some time yet.

The development of near-IR analysis techniques for AGNs and star forming galaxies is a key focus for the immediate future. While one of the goals for the *James Webb Space Telescope* (*JWST*) is to look at optical and ultraviolet spectral features redshifted into the near-IR, *JWST*'s NIRCam and NIRSpec will provide high spatial (0.″032 for NIRCam) and spectral resolutions (R$\leq$2700) to use for the confirmation of low-redshift dual AGNs. This strongly suggests that we should improve our understanding of near-IR AGN and SF emission line ratio diagnostics (Larkin et al., 1998; Rodríguez-Ardila et al., 2008) prior to *JWST*'s launch. Anna Boehle and James Larkin

of UCLA have recently begun work on further exploring this diagnostic diagram.

Finally, to mention a completely different direction of future research, kpc-scale outflows are not well understood currently. We do not know what mechanisms (AGN activity? star formation? both?) drive galactic-scale shocks and outflows, nor do we understand if the various gas phases of outflows are intermixed or spatially distinct. Understanding galactic-scale outflows is important because theory predicts that these outflows are needed to quench SF, limit black hole accretion, alter the mass-metallicity relation, enrich the circumgalactic medium, and give rise to the observed relationships between the central black hole's mass and properties of the galaxy's bulge (e.g. Silk & Rees 1998; Tremonti et al 2004; Springel, Di Matteo, & Hernquist 2005; Hopkins et al. 2008; Narayanan et al. 2008; Tumlinson et al. 2011). An understanding of the physical processes that influence strong outflows is needed in order to model outflows and their effect on galaxy evolution effectively. Coincidently, double-peaked [O III] lines turn out to be efficient selection method for 0.1–5 kpc outflows, as shown in Fu et al. (2012) and McGurk et al. in press. The increasing availability of both optical and near-infrared integral field spectroscopy could widely increase our understanding of these outflows; similar observations of outflows discovered in Herschel (Rupke & Veilleux, 2013b, 2015) are already proving the value of studying outflows with integral field spectroscopy.

Bibliography

Abazajian, K. N., Adelman-McCarthy, J. K., Agüeros, M. A., et al. 2009, ApJS, 182, 543

Baldwin, J. A., Phillips, M. M., & Terlevich, R. 1981, PASP, 93, 5

Ballet, J. 1999, A&AS, 135, 371

Ballo, L., Braito, V., Della Ceca, R., et al. 2004, ApJ, 600, 634

Barrows, R. S., Sandberg Lacy, C. H., Kennefick, J., et al. 2013, ApJ, 769, 95

Barrows, R. S., Stern, D., Madsen, K., et al. 2012, ApJ, 744, 7

Barth, A. J., Bentz, M. C., Greene, J. E., & Ho, L. C. 2008, ApJ, 683, L119

Bauman, B. J., Gavel, D. T., Waltjen, K. E., et al. 1999, in Proc. SPIE, Vol. 3762, Adaptive Optics Systems and Technology, ed. R. K. Tyson & R. Q. Fugate, 194–200

Becker, R. H., White, R. L., & Helfand, D. J. 1995, ApJ, 450, 559

Benítez, E., Méndez-Abreu, J., Fuentes-Carrera, I., et al. 2013, ApJ, 763, 36

Berczik, P., Merritt, D., Spurzem, R., & Bischof, H.-P. 2006, ApJ, 642, L21

Bertin, E., & Arnouts, S. 1996, A&AS, 117, 393

Bianchi, S., Chiaberge, M., Piconcelli, E., Guainazzi, M., & Matt, G. 2008, MNRAS, 386, 105

Blaes, O., Lee, M. H., & Socrates, A. 2002, ApJ, 578, 775

Blecha, L., Loeb, A., & Narayan, R. 2013, MNRAS, 429, 2594

Blumenthal, G. R., Faber, S. M., Primack, J. R., & Rees, M. J. 1984, Nature, 311, 517

Bondi, M., & Pérez-Torres, M.-A. 2010, ApJ, 714, L271

Bonning, E. W., Shields, G. A., & Salviander, S. 2007, ApJ, 666, L13

Boroson, T. A., & Lauer, T. R. 2009, Nature, 458, 53

Cash, W. 1979, ApJ, 228, 939

Cisternas, M., Jahnke, K., Inskip, K. J., et al. 2011, ApJ, 726, 57

Civano, F., Elvis, M., Lanzuisi, G., et al. 2010, ApJ, 717, 209

—. 2012, ApJ, 752, 49

Clavel, J., & Wamsteker, W. 1987, ApJ, 320, L9

Comerford, J. M., Gerke, B. F., Stern, D., et al. 2012, ApJ, 753, 42

Comerford, J. M., Griffith, R. L., Gerke, B. F., et al. 2009a, ApJ, 702, L82

Comerford, J. M., Pooley, D., Barrows, R. S., et al. 2015, arXiv:1504.01391

Comerford, J. M., Pooley, D., Gerke, B. F., & Madejski, G. M. 2011, ApJ, 737, L19

Comerford, J. M., Gerke, B. F., Newman, J. A., et al. 2009b, ApJ, 698, 956

Cutri, R. M., Skrutskie, M. F., van Dyk, S., et al. 2003, VizieR Online Data Catalog, 2246, 0

Dasyra, K. M., Tacconi, L. J., Davies, R. I., et al. 2006, New A Rev., 50, 720

Decarli, R., Dotti, M., Falomo, R., et al. 2009, ApJ, 703, L76

Decarli, R., Dotti, M., Montuori, C., Liimets, T., & Ederoclite, A. 2010, ApJ, 720, L93

Dekel, A., & Birnboim, Y. 2006, MNRAS, 368, 2

Dekel, A., Birnboim, Y., Engel, G., et al. 2009, Nature, 457, 451

Dickey, J. M., & Lockman, F. J. 1990, ARA&A, 28, 215

Dotti, M., Montuori, C., Decarli, R., et al. 2009, MNRAS, 398, L73

Ellison, S. L., Patton, D. R., Mendel, J. T., & Scudder, J. M. 2011, MNRAS, 418, 2043

Escala, A., Larson, R. B., Coppi, P. S., & Mardones, D. 2004, ApJ, 607, 765

Evans, D. A., Fong, W.-F., Hardcastle, M. J., et al. 2008, ApJ, 675, 1057

Fabbiano, G., Wang, J., Elvis, M., & Risaliti, G. 2011, Nature, 477, 431

Falcke, H., Wilson, A. S., & Simpson, C. 1998, ApJ, 502, 199

Ferdman, R. D., van Haasteren, R., Bassa, C. G., et al. 2010, Classical and Quantum Gravity, 27, 084014

Fischer, T. C., Crenshaw, D. M., Kraemer, S. B., et al. 2011, ApJ, 727, 71

Freeman, P., Doe, S., & Siemiginowska, A. 2001, in Society of Photo-Optical Instrumentation Engineers (SPIE) Conference Series, Vol. 4477, Astronomical Data Analysis, ed. J.-L. Starck & F. D. Murtagh, 76–87

Freeman, P. E., Kashyap, V., Rosner, R., & Lamb, D. Q. 2002, ApJS, 138, 185

Frey, S., Paragi, Z., An, T., & Gabányi, K. É. 2012, MNRAS, 425, 1185

Fruscione, A., McDowell, J. C., Allen, G. E., et al. 2006, in Society of Photo-Optical Instrumentation Engineers (SPIE) Conference Series, Vol. 6270, Society of Photo-Optical Instrumentation Engineers (SPIE) Conference Series, 1

Fu, H., Myers, A. D., Djorgovski, S. G., & Yan, L. 2011a, ApJ, 733, 103

Fu, H., Myers, A. D., Djorgovski, S. G., et al. 2015, ApJ, 799, 72

Fu, H., Yan, L., Myers, A. D., et al. 2012, ApJ, 745, 67

Fu, H., Zhang, Z.-Y., Assef, R. J., et al. 2011b, ApJ, 740, L44

Gabányi, K. É., Frey, S., Xiao, T., et al. 2014, MNRAS, 443, 1509

Garmire, G. P., Bautz, M. W., Ford, P. G., Nousek, J. A., & Ricker, Jr., G. R. 2003, in Society of Photo-Optical Instrumentation Engineers (SPIE) Conference Series, Vol. 4851, X-Ray and Gamma-Ray Telescopes and Instruments for Astronomy., ed. J. E. Truemper & H. D. Tananbaum, 28–44

Gavel, D., Kupke, R., Dillon, D., et al. 2014, in Status of Current AO Instrument Projects I, Proc. SPIE

Gavel, D. T. 2011, in Proc. SPIE, Vol. 7931, MEMS Adaptive Optics V, ed. S. S. Olivier, T. G. Bifano, & J. A. Kubby, 793103–1–793103–8

Ge, J.-Q., Hu, C., Wang, J.-M., Bai, J.-M., & Zhang, S. 2012, ApJS, 201, 31

Gerke, B. F., Newman, J. A., Lotz, J., et al. 2007, ApJ, 660, L23

Gilmore, K., Rank, D., & Temi, P. 1995, in IAU Symposium, Vol. 167, New Developments in Array Technology and Applications, ed. A. G. D. Philip, K. Janes, & A. R. Upgren, 79

Green, P. J., Myers, A. D., Barkhouse, W. A., et al. 2010, ApJ, 710, 1578

Green, P. J., Aldcroft, T. L., Richards, G. T., et al. 2009, ApJ, 690, 644

Greene, J. E., Zakamska, N. L., Ho, L. C., & Barth, A. J. 2011, ApJ, 732, 9

Gregg, M. D., Becker, R. H., White, R. L., et al. 2002, ApJ, 573, L85

Guainazzi, M., Piconcelli, E., Jiménez-Bailón, E., & Matt, G. 2005, A&A, 429, L9

Guedes, J., Madau, P., Mayer, L., & Callegari, S. 2011, ApJ, 729, 125

Hanson, K. M. 2000, in Proc. SPIE, Vol. 4008, Optical and IR Telescope Instrumentation

and Detectors, ed. M. Iye & A. F. M. Moorwood, 814–821

Heckman, T. M., Ptak, A., Hornschemeier, A., & Kauffmann, G. 2005, ApJ, 634, 161

Helfand, D. J., White, R. L., & Becker, R. H. 2015, ApJ, 801, 26

Hennawi, J. F., Strauss, M. A., Oguri, M., et al. 2006, AJ, 131, 1

Hennawi, J. F., Myers, A. D., Shen, Y., et al. 2010, ApJ, 719, 1672

Hernquist, L. 1989, Nature, 340, 687

Hinshaw, G., Weiland, J. L., Hill, R. S., et al. 2009, ApJS, 180, 225

Hobbs, G., Archibald, A., Arzoumanian, Z., et al. 2010, Classical and Quantum Gravity, 27, 084013

Hodge, J. A., Becker, R. H., White, R. L., Richards, G. T., & Zeimann, G. R. 2011, AJ, 142, 3

Hopkins, A. M., Miller, C. J., Nichol, R. C., et al. 2003, ApJ, 599, 971

Hopkins, P. F., Hernquist, L., Cox, T. J., et al. 2006, ApJS, 163, 1

Hopkins, P. F., Hernquist, L., Cox, T. J., & Kereš, D. 2008, ApJS, 175, 356

Hopkins, P. F., Torrey, P., Faucher-Giguere, C.-A., Quataert, E., & Murray, N. 2015, ArXiv e-prints, arXiv:1504.05209

Huang, Y., Liu, X.-W., Yuan, H.-B., et al. 2014, MNRAS, 439, 2927

Hudson, D. S., Reiprich, T. H., Clarke, T. E., & Sarazin, C. L. 2006, A&A, 453, 433

Hughes, S. A. 2002, MNRAS, 331, 805

Imanishi, M., & Saito, Y. 2014, ApJ, 780, 106

Jenet, F., Finn, L. S., Lazio, J., et al. 2009, ArXiv e-prints, arXiv:0909.1058

Junkkarinen, V., Shields, G. A., Beaver, E. A., et al. 2001, ApJ, 549, L155

Kauffmann, G., & Haehnelt, M. 2000, MNRAS, 311, 576

Kauffmann, G., Heckman, T. M., Tremonti, C., et al. 2003, MNRAS, 346, 1055

Kewley, L. J., Dopita, M. A., Sutherland, R. S., Heisler, C. A., & Trevena, J. 2001, ApJ, 556, 121

Kocevski, D. D., Faber, S. M., Mozena, M., et al. 2012, ApJ, 744, 148

Komossa, S., Burwitz, V., Hasinger, G., et al. 2003, ApJ, 582, L15

Komossa, S., Zhou, H., & Lu, H. 2008, ApJ, 678, L81

Kormendy, J., & Richstone, D. 1995, ARA&A, 33, 581

Koss, M., Mushotzky, R., Treister, E., et al. 2012, ApJ, 746, L22

Koss, M., Mushotzky, R., Veilleux, S., & Winter, L. 2010, ApJ, 716, L125

Koss, M., Mushotzky, R., Veilleux, S., et al. 2011a, ApJ, 739, 57

Koss, M., Mushotzky, R., Treister, E., et al. 2011b, ApJ, 735, L42

Kupke, R., Gavel, D., Roskosi, C., et al. 2012, in Proc. SPIE, Vol. 8447, Adaptive Optics Systems III, ed. B. L. Ellerbroek, E. Marchetti, & J.-P. Véran, 7pp.

Kwok, S. H., & Cohen, R. W. 2002, in Proc. SPIE, Vol. 4845, Advanced Global Communications Technologies for Astronomy II, ed. R. I. Kibrick, 194–200

Lacy, M., Storrie-Lombardi, L. J., Sajina, A., et al. 2004, ApJS, 154, 166

LaMassa, S. M., Heckman, T. M., Ptak, A., & Urry, C. M. 2013, ApJ, 765, L33

Larkin, J., Barczys, M., Krabbe, A., et al. 2006, in Society of Photo-Optical Instrumentation Engineers (SPIE) Conference Series, Vol. 6269, 62691A

Larkin, J. E., Armus, L., Knop, R. A., Soifer, B. T., & Matthews, K. 1998, ApJS, 114, 59

Lee, K. J., Wex, N., Kramer, M., et al. 2011, MNRAS, 414, 3251

Li, J., Kastner, J. H., Prigozhin, G. Y., et al. 2004, ApJ, 610, 1204

Liu, X., Civano, F., Shen, Y., et al. 2013, ApJ, 762, 110

Liu, X., Greene, J. E., Shen, Y., & Strauss, M. A. 2010a, ApJ, 715, L30

Liu, X., Shen, Y., & Strauss, M. A. 2011, ApJ, 736, L7

Liu, X., Shen, Y., Strauss, M. A., & Greene, J. E. 2010b, ApJ, 708, 427

Lodato, G., Nayakshin, S., King, A. R., & Pringle, J. E. 2009, MNRAS, 398, 1392

Manchester, R. N., Hobbs, G., Bailes, M., et al. 2013, PASA, 30, 17

Markwardt, C. B. 2009, in Astronomical Society of the Pacific Conference Series, Vol. 411, Astronomical Data Analysis Software and Systems XVIII, ed. D. A. Bohlender, D. Durand, & P. Dowler, 251

Martel, A. R., Baum, S. A., Sparks, W. B., et al. 1999, ApJS, 122, 81

Mateos, S., Alonso-Herrero, A., Carrera, F. J., et al. 2012, MNRAS, 426, 3271

Max, C. E., Canalizo, G., Macintosh, B. A., et al. 2005, ApJ, 621, 738

Mazzarella, J. M., Iwasawa, K., Vavilkin, T., et al. 2012, AJ, 144, 125

McGurk, R., Rockosi, C., Gavel, D., et al. 2014, in Society of Photo-Optical Instrumentation Engineers (SPIE) Conference Series, Vol. 9148, Society of Photo-Optical Instrumentation Engineers (SPIE) Conference Series, 3

McGurk, R. C., Max, C. E., Medling, A. M., Shields, G. A., & Comerford, J. M. 2015, ApJ, arXiv:1107.2651

McGurk, R. C., Max, C. E., Rosario, D. J., et al. 2011, ApJ, 738, L2

McLean, I. S., Steidel, C. C., Epps, H., et al. 2010, in Proc. SPIE, Vol. 7735, Ground-

based and Airborne Instrumentation for Astronomy III

McLean, I. S., Steidel, C. C., Epps, H. W., et al. 2012, in Proc. SPIE, Vol. 8446, Ground-based and Airborne Instrumentation for Astronomy IV

Merritt, D. 2001, ApJ, 556, 245

Milosavljević, M., & Merritt, D. 2003a, ApJ, 596, 860

Milosavljević, M., & Merritt, D. 2003b, in American Institute of Physics Conference Series, Vol. 686, The Astrophysics of Gravitational Wave Sources, ed. J. M. Centrella, 201–210

Moran, E. C., Halpern, J. P., Bothun, G. D., & Becker, R. H. 1992, AJ, 104, 990

Myers, A. D., Brunner, R. J., Richards, G. T., et al. 2007, ApJ, 658, 99

Myers, A. D., Richards, G. T., Brunner, R. J., et al. 2008, ApJ, 678, 635

Nandra, K., & Pounds, K. A. 1994, MNRAS, 268, 405

Nelder, J. A., & Mead, R. 1965, The Computer Journal, 7, 308

Ohyama, Y., Terashima, Y., & Sakamoto, K. 2015, ArXiv e-prints, arXiv:1503.08555

Owen, F. N., O'Dea, C. P., Inoue, M., & Eilek, J. A. 1985, ApJ, 294, L85

Park, T., Kashyap, V. L., Siemiginowska, A., et al. 2006, ApJ, 652, 610

Peng, C. Y., Ho, L. C., Impey, C. D., & Rix, H.-W. 2002, AJ, 124, 266

Peng, Z.-X., Chen, Y.-M., Gu, Q.-S., & Hu, C. 2011, Research in Astronomy and Astrophysics, 11, 411

Piconcelli, E., Vignali, C., Bianchi, S., et al. 2010, ApJ, 722, L147

Pindor, B., Eisenstein, D. J., Gregg, M. D., et al. 2006, AJ, 131, 41

Preto, M., Berentzen, I., Berczik, P., & Spurzem, R. 2011, ApJ, 732, L26

Rao, K. N., Humphreys, C. J., & Rank, D. H. 1966, Wavelength standards in the infrared

Richstone, D., Ajhar, E. A., Bender, R., et al. 1998, Nature, 395, A14

Riffel, R., Rodríguez-Ardila, A., & Pastoriza, M. G. 2006, A&A, 457, 61

Rodriguez, C., Taylor, G. B., Zavala, R. T., et al. 2006, ApJ, 646, 49

Rodríguez-Ardila, A., Riffel, R., & Carvalho, E. A. 2008, in Revista Mexicana de Astronomia y Astrofisica Conference Series, Vol. 32, Revista Mexicana de Astronomia y Astrofisica Conference Series, 77–79

Rosario, D. J., McGurk, R. C., Max, C. E., Shields, G. A., & Smith, K. L. 2011, ArXiv e-prints, arXiv:1102.1733

Rosario, D. J., Shields, G. A., Taylor, G. B., Salviander, S., & Smith, K. L. 2010, ApJ, 716, 131

Rupke, D. S. N., & Veilleux, S. 2013a, ApJ, 775, L15

—. 2013b, ApJ, 775, L15

—. 2013c, ApJ, 768, 75

—. 2015, ApJ, 801, 126

Schawinski, K., Urry, M., Treister, E., et al. 2011, ApJ, 743, L37

Shabala, S. S., Ash, S., Alexander, P., & Riley, J. M. 2008, MNRAS, 388, 625

Shen, Y., Liu, X., Greene, J. E., & Strauss, M. A. 2011, ApJ, 735, 48

Sillanpaa, A., Haarala, S., Valtonen, M. J., Sundelius, B., & Byrd, G. G. 1988, ApJ, 325, 628

Smith, K. L., Shields, G. A., Bonning, E. W., et al. 2010, ApJ, 716, 866

Smith, K. L., Shields, G. A., Salviander, S., Stevens, A. C., & Rosario, D. J. 2012, ApJ, 752, 63

Spergel, D. N., Bean, R., Doré, O., et al. 2007, ApJS, 170, 377

Srinath, S., Rockosi, C., McGurk, R., et al. 2014, in Status of Current AO Instrument Projects, Proc. SPIE

Stern, D., Eisenhardt, P., Gorjian, V., et al. 2005, ApJ, 631, 163

Stern, D., Assef, R. J., Benford, D. J., et al. 2012, ApJ, 753, 30

Szokoly, G. P., Bergeron, J., Hasinger, G., et al. 2004, ApJS, 155, 271

Thorne, K. S. 1995, in Annals of the New York Academy of Sciences, Vol. 759, Seventeeth Texas Symposium on Relativistic Astrophysics and Cosmology, ed. H. Böhringer, G. E. Morfill, & J. E. Trümper, 127

Treister, E., Schawinski, K., Urry, C. M., & Simmons, B. D. 2012, ApJ, 758, L39

U, V., Medling, A., Sanders, D., et al. 2013, ApJ, 775, 115

Valtonen, M. J., Lehto, H. J., Nilsson, K., et al. 2008, Nature, 452, 851

Vecchio, A., & Wickham, E. D. 2004, Phys. Rev. D, 70, 082002

Veilleux, S., & Osterbrock, D. E. 1987, ApJS, 63, 295

Wang, J.-M., Chen, Y.-M., Hu, C., et al. 2009, ApJ, 705, L76

Weisskopf, M. C., O'dell, S. L., & van Speybroeck, L. P. 1996, in Society of Photo-Optical Instrumentation Engineers (SPIE) Conference Series, Vol. 2805, Multilayer and Grazing Incidence X-Ray/EUV Optics III, ed. R. B. Hoover & A. B. Walker, 2–7

Whittle, M., & Wilson, A. S. 2004, AJ, 127, 606

Wilson, A. S., & Colbert, E. J. M. 1995, ApJ, 438, 62

Wilson, A. S., & Willis, A. G. 1980, ApJ, 240, 429

Wizinowich, P. L., Le Mignant, D., Bouchez, A. H., et al. 2006, PASP, 118, 297

Wright, E. L. 2006, PASP, 118, 1711

Wright, S. A. 2011,

Wrobel, J. M., & Laor, A. 2009, ApJ, 699, L22

Xu, D., & Komossa, S. 2009, ApJ, 705, L20

Zezas, A., Ward, M. J., & Murray, S. S. 2003, ApJ, 594, L31

Zheng, W., Perez, E., Grandi, S. A., & Penston, M. V. 1995, AJ, 109, 2355

Zhou, H., Wang, T., Zhang, X., Dong, X., & Li, C. 2004, ApJ, 604, L33